Electronic Energy and Charge Transfer Dynamics via Quasi-Classical Methods

by

Yudan Liu

A dissertation submitted in partial fulfillment
of the requirements for the degree of
Doctor of Philosophy
(Chemistry and Scientific Computing)
in the University of Michigan
2023

Doctoral Committee:

Professor Eitan Geva, Chair
Professor Kevin Kubarych
Professor Jennifer Ogilvie
Professor Dominika Zgid

Yudan Liu
yudanl@umich.edu
ORCID iD: 0000-0002-8485-3638

DEDICATION

To my parents, for their unconditional love and support.

ACKNOWLEDGMENTS

I would first like to thank my advisor Eitan Geva for all the help and support I have received to make this dissertation possible. The PhD journey is an especially hard one, and I am fortunate enough to have him as my mentor. Without his mentorship throughout my time being a research intern and a PhD student, I could not have enjoyed my research and grown the many skills that I have today. His support in my career pursuits has helped me achieve my goals and pursue my desired career. I would also like to thank my committee members, Kevin Kubarych, Dominika Zgid, and Jennifer Ogilvie, who have supported me, and provided great suggestions that helped me better develop my skills. I would also like to thank my many labmates: Xing Gao, Ellen Mulvihill, Alex Schubert, Yifan Lai, Miriam Woolf, Max Saller, Dalia Hassan, Callie Jones, Zongwei Huang, and Pouya Khazaei, I am truly fortunate to have the chance to meet and work with all of you. Especially, I would like to thank Xing and Ellen, who have essentially been my additional mentor. Thank you for all the help that I have received in both research and life outside of research. I cannot imagine going through the journey without you all.

To my parents, thank you for your unconditional love and support that make me who I am today. Thank you for giving me the chance and helping me in every way you can to pursue my interests. To my mom, thank you for always making me your priority and always believing in me. I cannot have survived many difficult situations without you. To my dad, thank you for many interesting conversations and for your broad knowledge that has led me to be curious about the world. To my lao-lao, thank you for always taking care of me and spoiling me with the great food you cooked. To my nai-nai, thank you for always trying to give me the best you can and for looking after me.

I would also like to express my gratitude to all my friends. To my USTC friends, Shuchen Ji and Xinyue Zhao, thank you for making my undergraduate life incredible and for always supporting

me and listening to me even with the huge timezone differences. To my Michigan friends Runxue Yu, Yichen Liu, Meichen Liu and Wen Guo, thank you for going on so many different adventures with me and helping me with my life and even research. To my consulting buddies, Amber Zhou and Sua Ryu, my job-hunting journey is only possible and tolerable because of the two of you. Thank you for the help and emotional support, I cannot have landed my job without you.

TABLE OF CONTENTS

DEDICATION ii

ACKNOWLEDGMENTS iii

LIST OF FIGURES vii

LIST OF TABLES x

ABSTRACT xii

CHAPTER

I Introduction 1

I.1 Electronic Energy and Charge Transfer Dynamics 1
I.2 Methods for Simulating Electronic Energy and Charge Transfer Dynamics . . . 3
I.3 Overview of This Dissertation 7

II Quasi-Classical Mapping Hamiltonian Methods 9

II.1 Introduction 9
II.2 Mapping Hamiltonian Approach 10
II.3 Quasi-Classical Approximations 12
II.3.1 Linearized Semi-Classical Approach 12
II.3.1.1 Connection to Ehrenfest Mean Field Method 15
II.3.2 Symmetrical Quasi-Classical (SQC) approach 16
II.4 Spin-Boson Model: Application Walkthrough 18
II.4.1 Two-Level Spin-Boson Model 18
II.4.2 Applying LSCI to Describe the Observable of Interest 19
II.4.3 Time Propagation Methods 21
II.4.4 Pseudo Code 25
II.5 Results for the Spin-Boson Model 26
II.6 Concluding Remarks 28

III The Modified Generalized Quantum Master Equation Approach 31

III.1 Introduction 31
III.2 Preliminary Considerations 32
III.3 The Generalized Quantum Master Equation 35

III.3.1Full-Dimensionality GQME with Condon Approximation 39
III.3.2Reduced-Dimensionality GQME in σ_x Representation for the Spin-Boson Model 39
III.4 Spin-Boson Model: Application Walkthrough 41
III.5 Results with Spin-Boson Model 43
III.5.1Results with the Full-Dimensionality GQME 44
III.5.2Results with Reduced-Dimensionality GQMEs in the $\hat{\sigma}_z$ representation . . 45
III.5.3Results with Reduced-Dimensionality GQME in the $\hat{\sigma}_x$ representation . . 46
III.5.4Convergence Memory Time 50
III.6 Concluding Remarks 52

IV Simulating The Linear Vibronic Coupling (LVC) Model 66

IV.1 Introduction 66
IV.2 The Linear Vibronic Coupling (LVC) Model 68
IV.3 Results with Quasi-Classical Mapping Hamiltonian Methods 70
IV.3.1Fulvene molecule 72
IV.3.22,6-bis(methylene) adamantyl (BMA) radical cation 73
IV.3.32-methylene-6-isopropylidene adamantyl (MIA) radical cation 75
IV.4 Results with Generalized Quantum Master Equation 78
IV.5 Concluding Remarks 83

V Simulating The Fenna-Matthews-Olson (FMO) Complex 85

V.1 Introduction 85
V.2 Fenna-Matthews-Olson(FMO) Complex 86
V.3 Results with Quasi-Classical Mapping Hamiltonian Methods and Generalized Quantum Master Equation 89
V.4 Concluding Remarks 91

VI Methods for Calculating the Propagator for a Quantum Open System Governed by the GQME 92

VI.1 Introduction 92
VI.2 Generating the Propagator Through The Transfer Tensor Method 93
VI.3 Generating the Propagator Directly Through The Generalized Quantum Master Equations 98
VI.4 Concluding Remarks 99

VII Conclusion 101

VII.1 Summary 101
VII.2 Future Directions 103

BIBLIOGRAPHY 105

LIST OF FIGURES

FIGURE

II.1 Dynamics of two-level spin-boson model simulated with LSC, modified LSC, and MF. Model parameters are set according to Table II.3. The DEOM results, represented by the black line, give the exact dynamics. The expectation value of $\hat{\sigma}_x$, $\hat{\sigma}_y$ and $\hat{\sigma}_z$ is described in Eq. II.52. The simulated dynamics with SQC for the same four types of two-level spin-boson model can be found in Ref. [85]. 30

III.1 Coherence dynamics of two-level spin-boson model. Model parameters are set according to Table II.3. Dash lines represent results generated directly with input methods, solid lines represent results generated with GQME. The DEOM results, represented by the black line, give the exact dynamics. 54

III.2 Matrix elements of PFIs $\mathcal{F}$, described in Eq. III.30, for model D in Table II.3, with LSCII chosen as input method. The real part of the elements are presented in pink lines and the imaginary parts are presented in blue lines. 55

III.3 Matrix elements of PFIs $\dot{\mathcal{F}}$, described in Eq. III.31, for model D in Table II.3, with LSCII chosen as input method. The real part of the elements are presented in pink lines and the imaginary parts are presented in blue lines. 56

III.4 Real part of matrix elements of the memory kernel $\mathcal{K}$of different choice of projection operators, for model D in Table II.3, with LSCII chosen as input method. 57

III.5 Imaginary part of matrix elements of the memory kernel $\mathcal{K}$of different choice of projection operators, for model D in Table II.3, with LSCII chosen as input method. . . . 58

III.6 Inhomogeneous term $\mathcal{I}$ for $\mathcal{P}$ chosen to include only electronic state $|0\rangle\langle 1|$, for model D in Table II.3, with LSCII chosen as input method. 59

III.7 $\langle\hat{\sigma}_x\rangle$ dynamics of two-level spin-boson model. Model parameters are set according to Table II.3. Dashlines represent results generated directly with input methods, solid lines represent results generated with reduced-dimensionality GQME in $\hat{\sigma}_z$ representation. The DEOM results, represented by the black line, give the exact dynamics. 60

III.8 $\langle\hat{\sigma}_y\rangle$ dynamics of two-level spin-boson model. Model parameters are set according to Table II.3. Dashlines represent results generated directly with input methods, solid lines represent results generated with reduced-dimensionality GQME in $\hat{\sigma}_z$ representation. The DEOM results, represented by the black line, give the exact dynamics. 61

III.9 Real part of matrix elements of the memory kernel $\mathcal{K}$of different choice of projection operators, for model D in Table II.3, with LSCII chosen as the input method. 62

III.10 Imaginary part of matrix elements of the memory kernel $\mathcal{K}$ of different choice of projection operators, for model D in Table II.3, with LSCII chosen as input method. . 63
III.11 Real part of the inhomogeneous term $\mathcal{I}$ for $\mathcal{P}$ chosen to include only electronic state $|0\rangle\langle 1|$, for model D in Table II.3, with LSCII chosen as input method. 64
III.12 Imaginary part of the inhomogeneous term $\mathcal{I}$ for $\mathcal{P}$ chosen to include only electronic state $|0\rangle\langle 1|$, for model D in Table II.3, with LSCII chosen as input method. 64
III.13 Coherence dynamics of two-level spin-boson model. Model parameters are set according to Table II.3. Dash lines represent results generated directly with input methods, solid lines represent results generated with reduced-dimensionality GQME in $\hat{\sigma}_z$ representation. The DEOM results, represented by the black line, give the exact dynamics. 65

IV.1 Comparison of donor population dynamics for the gas-phase fulvene molecule via different methods at T=0. The MCTDH results, represented by a black line, give the exact dynamics for fulvene with the LVC model. 73
IV.2 Comparison of donor population dynamics for the gas-phase BMA radical cation via different methods at T=0. The MCTDH results, represented by a black line, give the exact dynamics for BMA with the LVC model. 74
IV.3 Comparison of donor population dynamics for the gas-phase MIA radical cation via different methods at T=0. The MCTDH results, represented by a black line, give the exact dynamics for MIA with the LVC model. 76
IV.4 The donor population dynamics of BMA simulated with MF and GQME. The green line shows the exact results by MCTDH. The purple line shows the results generated by the input methods, i.e. MF. The Light-blue line shows the full-dimensionality non-Condon GQME results generated with MF as input methods and 149.94 fs as memory time. 79
IV.5 The donor population dynamics of MIA simulated with MF and GQME. The green line shows the exact results by MCTDH. The purple line shows the results generated by the input methods, i.e. MF. The Light-blue line shows the full-dimensionality non-Condon GQME results generated with MF as input methods and 72.5 fs as memory time. The orange line shows the full-dimensionality non-Condon GQME results generated with MF as input methods and 149.94 fs as memory time. 80
IV.6 The memory kernel elements of MIA generated with MF projection-free inputs. The horizontal axis represents time, with the unit of fs. The orange line shows the imaginary parts and the purple line shows the real parts. 81
IV.7 The memory kernel elements of BMA generated with MF projection-free inputs. The horizontal axis represents time, with the unit of fs. The orange line shows the imaginary parts and the purple line shows the real parts. 82

V.1 Demonstration of the two primary pathways of FMO complex, adopted from Ref. 91 for demonstration purposes. 87

V.2 The population dynamics of the FMO model 1 with parameters set as in Tabel V.1. Solid lines show the exact results by the hierarchical equation of motion (HEOM) reported in Ref. 139. Dashed lines show the results generated by the input methods, i.e. LSCI and LSCII, for the left and right column, respectively. Dotted-dashed lines on the left and right column show the GQME results generated with LSCI and LSCII as input methods, respectively. The top row of dynamics corresponds to the electronic initial state set as $|1\rangle\langle 1|$. The bottom row of dynamics corresponds to the electronic initial state set as $|6\rangle\langle 6|$. The convergenced memory time is reported on the graph. . . 90

VI.1 Comparison of different numerical methods on simulating the population dynamics for model D of the two-level spin-boson model described in Sec. II.4. The vertical axis represents the electronic observable $\hat{\sigma}_z$, and the horizontal axis represents the time with Γ^{-1} as the unit. Here we use LSCI to generate the projection-free inputs. The results with the three numerical methods are presented and compared to the results generated by directly solving the GQME. 96

VI.2 Comparison of different numerical methods on simulating the population dynamics for model D of the two-level spin-boson model described in Sec. II.4. The vertical axis represents the electronic observable $\hat{\sigma}_z$, and the horizontal axis represents the time with Γ^{-1} as the unit. Here we use LSCII to generate the projection-free inputs. The results with the three numerical methods are presented and compared to the results generated by directly solving the GQME. 97

LIST OF TABLES

TABLE

II.1 Summary of the five LSC-based QC/MH methods used in this chapter. $[\hat{M}]_W^{\mathrm{I}}$ is given in Eq. (II.11), $[\hat{M}]_W^{\mathrm{II}}$ is given in Eq. (II.12), $[\hat{Q}]_W$ is given in Eq. (II.14), $\phi(\mathbf{q},\mathbf{p})$ is given in Eq. (II.13), and the general form of $C_{A_W B_W}(t)$ is given in Eq. (II.10). 14

II.2 Summary of the coefficients of the Gaussian sampling and the corresponding function of random variable for implementing Eq. II.36 and II.37. 21

II.3 Spin-boson Model and Simulation Parameters 26

II.4 Summary of the accuracy of dynamics of the two-level spin-boson model via QC/MH methods reported in Ref. 85. $\surd$ indicates that the method is accurate and $\times$ indicates that the method is inaccurate. The simulated dynamics with SQC can be found in Ref. [85]. 27

III.1 Summary of full-dimensionality Condon GQME results. $\surd$ indicates that full-dimensionality GQME with QC/MH-generated input provides improved simulation results compared to QC/MH methods themselves. $\times$ indicates that full-dimensionality GQME with QC/MH-generated input provides worse simulation results compared to QC/MH methods themselves. – indicates no significant improvement of simulation by applying full-dimensionality GQME. 44

III.2 Summary of reduced-dimensionality GQME in $\hat{\sigma}_z$ representation results. $\surd$ indicates that reduced-dimensionality GQME with QC/MH-generated input provide improved simulation results comparing to QC/MH methods themselves. $\times$ indicates that reduced-dimensionality GQME with QC/MH-generated input provide worse simulation results comparing to QC/MH methods themselves. – indicates no significant improvement of simluation by reduced-dimensionality GQME. / indicates an improvement, but not at the same level of exact result. 47

III.3 Summary of reduced-dimensionality GQME in $\hat{\sigma}_x$ representation results. $\surd$ indicates that reduced-dimensionality GQME with QC/MH-generated input provides improved simulation results compared to QC/MH methods themselves. $\times$ indicates that reduced-dimensionality GQME with QC/MH-generated input provides worse simulation results compared to QC/MH methods themselves. – indicates no significant improvement of simulation by reduced-dimensionality GQME. / indicates an improvement, but not at the same level as the exact result. 49

III.4 Summary of convergence memory time for the above mentioned system and full-dimensionality non-Condon GQME. 50

III.5 Summary of convergence memory time for the above mentioned system and versions of GQME. 51

IV.1 Number of nuclear modes, absolute value of the reaction free energy, $|\Delta E|$, and reorganization energy, E_r, for fulvene, BMA, and MIA (adopted from Ref. 100). 71
IV.2 Summary of results. $\surd$ implies that the method is accurate and $\times$ implies that the method is inaccurate. 77

V.1 Fenna-Matthews-Olson (FMO) Model and Simulation Parameters 89

ABSTRACT

Electronic energy transfer and charge transfer processes play crucial roles in many photochemical processes. Computational studies on these processes are challenging subjects in the chemistry community. The problem arises from the prohibitive computational costs of the quantum-mechanically exact methods for these typically large systems. Developing methods that can handle such large dimensionality is then the key priority.

In Chapter I of this dissertation, the motivation for studying the energy transfer and charge transfer processes will be laid out. Next, a literature review of current theoretical approaches to handle these problems will be discussed.

In Chapter II, the quasi-classical mapping Hamiltonian (QC/MH) methods will be laid out with various mapping schemes. The dynamics of the four types of two-state spin-boson models generated with QC/MH methods will then be compared to the exact results. By this benchmarking of accuracy, it will be shown that the modified LSC produced the most accurate simulation results. One version of modified LSC will be shown to even have the capability to generate accurate simulation results for systems in low temperature. In addition, it will be demonstrated that even with the same method, the simulation accuracy can differ for different electronic observables. The results will emphasize the importance to evaluate all elements of electronic density matrix for method benchmarking.

In Chapter III, the generalized quantum master equation (GQME) with a general choice of projection operators will be presented, along with a walkthrough of their application procedures. The assessment of the accuracy of GQME will then be completed with two-state spin-boson model. It will be shown that the best approach for GQME is to perform population-only reduced-dimensionality GQME in the observable representation. This combination of approaches will pro-

vide the most cost-efficient and accurate simulation.

In Chapter IV, the application of QC/MH methods and GQME is furtherly demonstrated with the linear vibronic coupling (LVC) model. We will then discover that the performance of QC/MH methods on LVC models might not agree with the performance of spin-boson models. This will suggest that accuracy benchmarking should be performed not just on spin-boson model, but on LVC model as well. In Chapter V, the energy transfer process in Fenna-Matthews-Olson(FMO) complex will be studied with the QC/MH and GQME. The simulation results will show that combining QC/MH with GQME allows one to generate accurate simulations even for large and complex systems. This discussion will expand our application of QC/MH and GQME beyond two-state systems.

In Chapter VI, the various ways to generate the time evolution operators using the GQME, which can be used along with quantum computing algorithms to propagate the system, will be discussed. A comparison between different approaches will then be discussed, and we will find out that the best approach is to directly generate the propagator through GQME.

In Chapter VII, we will present a summary of the discussions. In addition, further directions for QC/MH and GQME will be presented. This includes applying QC/MH and GQME to wider range of systems and further development on the reduced-dimensionality Condon approximation GQME.

CHAPTER I

Introduction

I.1 Electronic Energy and Charge Transfer Dynamics

Photo-induced electronic energy transfer and charge transfer dynamics play a central role in many fields, including photochemistry, solar energy, photosynthesis, and photovoltaics.[1] For example, photosynthesis can be divided into four stages: (1) light absorption and energy transfer via antenna systems, (2) primary electron transfer in reaction centers, (3) energy stabilization by secondary processes, and (4) synthesis and export of stable products [2]. In the first stages, the photon absorption gives rise to an excited state that results in charge separation in the reaction center. Generally speaking, the antenna system performs an energy transfer process, which migrates the electronic excited states from one molecule to another. This first step typically ends with an electronically excited donor in the reaction center. The second stage is where the conversion of electronic excitation energy to electrical energy takes place. The electronically excited donor transfer charges rapidly to the electron acceptor nearby. During this process, the excitation energy gets converted to electrical energy. Therefore the primary reaction happens during this process. In the third stage of photosynthesis, positive and negative charges are separated through a series of rapid secondary chemical reactions. The last stage in the photosynthesis process is to produce stable high-energy molecules. Electronic energy transfer and charge transfer are two critical steps in the photosynthesis process, therefore are the center of many studies.[3–7]

Understanding the dynamical processes of excitation energy transfer and charge transfer also

facilitates and enables the design of photovoltaic materials and devices capable of efficiently capturing and utilizing solar energy.

Photovoltaic technologies generate power by using devices that absorb solar energy and convert it into electrical energy. The increasing demand for energy, the rising price of fuels, and the growing concerns about the environment all lead to an urgent call for more utilization of renewable energy sources.[8] Photovoltaic technologies are among those of interest. Photovoltaic panels have the advantage of utilizing free natural energy sources with no greenhouse gases produced.[9] Inorganic solar cells, namely silicon-based devices, have been the leading technology in this field. Although silicon-based devices can achieve high power conversion efficiency[10], they are typically expensive and cannot be produced in large sizes. One alternative is organic solar cells. Single-component organic solar cells typically have low efficiency.[11] Studies have shown that with two components, efficiency can be improved.[12] The two components are made up of one electron-donor material and one electron-acceptor material. This technology, along with advancement in the material used, boost the power conversion efficiency of organic solar cells.[13–16] The charge transfer process between the donor and acceptor interface is an important feature of these technologies. The process can be described as a photoexcited donor-localized bright excited state transitioning to a donor-to-accepter interfacial charge-transfer state, then followed by a charge separation process or a charge recombination process.[17] The charge separation process leads to the dissociation of electron-hole pair and the charge recombination process leads to dissipating excess energy as heat. Promoting more charge separation will allow more efficient energy conversion. Understanding the charge transfer processes is crucial to improve conversion efficiency.

Gaining more understanding and having the ability to simulate the energy transfer and charge transfer processes can allow more efficient development of solar energy technologies. Performing accurate simulations can point to new directions of development, meanwhile reducing the economic cost of traditional research and development. The above processes can typically be described by open quantum systems. In the open quantum systems that describe the electronic energy transfer and charge transfer processes, the system is typically the electronic degrees of freedom

(DOF), and the bath that is coupled to the system is typically the nuclear degrees of freedom. In the next section, we will discuss various methods that can be used to simulate these processes.

I.2 Methods for Simulating Electronic Energy and Charge Transfer Dynamics

To accurately capture quantum effects, it is best to use quantum-mechanical exact methods to simulate the energy and charge transfer dynamics.

An example of such a quantum-mechanically exact method is the multiconfiguration time-dependent Hartree (MCTDH) method. MCTDH is a wavepacket-propagation-based exact method.[18–20] MCTDH is a variant of the multiconfigurational time-dependent self-consistent field (MC-TDSCF) method.[21] The MCTDH method uses a multiconfigurational wavefunction ansatz with single-particle wavefunction as time-dependent basis functions. Then the time-dependent Schrödinger equation is solved by a variational method.[22] Even though MCTDH scales exponentially with dimension, it is still computationally cheaper than the standard wavepacket dynamics.[18] This arises from the usage of time-dependent basis functions in MCTDH, instead of the time-independent wavefunction used in the standard wavepacket dynamics.

Another exact method is the dissipation equation of motion (DEOM).[23] The DEOM approach is formally exact for models with Gaussian bath, i.e. the linear hybridization noninteracting bath model. In DEOM, the linear hybridization bath operators are decomposed into dissipation operators. The dissipation density operators (DDO) can then be defined with the dissipation operators. The dynamics of DDO can be achieved by applying the Liouville-von Neumann equation. The typical observable of interest – the reduced system density operator, is the zeroth order DDO. The DEOM formalism can be constructed with another well-known method, the hierarchical equations of motion (HEOM).[23–25] The main difference between DEOM and HEOM is that the HEOM provides no physical meanings on the dynamics variables.[23] It is worth noticing here that the

decomposition of bath correlation can be prohibitively expensive for systems at close-to-zero temperatures, which limits the usage of DEOM. This low-temperature situation, however, generally can be handled by MCTDH.

As we see from the two examples of quantum-mechanically exact methods presented above, these methods typically either have requirements on the specific form of the model or have computational costs that scale exponentially with the increase of dimensionality. Unfortunately, quantum systems of chemical interest typically involve the system, bath, and system-bath interactions, resulting in high dimensionality, which makes exact methods impractical. This prompts the many studies and development of a wide variety of approximate approaches.

Surface hopping provides a practical approach for describing the coupled dynamics in large condensed phase systems. It is possible to implement surface hopping on the fly with ab initio electronic structure methods.[26] The fewest switches surface hopping (FSSH) algorithm was proposed aiming to increase the stability of the trajectory-based methods.[27] In this approach, the initial wavepacket's density is sampled as classical trajectories. Then the nuclear DOF are propagated classically, while the electronic DOF are propagated quantum mechanically with the Schrödinger equation. The probability of switching surface is calculated at each step, and hopping is only allowed with energy conservation. The FSSH approach was shown to provide an accurate description of the short-time dynamics through the conical intersections.[28] However, FSSH does not properly account for decoherence.[27, 29, 30] Several new approaches have been proposed aiming to fix this issue. However, most approaches centering on the decoherence are empirical.[30–34]. Restrictions on the applicability of FSSH also arise from the assumption that the system starts at a single adiabatic state. The derivation connecting the FSSH and the quantum-classical Liouville equation provides ways to overcome this.[35]

The mapping Hamiltonian method, proposed by Meyer and Miller[36], uses mapping relations that follow the same commutation relations as the density matrix and observable dynamics. This approach is motivated by the use of auxiliary position and momentum operators, which have a clear classical limit, and was further investigated by Stock and Thoss on the mapping relations

using the harmonic oscillator model[37]. Different mapping methods have been proposed, including the linearized semi-classical (LSC) methods. The LSC methods: the Poisson-bracket mapping equation (PBME)[38, 39] and the linearized semi-classical method (LSC-IVR)[40, 41], or LSCI and LSCII respectively, are based on the harmonic oscillator's creation and annihilation operator and the wavefunction of singly-excited states, respectively. However, the closure relation is not guaranteed for every trajectory with the LSC methods. To solve this issue, a modified linearized semi-classical approach was introduced, which expressed the closure relation in the mapping relations, ensuring closure relations.[42, 43]. Another mapping scheme, the symmetrical quasi-classical method (SQC), uses the action-angle variables and filters trajectories by a window, resulting in accurate descriptions of population dynamics for various system types.[44–49]

The mixed quantum-classical Liouville (MQCL) equation may be obtained from the quantum Liouville equation using a partial Wigner representation, where Wigner transformation is performed to the classical DOF, and by considering the limit of small mass ratio between the classical and quantum DOF.[50] It is reported that for an arbitrary quantum subsystem bilinearly coupled to a harmonic environment, the MQCL reproduces the exact fully quantum-mechanical dynamics.[51] The MQCL equation has the advantage of being more accurate than some other semi-classical methods.[52–54] The downside of MQCL is the relatively high computational cost. Sequential Short-Time Propagation (SSTP) algorithm[55] and the Trotter-Based Surface-Hopping (TBSH)[56] algorithm can be used to solve the MQCL equations. The two methods are trajectory-based algorithms that utilized Monte Carlo sampling. Therefore, the computational cost of these two algorithms can be quite large due to the increasing number of trajectories required for convergence. To minimize the related computational cost, the transition filtering technique was proposed, aiming to reduce the statistical errors.[55, 57] The observable cutting is another technique, implemented to reduce the number of trajectories required. It restricts the statistical weight of trajectories when it reaches some certain value.[58]

The quantum-classical path integral (QCPI) method is a rigorous approach that combines the fully quantum mechanical treatment for the small system and the classical trajectory approach for

the large system. This is completed by restricting the path sum to the classical trajectories for the heavy particles and maintaining the quantum path sum for the light particles.[59] The challenge of this approach arises from the computational cost of the evaluation of real-time path integral expressions. One possible path is developed by exploiting the mechanism of decoherence, which occurs when a quantum system interacts with its surrounding environment.[60] One recent progress on QCPI is the small matrix quantum-classical path integral(SMatQCPI), which eliminates the tensor storage requirements through a small matrix decomposition.[61]

Another approach to simulating electronic energy and charge transfer dynamics is based on quantum master equations. A quantum master equation typically refers to first-order differential equations describing the time evolution of a quantum system or observable of interest. For example, the Redfield quantum master equation is a Markovian master equation that describes the time evolution of the reduced density matrix of a system coupled to a bath.[62] The Redfield quantum master equation can be derived based on second-order perturbation treatment in the system-bath coupling. Therefore, it is best for models with weak system-bath coupling. The Redfield theory is closely connected to the Lindblad master equation, and both methods assume Markovianity. Such a Markovian approximation ignores the effect of memory, meaning that the future of the system of interest is not affected by the past. One approach that accounts for non-Markovian effects is the Nakajima-Zwanzig generalized quantum master equation (NZ-GQME). NZ-GQME is based on using projection superoperators in Liouville space, resulting in the time evolution of the projected density matrix. By focusing only on the most important part of the system, the NZ-GQME can reduce the computational cost significantly. The effect of the rest of the system on the projected density matrix is incorporated into the memory kernel. Shi and Geva proposed a formally exact approach for generating memory kernels using only projection-free inputs.[63] The accuracy of this method has been demonstrated with both quantum-mechanically exact and semi-classical inputs for the spin-boson model.[63, 64] To account for arbitrary initial state and system-bath coupling, the Zhang-Ka-Geva approach was introduced.[65] Further evidence of the efficacy of the Shi-Geva GQME approach was shown by generating projection-free inputs using surface hopping[66] and

Ehrenfest mean field methods[67]. This method requires expressing the Hamiltonian in a system-bath form. Mulvihill et al. proposed a modified GQME approach that eliminates the restriction on the form of the Hamiltonian, making it generally applicable.[68, 69] To reduce computational costs further, a reduced-dimensionality GQME approach was also proposed.[70]

Our focus in this dissertation is to develop general, low-cost quasi-classical methods that are capable of describing the energy transfer and charge transfer dynamics of open quantum systems accurately. More specifically, we will center our attention on the quasi-classical mapping Hamiltonian (QC/MH) methods and the generalized quantum master equation (GQME).

I.3 Overview of This Dissertation

In this dissertation, we will use bold letters, e.g. $\mathbf{A}$, to represent vector variables and hat on letters, e.g. $\hat{B}$, to represent operators in Hilbert space. The rest of this dissertation is organized as follows. In Chapter II, we first present the general mapping Hamiltonian method. Then the different quasi-classical approximations of the mapping Hamiltonian methods are presented. Next, we walk through the application of the linearized semi-classical approximation to the two-level spin-boson model as a demonstration. The simulation results of the two-level spin-boson model via QC/MH are then provided and compared to the results from exact methods. In Chapter III, the modified approach to the generalized quantum master equation with a general form of projection operator is described. We then walk through the application of GQME to the two-level spin-boson model. The simulation results of the coherence dynamics of the two-level spin-boson model are then presented and compared to the exact results generated with the dissipation equation of motion (DEOM). In Chapter IV, we apply the above-mentioned QC/MH methods and the GQME to a model with conical intersections: the linear vibronic coupling model. We compared the simulation results with the exact dynamics and emphasized the necessity of benchmarking and evaluating methods over different types of models. In Chapter V, the QC/MH methods and the GQME are applied to the Fenna-Matthews-Olson (FMO) complex, a photosynthetic complex with long-lived quantum co-

herences. Then we report the simulation results and compare those to the dynamics generated via an exact method. In Chapter VI, the various ways to calculate time evolution propagators, that can be used in quantum computing algorithms, are discussed and compared. A summary of the dissertation and outlook for future projects with the quasi-classical methods is then given in Chapter VII.

CHAPTER II

Quasi-Classical Mapping Hamiltonian Methods

II.1 Introduction

The mapping Hamiltonian method was proposed by Meyer and Miller[36] and later investigations on the mapping relations using the harmonic oscillator model were done by Stock and Thoss[37]. The mapping relations follow the same commutations relations. This approach is prompted by the fact that both the density matrix dynamics and the observable dynamics are dictated by commutators. This approach is motivated by the fact that mapping relations can be expressed using auxiliary position and momentum operators, which have a clearly defined classical limit. With the quasi-classical approximation, the nuclear coordinates and momenta, as well as the auxiliary coordinates and momenta associated with the electronic DOFs, are typically treated classically.

The choice of mapping is not unique. The two linearized semi-classical (LSC) methods, originally named the Poisson-bracket mapping equation (PBME)[38, 39] and the linearized semi-classical method (LSC-IVR)[40, 41], arise from the creation and annihilation operator of the harmonic oscillators and the wavefunction of singly-excited states, respectively. The well-known Ehrenfest mean-field method can be thought of as a QC/MH method with a pre-setted initial value for the auxiliary position and momentum. For the LSC methods, the closure relation is not guaranteed for each trajectory. To address this issue, the modified linearized semi-classical approach was proposed.[42, 43] The modified LSC explicitly expressed the closure relation in the mapping relations, ensuring the closure relations. This approach showed significant improvements

for the spin-boson model and the Fenna-Matthews-Olson (FMO) complex compared to the LSC approach.[42, 43] A variation of the mapping scheme that is based on the action-angle variables is the symmetrical quasi-classical method (SQC). In SQC, the trajectories are filtered by a window. This results in accurate descriptions of the population dynamics for various types of systems.[44–49]

The rest of this chapter is organized as follows. The mapping Hamiltonian formalism is presented in Sec. II.2. Next, we present various mapping schemes and the quasi-classical approximations in Sec. II.3. In Sec. II.4, we use the two-level spin-boson model to demonstrate the application of QC/MH methods. In the next section, we present the simulation results of the dynamics of the electronic density matrix of the two-level spin-boson model, compared to the dynamics generated with the dissipation equation of motion (DEOM). Concluding remarks are given in section II.6.

II.2 Mapping Hamiltonian Approach

MH methods are based on casting the population and coherence operators, $\{|j\rangle\langle k|\}$, onto an isomorphic set of operators, $\{M_{jk}(\hat{\mathbf{q}}, \hat{\mathbf{p}})\}$:

$$|j\rangle\langle k| \mapsto M_{jk}(\hat{\mathbf{q}}, \hat{\mathbf{p}}) \quad , \tag{II.1}$$

with $\{M_{jk}(\hat{\mathbf{q}}, \hat{\mathbf{p}})\}$ satisfying the same commutation relations as $\{|j\rangle\langle k|\}$.[36, 39, 40, 42, 43, 71–78, 78–86] Here, $\{\hat{\mathbf{q}}, \hat{\mathbf{p}}\}$ are a set of auxiliary Cartesian coordinate and momentum operators. The reason for utilizing mapping operators over the original electronic operators is that $\{M_{jk}(\hat{\mathbf{q}}, \hat{\mathbf{p}})\}$ have classical-like analogs and therefore allow QC approximations to be used, unlike with $\{|j\rangle\langle k|\}$.

One electronic observable of common interest is the electronic density operator at a later time

t. This is given by:

$$\hat{\sigma}(t) = \mathrm{Tr}_n \left\{\hat{\rho}(t)\right\} = \sum_{m,n=1}^{Ne} \sigma_{mn}(t) \left|m\right\rangle\!\left\langle n\right|, \tag{II.2}$$

$$\begin{aligned} \text{with } \sigma_{mn}(t) &= \langle m| \hat{\sigma}(t) |n\rangle = \mathrm{Tr}\left\{\hat{\rho}(t) \left|n\right\rangle\!\left\langle m\right|\right\} \\ &= \mathrm{Tr}\left\{e^{-i\hat{H}t/\hbar}\hat{\rho}(0)e^{i\hat{H}t/\hbar} \left|n\right\rangle\!\left\langle m\right|\right\} = \mathrm{Tr}\left\{\hat{\rho}(0)e^{i\hat{H}t/\hbar}.\left|n\right\rangle\!\left\langle m\right| e^{-i\hat{H}t/\hbar}\right\} \end{aligned} \tag{II.3}$$

Here, $\hat{\rho}(0)$ is the nonequilibrium initial state and N_e represents the number of electronic DOF. $\sigma_{mm}(t)$ corresponds to the population of the n-th electronic state and $\sigma_{mn}(t)$ (where $m \neq n$) corresponds to the electronic coherence between the m-th and the n-th electronic states. Note that $e^{i\hat{H}t/\hbar} \left|n\right\rangle\!\left\langle m\right| e^{-i\hat{H}t/\hbar}$ can be considered as the observable $\left|n\right\rangle\!\left\langle m\right|$ at time t:

$$\sigma_{mn}(t) = \mathrm{Tr}\left\{\hat{\rho}(0) \left|n\right\rangle\!\left\langle m\right| (t)\right\}. \tag{II.4}$$

Although choices of initial state is not unique, the typical choice is $\hat{\rho}(0) = \hat{\rho}_n(0) \otimes \left|\alpha\right\rangle\!\left\langle\alpha\right|$. We will use this to demonstrate QC/MH methods in this chapter. With this choice, we can then write the electronic density matrix elements as:

$$\sigma_{mn}(t) = \mathrm{Tr}\left\{\hat{\rho}_n(0) \otimes \left|\alpha\right\rangle\!\left\langle\alpha\right| e^{i\hat{H}t/\hbar} \left|n\right\rangle\!\left\langle m\right| e^{-i\hat{H}t/\hbar}\right\} \equiv C_{\hat{M}_{\alpha\alpha}\hat{M}_{nm}}(t). \tag{II.5}$$

As outlined in Refs. 42 and 43, the electronic population operator can also be mapped as the sum of the identity operator $\hat{1}$ and a trace zero term, giving the alternative form

$$\left|m\right\rangle\!\left\langle m\right| \mapsto \frac{1}{N_e}(\hat{1} + \hat{Q}_m) \quad , \tag{II.6}$$

where

$$\hat{Q}_m = N_e\hat{M}_{mm} - \sum_{b=1}^{N_e} \hat{M}_{bb} \quad . \tag{II.7}$$

in which $\hat{M}_{mm} \equiv \left|m\right\rangle \left\langle m\right|$, and N_e is the number of electronic DOF. Plugging Eq. (II.6) into

Eq. (II.5) leads to the following alternative expressions for the electronic density matrix elements:

$$\begin{aligned}\sigma_{mm}(t) &= \frac{1}{N_e^2}\Big[N_e + C_{\hat{1}\hat{Q}_m}(t) + C_{\hat{Q}_\alpha\hat{Q}_m}(t)\Big] \\ \sigma_{mn}(t) &= \frac{1}{N_e}\Big[C_{\hat{1}\hat{M}_{nm}}(t) + C_{\hat{Q}_\alpha\hat{M}_{nm}}(t)\Big] \quad .\end{aligned} \tag{II.8}$$

Here $\hat{M}_{nm} \equiv |n\rangle\langle m|$, and the correlation function

$$C_{AB}(t) = \mathrm{Tr}\Big\{\hat{\rho}_n(0)A(\hat{\mathbf{q}}(0),\hat{\mathbf{p}}(0))B(\hat{\mathbf{q}}(t),\hat{\mathbf{p}}(t))\Big\} \quad . \tag{II.9}$$

II.3 Quasi-Classical Approximations

II.3.1 Linearized Semi-Classical Approach

Applying the LSC approximation[87] to a correlation function of the form given in Eq. (II.9) results in the following QC approximation for $C_{\hat{A}\hat{B}}(t)$:

$$\begin{aligned}&C_{A_W B_W}(t) = \\ &\left(\frac{1}{2\pi\hbar}\right)^{N_e+N_n}\int \mathbf{dR}_0 \int \mathbf{dP}_0 \int \mathbf{dq}_0 \int \mathbf{dp}_0 [\hat{\rho}_n(0)]_W(\mathbf{R}_0,\mathbf{P}_0)A_W(\mathbf{q}_0,\mathbf{p}_0)B_W(\mathbf{q}_t,\mathbf{p}_t) \quad .\end{aligned} \tag{II.10}$$

Applying the QC approximation to the correlation functions in Eq. (II.5) and (II.8) leads to two alternative QC/MH approximations for the electronic density matrix elements, detailed in the following.

The actual choice of mapping variables is not unique and multiple choices of mapping variables have been proposed and employed.[75–78, 84, 88] In this chapter, we consider two such choices, which are based on the Stock-Thoss-Meyer-Miller mapping[36, 37] (the reader is referred to Refs. 69 and 85 for a more detailed discussion of these two choices). The first choice, which we

refer to as *mapping #1*, leads to the following QC mapping variables:

$$\begin{aligned}
[\hat{M}_{mm}]_W^{(\mathrm{I})}(\mathbf{q},\mathbf{p}) &= \frac{1}{2\hbar}(q_m^2+p_m^2-\hbar) \\
[\hat{M}_{mn}]_W^{(\mathrm{I})}(\mathbf{q},\mathbf{p}) &= \frac{1}{2\hbar}(q_m-ip_m)(q_n+ip_n) \quad .
\end{aligned} \tag{II.11}$$

The second choice, which we refer to as *mapping #2*, leads to the following QC mapping variables:

$$\begin{aligned}
[\hat{M}_{mm}]_W^{(\mathrm{II})}(\mathbf{q},\mathbf{p}) &= \phi(\mathbf{q},\mathbf{p})\left(q_m^2+p_m^2-\frac{\hbar}{2}\right) \\
[\hat{M}_{mn}]_W^{(\mathrm{II})}(\mathbf{q},\mathbf{p}) &= \phi(\mathbf{q},\mathbf{p})(q_m-ip_m)(q_n+ip_n) \quad ,
\end{aligned} \tag{II.12}$$

where

$$\phi(\mathbf{q},\mathbf{p}) = \frac{2^{N_e+1}}{\hbar}\exp\left[-\frac{1}{\hbar}\sum_{l=1}^{N_e}\left(q_l^2+p_l^2\right)\right] \quad . \tag{II.13}$$

We also note that the QC mapping #1 and mapping #2 approximations for $\hat{Q}_m$, Eq. (II.7), are given by:

$$\begin{aligned}
[\hat{Q}_m]_W^{(\mathrm{I})}(\mathbf{q},\mathbf{p}) &= N_e[\hat{M}_{mm}]_W^{(\mathrm{I})}(\mathbf{q},\mathbf{p}) - \sum_{b=1}^{N_e}[\hat{M}_{bb}]_W^{(\mathrm{I})}(\mathbf{q},\mathbf{p}) \quad , \\
[\hat{Q}_m]_W^{(\mathrm{II})}(\mathbf{q},\mathbf{p}) &= N_e[\hat{M}_{mm}]_W^{(\mathrm{II})}(\mathbf{q},\mathbf{p}) - \sum_{b=1}^{N_e}[\hat{M}_{bb}]_W^{(\mathrm{II})}(\mathbf{q},\mathbf{p}) \quad .
\end{aligned} \tag{II.14}$$

Applying the above-mentioned QC/MH approximations to Eqs. (II.5) or (II.8) yields the five different LSC-based methods shown in Table II.1 (see Refs. 85 and 42 for a more detailed discussion). The first two methods, LSCI (also referred to as PBME[39]) and LSCII (also referred to as LSC-IVR[40]) are based on Eq. (II.5). Both LSCI and LSCII use mapping #2 for $[\hat{M}_{\alpha\alpha}]_W$ but differ from each other in the mapping used for $[\hat{M}_{nm}]_W$, with LSCI using mapping #1 and LSCII using mapping #2.

The third through fifth LSC-based methods are based on Eq. (II.8) and were recently introduced by Saller et al.[42] For the correlation functions $C_{[\hat{1}]_W[\hat{Q}_m]_W}$, $C_{[\hat{1}]_W[\hat{M}_{nm}]_W}$, $C_{[\hat{Q}_\alpha]_W[\hat{Q}_m]_W}$ and $C_{[\hat{Q}_\alpha]_W[\hat{M}_{nm}]_W}$ [see Eq. (II.8)], all three methods use mapping #2 for $[\hat{Q}_m]_W$ and $[\hat{M}_{nm}]_W$ but dif-

fer in how they map the unity operator and in the mapping used for $[\hat{Q}_\alpha]_W$. The third method, referred to as mLSC/$\phi^1\phi^1$, maps the unity operator onto 1 and uses mapping #1 for $[\hat{Q}_\alpha]_W$. The fourth method, referred to as mLSC/$\phi^1\phi^2$, maps the unity operator onto 1 and uses mapping #2 for $[\hat{Q}_\alpha]_W$. The fifth method, referred to as mLSC/$\phi^2\phi^2$, maps the unity operator onto $2\hbar\phi(\mathbf{q},\mathbf{p})$ [with $\phi(\mathbf{q},\mathbf{p})$ given in Eq. (II.13)] and uses mapping #2 for $[\hat{Q}_\alpha]_W$.

Methods using $\sigma(t)$ based on Eq. (II.5)		
Method	$C_{[\hat{M}_{\alpha\alpha}]_W[\hat{M}_{kj}]_W}(t)$	
	$[\hat{M}_{\alpha\alpha}]_W$ mapping	$[\hat{M}_{kj}]_W$ mapping
LSCI	$[\hat{M}_{\alpha\alpha}]_W^{(\mathrm{II})}(\mathbf{q},\mathbf{p})$	$[\hat{M}_{kj}]_W^{(\mathrm{I})}(\mathbf{q},\mathbf{p})$
LSCII	$[\hat{M}_{\alpha\alpha}]_W^{(\mathrm{II})}(\mathbf{q},\mathbf{p})$	$[\hat{M}_{kj}]_W^{(\mathrm{II})}(\mathbf{q},\mathbf{p})$

Methods using $\sigma(t)$ based on Eq. (II.8)				
Method	$C_{[\hat{A}]_W[\hat{B}]_W}(t)$			
	$[\hat{A}]_W$		$[\hat{B}]_W$	
	$[\hat{1}]_W$ mapping	$[\hat{Q}_m]_W$ mapping	$[\hat{Q}_\alpha]_W$ mapping	$[\hat{M}_{kj}]_W$ mapping
mLSC/$\phi^1\phi^1$	1	$[\hat{Q}_m]_W^{(\mathrm{I})}(\mathbf{q},\mathbf{p})$	$[\hat{Q}_m]_W^{(\mathrm{II})}(\mathbf{q},\mathbf{p})$	$[\hat{M}_{kj}]_W^{(\mathrm{II})}(\mathbf{q},\mathbf{p})$
mLSC/$\phi^1\phi^2$	1	$[\hat{Q}_m]_W^{(\mathrm{II})}(\mathbf{q},\mathbf{p})$	$[\hat{Q}_m]_W^{(\mathrm{II})}(\mathbf{q},\mathbf{p})$	$[\hat{M}_{kj}]_W^{(\mathrm{II})}(\mathbf{q},\mathbf{p})$
mLSC/$\phi^2\phi^2$	$2\hbar\phi(\mathbf{q},\mathbf{p})$	$[\hat{Q}_m]_W^{(\mathrm{II})}(\mathbf{q},\mathbf{p})$	$[\hat{Q}_m]_W^{(\mathrm{II})}(\mathbf{q},\mathbf{p})$	$[\hat{M}_{kj}]_W^{(\mathrm{II})}(\mathbf{q},\mathbf{p})$

Table II.1: Summary of the five LSC-based QC/MH methods used in this chapter. $[\hat{M}]_W^{\mathrm{I}}$ is given in Eq. (II.11), $[\hat{M}]_W^{\mathrm{II}}$ is given in Eq. (II.12), $[\hat{Q}]_W$ is given in Eq. (II.14), $\phi(\mathbf{q},\mathbf{p})$ is given in Eq. (II.13), and the general form of $C_{A_W B_W}(t)$ is given in Eq. (II.10).

In order to obtain the correlation functions in Eqs. (II.5) and (II.8), the nuclear and electronic coordinates and momenta at time t, $\{\mathbf{R}_t,\mathbf{P}_t,\mathbf{q}_t,\mathbf{p}_t\}$, need to be obtained from the initial state $\{\mathbf{R}_0,\mathbf{P}_0,\mathbf{q}_0,\mathbf{p}_0\}$. The initial nuclear coordinates and momenta are sampled from the Wigner transform of the initial nuclear density matrix. The initial electronic coordinates and momenta are sampled based on the phase-space density $\phi(\mathbf{q}_0,\mathbf{p}_0)$ (see Table II.1). $\{\mathbf{R}_t,\mathbf{P}_t,\mathbf{q}_t,\mathbf{p}_t\}$ is obtained from $\{\mathbf{R}_0,\mathbf{P}_0,\mathbf{q}_0,\mathbf{p}_0\}$ via classical dynamics as dictated by the symmetrized mapping Hamiltonian[36, 79]. More specifically, we treat $\hat{\mathbf{q}}$ and $\hat{\mathbf{p}}$ classically by applying Hamilton's

equation to derive the equation of motion:

$$\dot{\mathbf{p}} = -\frac{\partial H}{\partial \mathbf{q}}, \qquad \dot{\mathbf{q}} = \frac{\partial H}{\partial \mathbf{p}}. \tag{II.15}$$

Detailed walkthrough of the application of LSC on the spin-boson model is presented in Sec. II.4.

II.3.1.1 Connection to Ehrenfest Mean Field Method

The mean-field (MF) method can also be cast as a QC/MH-type method[36] by expanding the electronic wave function at time t in the electronic basis, $\{|j\rangle\}$,

$$|\psi(t)\rangle = \sum_{j=1}^{N_e} c_j(t)|j\rangle \ , \tag{II.16}$$

and expressing the expansion coefficients in terms of Cartesian coordinates and momenta as follows

$$c_j = \frac{1}{\sqrt{2}}(q_j + ip_j) \quad . \tag{II.17}$$

The corresponding electronic density matrix is given by

$$\hat{\sigma}(t) = |\psi(t)\rangle\langle\psi(t)| = \sum_{j,k=1}^{N_e} c_j(t)c_k^*(t)|j\rangle\langle k| \quad . \tag{II.18}$$

It can then be shown that the MF method is equivalent to propagating $\{\mathbf{R}_t, \mathbf{P}_t, \mathbf{q}_t, \mathbf{p}_t\}$ as classical variables whose dynamics is governed by the QC Hamiltonian.[36] The initial nuclear coordinates and momenta within the MH method are sampled in the same way as the LSC and SQC methods. However, unlike the LSC and SQC methods, the initial values of the electronic coordinates and momenta, $\{\mathbf{q}_0, \mathbf{p}_0\}$ are uniquely determined by $c_j(0)$.

II.3.2 Symmetrical Quasi-Classical (SQC) approach

The symmetrical quasiclassical (SQC) method can also be viewed as an alternative implementation of the LSC approximation.[44–49] This method is formulated in terms of action-angle (a-a) variables rather than in terms of Cartesian coordinates and momenta. Each electronic state $|j\rangle$ is associated with a *classical* harmonic mode whose state is described by an action variable, n_j, and an angle variable, u_j.[36, 76] The QC mapping variables for the electronic density matrix elements in terms of a-a variables are given by

$$\begin{aligned}
[\hat{M}_{mm}]_W^{(\text{SQC})}(\mathbf{n},\mathbf{u}) &= \delta(n_m - 1) \prod_{\substack{\xi=1 \\ \xi\neq m}}^{N_e} \delta(n_\xi) \quad , \\
[\hat{M}_{mn}]_W^{(\text{SQC})}(\mathbf{n},\mathbf{u}) &= e^{i(u_n - u_m)}\, \delta\left(n_m - \frac{1}{2}\right) \delta\left(n_n - \frac{1}{2}\right) \prod_{\substack{\xi=1 \\ \xi\neq m,n}}^{N_e} \delta(n_\xi) \quad ,
\end{aligned} \tag{II.19}$$

where $\mathbf{n} = (n_1, ..., n_{N_e})$ and $\mathbf{u} = (u_1, ..., u_{N_e})$. The SQC method is based on replacing the delta functions in Eq. (II.19) with pre-limit delta functions. We use two different choices that lead to square sampling windows and triangular sampling windows.[48]

For the square sampling windows, $\delta(n_j - a)$ is replaced with $h(\gamma - |n_j - a|)/2\gamma$, where

$$h(x) = \begin{cases} 1 & x \geq 0 \\ 0 & x < 0 \end{cases} \tag{II.20}$$

is the Heaviside function. This gives mapping variables for two-state systems of the form

$$\begin{aligned}
[\hat{M}_{mm}]_W^{(\text{SQC_square})}(\mathbf{n},\mathbf{u}) &= h(\gamma - |n_m - 1|) h(\gamma - |n_n|) \, , \\
[\hat{M}_{mn}]_W^{(\text{SQC_square})}(\mathbf{n},\mathbf{u}) &= e^{i(u_n - u_m)}\, h\left(\gamma - \left|n_m - \frac{1}{2}\right|\right) h\left(\gamma - \left|n_n - \frac{1}{2}\right|\right) \quad ,
\end{aligned} \tag{II.21}$$

where γ is the window width parameter. The value of the window width parameter, γ, is typically set to 0.366, as recommended in Ref. 45.

For triangular sampling windows, the mapping variables for two-state systems are given by

$$
\begin{aligned}
&[\hat{M}_{mm}]_W^{(\text{SQC\_triangle})}(\mathbf{n},\mathbf{u}) = 2h(n_m+\gamma-1)h(n_n+\gamma)h(2-2\gamma-n_m-n_n) \quad , \\
&[\hat{M}_{mn}]_W^{(\text{SQC\_triangle})}(\mathbf{n},\mathbf{u}) = 2e^{i(u_n-u_m)}h\left(n_m+\gamma-\frac{1}{2}\right)h\left(n_n+\gamma-\frac{1}{2}\right)h(2-2\gamma-n_m-n_n) \quad .
\end{aligned}
\tag{II.22}
$$

Previous studies[48] showed that using triangular sampling windows gives rise to more accurate results and better convergence compared to using square sampling windows.

Within SQC, initial nuclear coordinates and momenta are sampled based on $[\hat{\rho}_n(0)]_W(\mathbf{R}_0,\mathbf{P}_0)$ (the same as in LSC-based methods). In the case of a system with an initial electronic state $\hat{\sigma}(0) = |\alpha\rangle\langle\alpha|$, for square windows, initial sampling of the action variable, n_l, is done following uniform distribution within the intervals

$$
\begin{cases}
(1-\gamma, 1+\gamma) & l=\alpha \\
(-\gamma,\gamma) & l\neq\alpha
\end{cases}
\quad . \tag{II.23}
$$

For triangle windows, n_l is sampled following uniform distribution within the intervals

$$
\begin{cases}
(1-\gamma, 2-\gamma) & l=\alpha \\
(-\gamma,1-\gamma) & l\neq\alpha
\end{cases}
\quad , \tag{II.24}
$$

subject to the constraint $n_m + n_n \leq 2-2\gamma$. For both square and triangle mapping variables, initial sampling of the angle variables, $\{u_l\}$, is done following a uniform distribution within the interval $(0, 2\pi)$.

The dynamics of the a-a variables within SQC are done in terms of Cartesian coordinates and momenta and are identical to that in the LSC-based methods. The relationship between the a-a

variables and the Cartesian coordinates and momenta are given by

$$\begin{aligned} q_l &= \sqrt{2(n_l+\gamma)\hbar}\cos(u_l) \quad , \\ p_l &= \sqrt{2(n_l+\gamma)\hbar}\sin(u_l) \quad . \end{aligned} \tag{II.25}$$

It should be noted that another implementation of the SQC method, which allows for a trajectory-dependent definition of γ, was recently shown to be significantly more accurate when applied to a one-dimensional photodissociation model.[89]

II.4 Spin-Boson Model: Application Walkthrough

In this section, we demonstrate how to apply QC/MH methods, more specifically LSCI, on the two-level spin-boson model to simulate the time evolution of reduced electronic density matrix:

$$\hat{\sigma}(t) = \mathrm{Tr}_n\left\{\rho(t)\right\}. \tag{II.26}$$

II.4.1 Two-Level Spin-Boson Model

The spin-boson model describes an open system with electronic states coupled to bath containing harmonic oscillators. The Hamiltonian of a two-level spin-boson model is:

$$\begin{aligned} \hat{H} = \quad & \hat{H}_0(\hat{\mathbf{R}},\hat{\mathbf{P}})\left|0\right\rangle\!\left\langle 0\right| + \hat{H}_1(\hat{\mathbf{R}},\hat{\mathbf{P}})\left|1\right\rangle\!\left\langle 1\right| + V_{01}\left|0\right\rangle\!\left\langle 1\right| + V_{10}\left|1\right\rangle\!\left\langle 0\right|, \\ \text{with,} \quad & \hat{H}_0(\hat{\mathbf{R}},\hat{\mathbf{P}}) = \epsilon + \sum_{k=1}^{N_n}\frac{\hat{P}_k^2}{2} + \frac{1}{2}\omega_k^2\hat{R}_k^2 - c_k\hat{R}_k \\ & \hat{H}_1(\hat{\mathbf{R}},\hat{\mathbf{P}}) = -\epsilon + \sum_{k=1}^{N_n}\frac{\hat{P}_k^2}{2} + \frac{1}{2}\omega_k^2\hat{R}_k^2 + c_k\hat{R}_k \\ & V_{01} = V_{10} = \Gamma, \end{aligned} \tag{II.27}$$

Here we will use N_n to represent the number of nuclear DOF and N_e to represent the number of electronic DOF. 2ϵ represents the equilibrium energy bias of the two states. Γ represents the elec-

tronic coupling between the two states. ω_k and c_k represent nuclear mode frequency and coupling coefficient, respectively, and are sampled from an Ohmic spectral density with exponential cutoff:

$$J(\omega) = \frac{\pi}{2}\hbar\xi\omega e^{-\omega/\omega_c}. \tag{II.28}$$

Here, ξ is the Kondo parameter, which roughly describes the friction, and ω_c is the cutoff frequency. To sample ω_k and c_k, we consider the folllowing relation when $N_n \to \infty$:

$$J(\omega) = \frac{\pi}{2}\sum_{k=1}^{N_n}\frac{c_k^2}{\omega_k}\delta(\omega-\omega_k) \xrightarrow[N_n\to\infty]{} \frac{\pi}{2}\hbar\xi\omega e^{-\omega/\omega_c}, \tag{II.29}$$

$$c_k = \sqrt{\xi\hbar\Delta\omega}\omega_k, \quad \Delta\omega = \frac{\omega_c}{N_n}(1-e^{-\frac{\omega_{max}}{\omega_c}}), \tag{II.30}$$

$$\omega_k = -\omega_c \ln\left(1-k\frac{\Delta\omega}{\omega_c}\right). \tag{II.31}$$

In this walkthrough, we will set up the initial state of the spin-boson to be:

$$\hat{\rho}(0) = |0\rangle\langle 0| \otimes \hat{\rho}_{\mathrm{n}}(0), \tag{II.32}$$

$$\hat{\rho}_{\mathrm{n}}(0) = \frac{e^{-\beta(\hat{H}_D+\hat{H}_A)/2}}{\mathrm{Tr}_n\left\{e^{-\beta(\hat{H}_D+\hat{H}_A)/2}\right\}}. \tag{II.33}$$

II.4.2 Applying LSCI to Describe the Observable of Interest

In this demonstration, our observable of interest is the electronic reduced density matrix as in Eq. II.2. Applying the LSC approximation Eq. II.10 to the correlation function Eq. II.4 results in the following QC approximation:

$$\sigma_{mn}(t) = \frac{1}{(2\pi\hbar)^{N_e+N_n}}\iiiint d\mathbf{R}(0)d\mathbf{P}(0)d\mathbf{q}(0)d\mathbf{p}(0)[\hat{\rho}_n(0)]_W(\mathbf{R}(0),\mathbf{P}(0)) \times[|0\rangle\langle 0|]_W(\mathbf{q}(0),\mathbf{p}(0)) \times [|n\rangle\langle m|]_W(\mathbf{q}(0),\mathbf{p}(0)). \tag{II.34}$$

Here, the Wigner transform of $\hat{\rho}_{\mathrm{n}}(0)$, $[\hat{\rho}_n(0)]_W(\mathbf{R}(0),\mathbf{P}(0))$ is:

$$\rho_{\mathrm{n,w}}(0)=\prod_{k=1}^{N_n}2tanh(\beta\hbar\omega_k/2)\exp\left\{-\frac{2tanh(\beta\hbar\omega_k/2)}{\hbar\omega_k}\left(\frac{1}{2}P_k(0)^2+\frac{1}{2}\omega_k^2R_k(0)^2\right)\right\}, \quad \text{(II.35)}$$

Applying LSCI as presented in Table II.1 and Eq. II.35 to Eq. II.34

$$\begin{aligned}\sigma_{mn}(t)= \quad & \frac{1}{(2\pi\hbar)^{N_e+N_n}}\iiiint d\mathbf{R}(0)d\mathbf{P}(0)d\mathbf{q}(0)d\mathbf{p}(0)\\ &\times\prod_{k=1}^{N_n}2tanh(\beta\hbar\omega_k/2)\exp\left\{-\frac{2tanh(\beta\hbar\omega_k/2)}{\hbar\omega_k}\left(\frac{1}{2}P_k(0)^2+\frac{1}{2}\omega_k^2R_k(0)^2\right)\right\}\\ &\times\frac{2^3}{\hbar}e^{-(q_0^2(0)+q_1^2(0)+p_0^2(0)+p_1^2(0))/\hbar}\left(q_0^2(0)+p_0^2(0)-\frac{\hbar}{2}\right)\\ &\times\frac{1}{2\hbar}(q_m^2(t)+p_m^2(t)-\hbar), \qquad \text{if } m=n \end{aligned} \quad \text{(II.36)}$$

$$\begin{aligned}\sigma_{mn}(t)= \quad & \frac{1}{(2\pi\hbar)^{N_e+N_n}}\iiiint d\mathbf{R}(0)d\mathbf{P}(0)d\mathbf{q}(0)d\mathbf{p}(0)\\ &\times\prod_{k=1}^{N_n}2tanh(\beta\hbar\omega_k/2)\exp\left\{-\frac{2tanh(\beta\hbar\omega_k/2)}{\hbar\omega_k}\left(\frac{1}{2}P_k(0)^2+\frac{1}{2}\omega_k^2R_k(0)^2\right)\right\}\\ &\times\frac{2^3}{\hbar}e^{-(q_0^2(0)+q_1^2(0)+p_0^2(0)+p_1^2(0))/\hbar}\left(q_0^2(0)+p_0^2(0)-\frac{\hbar}{2}\right)\\ &\times\frac{1}{2\hbar}(q_n(t)-ip_n(t))(q_m(t)+ip_m(t)). \qquad \text{if } m\neq n \end{aligned} \quad \text{(II.37)}$$

The above expression can be considered as the expectation value of a function $g(\mathbf{R}(0),\mathbf{P}(0),\mathbf{q}(0),\mathbf{p}(0);\mathbf{q}(t),\mathbf{p}(t))$, with $\mathbf{R}(0),\mathbf{P}(0),\mathbf{q}(0),\mathbf{p}(0)$ following a continuous Gaussian distribution. The probability density function of Gaussian distribution is:

$$f(x)=\frac{1}{\sigma\sqrt{2\pi}}e^{-\frac{1}{2}(\frac{x-\mu}{\sigma})^2}, \quad \text{(II.38)}$$

with σ as the standard deviation and μ as the mean. The expecation value of a function $g(x)$ is:

$$\langle g(x)\rangle=\int dxg(x)f(x). \quad \text{(II.39)}$$

To calculate Eq. II.36 and II.37, we sample $\mathbf{R}(0), \mathbf{P}(0), \mathbf{q}(0), \mathbf{p}(0)$ from the corresponding Gaussian distribution, and then calculate the integral as the expectation value of the function of random variables $g(\mathbf{R}(0), \mathbf{P}(0), \mathbf{q}(0), \mathbf{p}(0); \mathbf{q}(t), \mathbf{p}(t))$. In Table II.2, we show the corresponding mean, standard deviation, and the function of random variable $g(\mathbf{R}(0), \mathbf{P}(0), \mathbf{q}(0), \mathbf{p}(0), \mathbf{q}(t), \mathbf{p}(t))$ used to calculate the observables $\sigma_{mn}(t)$.

Mean and Standard Distribution Used in Sampling				
	R_k	P_k	q_i	p_i
Mean	0	0	0	0
Standard deviation	$\sqrt{\frac{\hbar}{2\omega_k tanh(\beta\hbar\omega_k/2)}}$	$\sqrt{\frac{\hbar\omega_k}{2tanh(\beta\hbar\omega_k/2)}}$	$\sqrt{\frac{\hbar}{2}}$	$\sqrt{\frac{\hbar}{2}}$
Corresponding Function of Random Variables $g(\mathbf{R}(0), \mathbf{P}(0), \mathbf{q}(0), \mathbf{p}(0); \mathbf{q}(t), \mathbf{p}(t))$				
$\sigma_{mm}(t)$ as in Eq. II.36	$\frac{2}{\hbar}\left(q_0^2(0) + p_0^2(0) - \frac{\hbar}{2}\right)\frac{1}{2\hbar}(q_m^2(t) + p_m^2(t) - \hbar)$			
$\sigma_{mn}(t)$ as in Eq. II.37	$\frac{2}{\hbar}\left(q_0^2(0) + p_0^2(0) - \frac{\hbar}{2}\right)\frac{1}{2\hbar}(q_n(t) - ip_n(t))(q_m(t) + ip_m(t))$			

Table II.2: Summary of the coefficients of the Gaussian sampling and the corresponding function of random variable for implementing Eq. II.36 and II.37.

II.4.3 Time Propagation Methods

We see that there are time dependent mapping variables $\mathbf{p}(t)$ and $\mathbf{q}(t)$ in the presented $g(\mathbf{R}(0), \mathbf{P}(0), \mathbf{q}(0), \mathbf{p}(0))$. As described above, treating all variables classically, we use Hamilton's equation to derive the equation of motion(EOM) of variables $\mathbf{R}(t)$, $\mathbf{P}(t)$, $\mathbf{q}(t)$, $\mathbf{p}(t)$. In practice, we symmetrize the Hamiltonian to improve numerical stability[36, 79]. By applying the closure relation $\sum_{i=1}^{N_e} |i\rangle\langle i| = 1$, we can rewrite the Hamiltonian as:

$$\begin{aligned} H(\mathbf{R}(t), \mathbf{P}(t), \mathbf{q}(t), \mathbf{p}(t)) \; &= \bar{H}(\mathbf{R}(t), \mathbf{P}(t)) + \sum_{\substack{j,k=1 \\ k\neq j}}^{N_e} H_{jk}(\mathbf{R}(t), \mathbf{P}(t))[\,|j\rangle\langle k|\,]_W(\mathbf{q}(t), \mathbf{p}(t)) \\ &+ \sum_{i=1}^{N_e} \left[H_{ii}(\mathbf{R}(t), \mathbf{P}(t)) - \bar{H}(\mathbf{R}(t), \mathbf{P}(t))\right][\,|i\rangle\langle i|\,]_W(\mathbf{q}(t), \mathbf{p}(t)) \;\; . \end{aligned} \tag{II.40}$$

with $\bar{H}(\mathbf{R}(t),\mathbf{P}(t)) = \frac{1}{N_e}\sum_{i=1}^{N_e} H_{ii}(\mathbf{R}(t),\mathbf{P}(t))$. It should be noted that the symmetrized form of the mapping Hamiltonian, Eq. (II.40), is obtained by rewriting $H_{ii}(\mathbf{R}(t))$ as $\bar{H}(\mathbf{R}(t)) + [H_{ii}(\mathbf{R}(t)) - \bar{H}(\mathbf{R}(t))]$, where $\bar{H}(\mathbf{R}(t)) = \frac{1}{N_e}\sum_{i=1}^{N_e} H_{ii}(\mathbf{R}(t))$, and using the closure relation, $\sum_{i=1}^{N_e} |i\rangle\langle i| = \hat{1}$. This is a standardized procedure that was also used in many previous studies[36, 42, 43, 79, 85, 86]. For the two-level spin-boson model, after we map the electronic states as mapping #1 in Table II.1, the Hamiltonian becomes:

$$\begin{aligned} H(t) = \quad & H_0(\mathbf{R}(t),\mathbf{P}(t))\frac{1}{2\hbar}(q_0(t)^2 + p_0(t)^2 - \hbar) + H_1(\mathbf{R}(t),\mathbf{P}(t))\frac{1}{2\hbar}(q_1(t)^2 + p_1(t)^2 - \hbar) \\ & + V_{01}\frac{1}{2\hbar}(q_0(t) - ip_0(t))(q_1(t) + ip_1(t)) + V_{10}\frac{1}{2\hbar}(q_1(t) - ip_1(t))(q_0(t) + ip_0(t)) \\ & + \bar{H}(\mathbf{R}(t),\mathbf{P}(t)) \end{aligned} \tag{II.41}$$

$$\begin{aligned} \text{with,} \quad & H_0(\mathbf{R}(t),\mathbf{P}(t)) = \epsilon - \sum_{k=1}^{N_n} c_k R_k(t), \qquad H_1(\mathbf{R}(t),\mathbf{P}(t)) = -\epsilon + \sum_{k=1}^{N_n} c_k R_k(t) \\ & \bar{H}(\mathbf{R}(t),\mathbf{P}(t)) = \sum_{k=1}^{N_n} \frac{P_k^2(t)}{2} + \frac{1}{2}\omega_k^2 R_k^2(t), \qquad V_{01} = V_{10} = \Gamma \end{aligned}$$

Applying Hamilton's equation, the resulting EOM are:

$$\begin{aligned} \dot{q}_0(t) &= \frac{1}{\hbar}\left(\epsilon - \sum_{k=1}^{N_n} c_k R_k(t)\right) p_0(t) + \frac{1}{\hbar}\Gamma p_1(t) \\ \dot{p}_0(t) &= -\frac{1}{\hbar}\left(\epsilon - \sum_{k=1}^{N_n} c_k R_k(t)\right) q_0(t) - \frac{1}{\hbar}\Gamma q_1(t) \\ \dot{q}_1(t) &= \frac{1}{\hbar}\left(-\epsilon + \sum_{k=1}^{N_n} c_k R_k(t)\right) p_1(t) + \frac{1}{\hbar}\Gamma p_0(t) \\ \dot{p}_1(t) &= -\frac{1}{\hbar}\left(-\epsilon + \sum_{k=1}^{N_n} c_k R_k(t)\right) q_1(t) - \frac{1}{\hbar}\Gamma q_0(t) \\ \dot{R}_k(t) &= P_k(t) \\ \dot{P}_k(t) &= \frac{1}{2\hbar} c_k \left(q_0(t)^2 + p_0(t)^2 - q_1(t)^2 - p_1(t)^2\right) - \omega_k^2 R_k(t) \end{aligned} \tag{II.42}$$

One viable scheme for numerical integration of Eq. II.42 is to propagate $\mathbf{q}$ and $\mathbf{p}$ using forward Euler method, and propagate $\mathbf{R}$ and $\mathbf{P}$ using Verlet.

The forward euler numerical integration for a differential equation $\frac{dy(t)}{dt} = f(t, y)$ is:

$$y_{n+1} = y_n + \Delta t f(t, y_n) \tag{II.43}$$

The Verlet integration method is:

$$\begin{aligned} x(t + \Delta t) &= x(t) + v(t)\Delta t + \frac{1}{2}a(t)\Delta t^2 \\ a(t + \Delta t) &= f(x(t + \Delta t)) \\ v(t + \Delta t) &= v(t) + \frac{1}{2}(a(t) + a(t + \Delta t))\Delta t, \end{aligned} \tag{II.44}$$

with $a(t) = f(x(t))$ being acceleration, $x(t)$ being position and $v(t)$ being velocity.

The propagation scheme to propagate from t to $t + \Delta t$ is described as:

propagate $\mathbf{q}$(t), $\mathbf{p}$(t) to $\mathbf{q}(t + 0.5\Delta t)$, $\mathbf{p}(t + 0.5\Delta t)$ using forward Euler

$q_0(t + 0.5\Delta t) = q_0(t) + 0.5\Delta t \times \dot{q}_0(t)$

$p_0(t + 0.5\Delta t) = p_0(t) + 0.5\Delta t \times \dot{p}_0(t)$

$q_1(t + 0.5\Delta t) = q_1(t) + 0.5\Delta t \times \dot{q}_1(t)$

$p_1(t + 0.5\Delta t) = p_1(t) + 0.5\Delta t \times \dot{p}_1(t)$

#propagate $\mathbf{R}$(t), $\mathbf{P}$(t) to $\mathbf{R}(t + \Delta t)$, $\mathbf{P}(t + \Delta t)$ using Verlet

$R_k(t + \Delta t) = R_k(t) + P_k(t) \times \Delta t + \frac{1}{2}\dot{P}_k(t)\Delta t^2$

Calculate $\dot{P}_k(t + \Delta t)$ with the new $R_k(t + \Delta t)$

$P_k(t + \Delta t) = P_k(t) + \frac{1}{2}(\dot{P}_k(t) + \dot{P}_k(t + \Delta t))\Delta t$

propagate $\mathbf{q}(t + 0.5\Delta t)$, $\mathbf{p}(t + 0.5\Delta t)$ to $\mathbf{q}(t + \Delta t)$, $\mathbf{p}(t + \Delta t)$ using forward Euler

$q_0(t + \Delta t) = q_0(t + 0.5\Delta t) + 0.5\Delta t \times \dot{q}_0(t)$

$p_0(t + \Delta t) = p_0(t + 0.5\Delta t) + 0.5\Delta t \times \dot{p}_0(t)$

$q_1(t + \Delta t) = q_1(t + 0.5\Delta t) + 0.5\Delta t \times \dot{q}_1(t)$

$p_1(t + \Delta t) = p_1(t + 0.5\Delta t) + 0.5\Delta t \times \dot{p}_1(t)$

An alternative way to propagate the electronic DOF is through explicit diagonalization. Similar

to previously described in Sec. II.3.1.1, we define the corresponding electronic wave function at time t as:

$$|\psi(t)\rangle = c_0(t)\,|0\rangle + c_1(t)\,|1\rangle\,. \tag{II.45}$$

In Meyer-Miller mapping, the coefficients can be mapped as:

$$c_i(t) = \frac{1}{\sqrt{2}}(q_k + ip_k). \tag{II.46}$$

In the Schrodinger picture, the coefficients at time t are:

$$c_i(t + \Delta t) = e^{-iH\Delta t/\hbar}c_i(t), \tag{II.47}$$

with $U(t) = e^{-iH\Delta t/\hbar}$ as the propagator. Because H is a hermitian matrix, we can diagonalize H to be $Q\Lambda Q^{-1}$. With the eigendecomposition, we can express the propagator as:

$$U(t) = Qe^{-i\Lambda\Delta t/\hbar}Q^{-1}. \tag{II.48}$$

Since the exponential of a diagonal matrix is simply the matrix of the exponential of each diagonal term, we can then easily calculate the propagator. Plugging in Eq. II.46, we can propagate $q_k(t)$ and $p_k(t)$ with $U(t)$:

$$q_k(t + \Delta t) + ip_k(t + \Delta t) = Qe^{-i\Lambda\Delta t/\hbar}Q^{-1}(q_k(t) + ip_k(t)). \tag{II.49}$$

Replacing forward Euler with this explicit diagonalization method can help improve accuracy and numerical stability.

II.4.4 Pseudo Code

In summary, to apply LSCI on a two-level spin-boson model, we first use Gaussian sampling to gather initial $\mathbf{R}$, $\mathbf{P}$, $\mathbf{q}$ and $\mathbf{p}$, and then use explicit diagonalization or forward Euler to propagate $\mathbf{q}$, $\mathbf{p}$ and verlocity Verlet to propagate $\mathbf{R}$, $\mathbf{P}$. The observables of interest are calculated by taking the average of the function of random variables. The pseudo-code of the algorithm is presented below.

```
#system and bath parameters
initialize parameters: gamma, epsilon, c, omega, beta, DOFe, DOFn
#stepsize of propagation, final time, # of trajectories
initialize parameters: dt, t_final, Ntraj
#store the electronic density matrix
initialize sigma as nt*DOFe*DOFe 3D array
for i in range(Ntraj):
    #initial sampling
    Gaussian sampling DOFn sets of R(0), P(0) according to Table II.2
    Gaussian sampling DOFe sets of q(0), p(0) according to Table II.2
    #calculate the function of random variable for the observable at t=0
    #defined in Table II.2
    sigma[0] += g(R(0),P(0),q(0),p(0);q(0),p(0))/Ntraj
    for n from 1 to t_final:
        #propagate the system one step further
        #with explicit diagonalization
        propagate q(ndt), p(ndt) to q((n+0.5)dt), p((n+0.5)dt)
        #with Verlet
        propagate R(ndt), P(ndt) to R((n+1)dt), P((n+1)dt)
        #with explicit diagonalization
        propagate q((n+0.5)dt), p((n+0.5)dt) to q((n+1)dt), p((n+1)dt)
        #calculate the function of random variable for the observable at time t
```

```
        sigma[t] += g(R(0),P(0),q(0),p(0);q((n+1)dt),p((n+1)dt))/Ntraj
        # as defined in Table II.2
print out observable
```

II.5 Results for the Spin-Boson Model

In this section, we present results for the two-level spin-boson model described prior (with Hamiltonian defined as Eq. II.27) with the four sets of parameters presented in Table II.3. These four sets of parameters represent both symmetric & asymmetric cases and also high and low temperature cases.

Table II.3: Spin-boson Model and Simulation Parameters

	Model Parameters					Numerical Parameters			
Model #	ϵ	Γ	β	ξ	ω_c	ω_{max}	N_n	Δt	N_{traj}
A	0.0	1.0	0.1	0.09	2.5	12.0	400	0.005	3×10^6
B	0.0	1.0	5.0	0.09	2.5	12.0	400	0.005	3×10^6
C	1.0	1.0	0.25	0.1	1.0	5.0	400	0.005	3×10^6
D	1.0	1.0	5.0	0.1	2.0	10.0	400	0.005	3×10^6

For spin-boson model, we are interested in the Pauli matrices $\hat{\sigma}_x$, $\hat{\sigma}_y$, and $\hat{\sigma}_z$. These are defined as:

$$\hat{\sigma}_x = \begin{pmatrix} 0 & 1 \\ 1 & 0 \end{pmatrix}, \hat{\sigma}_y = \begin{pmatrix} 0 & -i \\ i & 0 \end{pmatrix}, \hat{\sigma}_z = \begin{pmatrix} 1 & 0 \\ 0 & -1 \end{pmatrix}. \tag{II.50}$$

These matrices are electronic observables. For a electronic density operator $\hat{\sigma}$, the expectation

value of any electronic observable $\hat{A}$ can be calculated with:

$$\left\langle \hat{A} \right\rangle = \mathrm{Tr}\{\hat{\sigma}\hat{A}\} \tag{II.51}$$

Therefore, for the two-level spin-boson model, the expectation value of the Pauli matrices are calculated as:

$$\langle \hat{\sigma}_x \rangle = \sigma_{01} + \sigma_{10}, \quad \langle \hat{\sigma}_y \rangle = i\sigma_{01} - i\sigma_{10}, \quad \langle \hat{\sigma}_z \rangle = \sigma_{00} - \sigma_{11}. \tag{II.52}$$

The simulated dynamics of $\langle \hat{\sigma}_x \rangle$, $\langle \hat{\sigma}_y \rangle$, $\langle \hat{\sigma}_z \rangle$ for the two-level spin-boson model is shown in Figure II.1. The quantum-mechanically exact results were calculated via the dissipation equation of motion (DEOM) method of Yan et al[23]. A summary of the accuracy of the QC/MH methods is shown in Table II.4.

Spin-boson Model	A symmetric/high T			B symmetric/low T			C asymmetric/low T			D asymmetric/low T		
QC/MH	$\langle\sigma_x\rangle$	$\langle\sigma_y\rangle$	$\langle\sigma_z\rangle$	$\langle\sigma_x\rangle$	$\langle\sigma_y\rangle$	$\langle\sigma_z\rangle$	$\langle\sigma_x\rangle$	$\langle\sigma_y\rangle$	$\langle\sigma_z\rangle$	$\langle\sigma_x\rangle$	$\langle\sigma_y\rangle$	$\langle\sigma_z\rangle$
LSCI	×	√	√	×	√	√	×	√	×	×	√	×
LSCII	×	√	√	×	√	√	×	√	×	×	√	×
MF	×	√	√	×	√	√	×	√	×	×	×	×
mLSC/$\phi^1\phi^1$	√	√	√	×	√	√	√	√	√	×	√	√
mLSC/$\phi^1\phi^2$	√	√	√	×	√	√	√	√	√	×	√	√
mLSC/$\phi^2\phi^2$	√	√	√	×	√	√	√	√	√	√	√	√
SQC	×	√	√	×	√	√	√	√	√	×	√	√

Table II.4: Summary of the accuracy of dynamics of the two-level spin-boson model via QC/MH methods reported in Ref. 85. √ indicates that the method is accurate and × indicates that the method is inaccurate. The simulated dynamics with SQC can be found in Ref. [85].

We observed that overall LSCI, LSCII, and Ehrenfest methods are the least accurate methods. Although these methods can provide well-enough description for $\langle \hat{\sigma}_y(t) \rangle$ for all four systems and $\langle \hat{\sigma}_z(t) \rangle$ for the high-temperature, symmetric model, this is not the case for $\langle \hat{\sigma}_x(t) \rangle$. The modified

LSC methods: mLSC/$\phi^1\phi^1$, mLSC/$\phi^1\phi^2$, and mLSC/$\phi^2\phi^2$ provides the most accurate description. It is worth mentioning that for model B, the symmetric low T case, mLSC/$\phi^2\phi^2$ is the best method among all QC/MH methods in simulating the dynamics of $\langle\hat{\sigma}_x(t)\rangle$. As can be conclude from Eq. II.52, by assessing the expectation value of these Pauli matrices, we are assessing the ability of these methods to describe the overall density matrix, instead of only assessing the dynamics of the populations. We also see that even if a method has the capability of describing population dynamics well, it does not necessarily mean that the method can describe the dynamics of coherences well. These results point to mLSC/$\phi^1\phi^1$, mLSC/$\phi^1\phi^2$, and mLSC/$\phi^2\phi^2$ as the methods of choice, since they are more accurate and do not involve choices regarding window shape and width in SQC.

II.6 Concluding Remarks

In this chapter, we discussed various quasi-classical mapping Hamiltonian methods. These include linearized semi-classical approximation; modified LSC, which preserves the trace of the electronic density matrix for each trajectory; symmetrical quasi-classical approach, which was formulated based on the action-angle variables. The SQC approach requires choosing the window shape and size. In the LSC approach, which utilized two ways of mapping, one corresponds to the creation and annihilation operators, and the other one corresponds to the singly excited harmonic oscillators. Because the exact quantum dynamics is restricted to the singly-excited subspace of the oscillator Hilbert space, if the electronic states are treated fully quantum-mechanically, the two mappings would lead to the same results. The connection between LSC and MF was also discussed in this chapter. In simple terms, MF can be done via LSC procedures with no sampling but a fixed value for the initial auxiliary electronic $\mathbf{q}$ and $\mathbf{p}$.

We then demonstrated the application of LSCI to describe the reduced density matrix of a two-level spin-boson model. Detailed descriptions of the initial sampling process and the numerical integration process were included. The forward Euler can be used as the most straightforward numerical integration method. A combination of explicit diagonalization for electronic DOF and the

Verlet method for nuclear DOF will allow more accurate numerical integration. A pseudo-code for the implementation was also presented. Following this, we presented the resulting dynamics of applying the QC/MH method to the two-level spin-boson model. We observed that, across the board, mLSC/$\phi^2\phi^2$ provides the most accurate descriptions of the dynamics. The results emphasized the importance of using the overall density matrix to evaluate method accuracy, due to the inconsistency in the performance of QC/MH methods for different electronic observables.

As we have seen above, most quasi-classical mapping Hamiltonian methods failed to provide accurate descriptions for $\langle\hat{\sigma}_x\rangle$, and LSCI, LSCII, and MF cannot provide good descriptions for $\langle\hat{\sigma}_z\rangle$. This prompt for modification of these methods in an attempt to improve accuracy. One study by Gao and Geva focuses on modifying the constant terms in the mapping formula and has shown accurate simulation for various charge and energy transfer systems.[90] Using QC/MH methods to generate projection-free inputs for the generalized quantum master equation can be a good alternative route.[67–70, 91, 92] We will explore this route in Chapter III

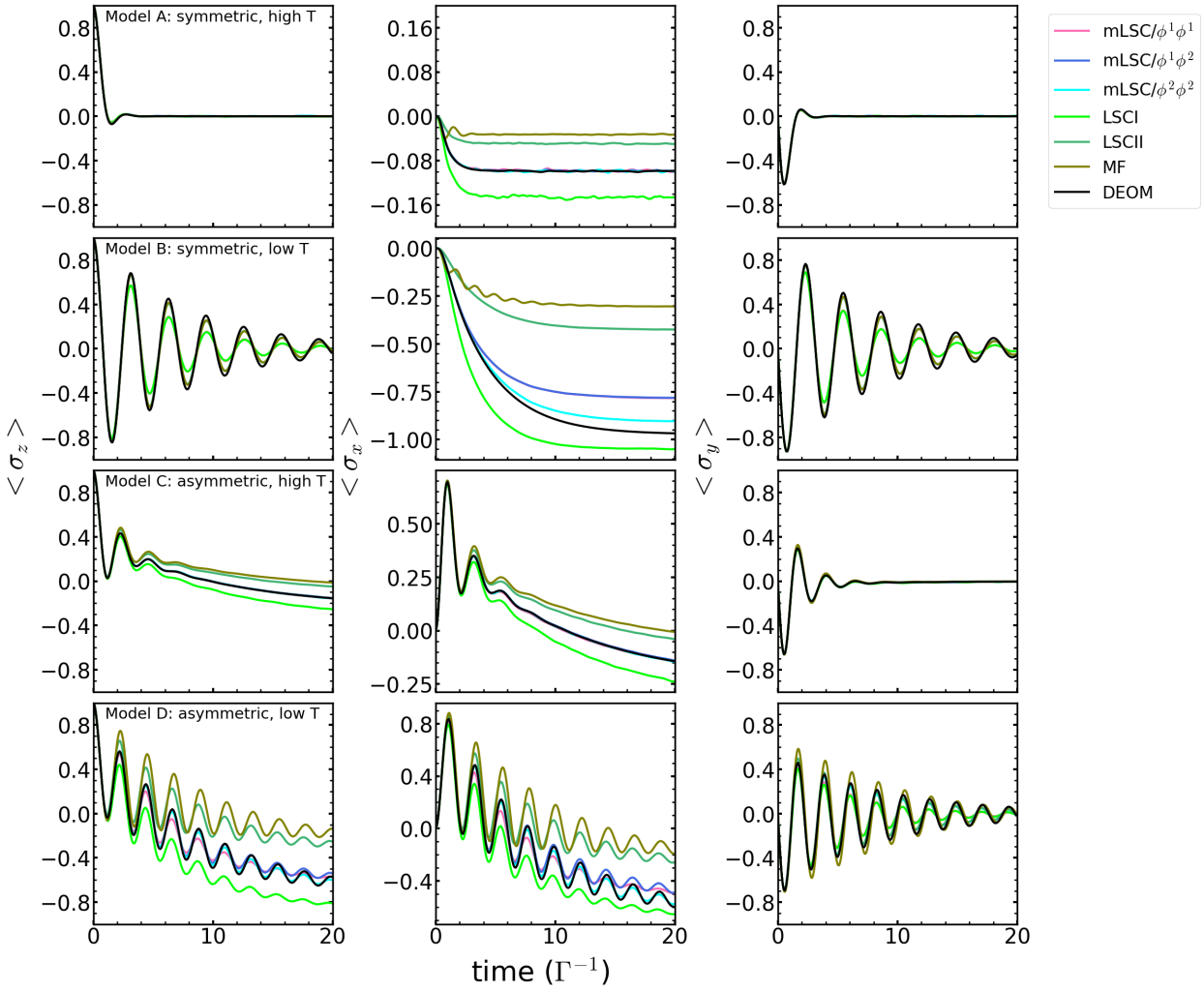

Figure II.1: Dynamics of two-level spin-boson model simulated with LSC, modified LSC, and MF. Model parameters are set according to Table II.3. The DEOM results, represented by the black line, give the exact dynamics. The expectation value of $\hat{\sigma}_x$, $\hat{\sigma}_y$ and $\hat{\sigma}_z$ is described in Eq. II.52. The simulated dynamics with SQC for the same four types of two-level spin-boson model can be found in Ref. [85].

CHAPTER III

The Modified Generalized Quantum Master Equation Approach

III.1 Introduction

The Master equation typically refers to first-order differential equations describing the time evolution. The Redfield equation is a Markovian master equation that describes the time evolution of the reduced density matrix.[62] The Redfield equation is a second-order perturbation treatment in the system-bath coupling. Therefore, it is best for models with weak system-bath coupling. The Redfield theory is closely connected to the Lindblad master equation, and both methods assume Markovian. Markovian approximation ignores the effect of memory, meaning that the future of the system of interest is not affected by the past.

The Nakajima-Zwanzig generalized quantum master equation (NZ-GQME) arises from the quantum Liouville equation. The benefit of NZ-GQME is that it accounts for the non-Markovian effects. The quantum Liouvile equation describes the dynamics of the overall density matrix. The quantum Liouville equation again scales exponentially with the dimension of the systems. By projecting the quantum Liouville equation, the NZ-GQME reduces the dimensionality and thereby reduces the computational costs. The NZ-GQME described the time evolution of the projected density matrix, and the effect of the rest of the system on the projected density matrix is incorporated in the memory kernels.

A formally exact formulation for generating the memory kernels with only projection-free in-

puts was proposed by Shi and Geva.[63] The accuracy of this approach is demonstrated with quantum-mechanically exact inputs and semi-classical inputs for the spin-boson model.[63, 64] The Zhang-Ka-Geva approach was introduced to account for arbitrary initial state and system-bath coupling. This new approach can accommodate a wide range of projection operators.[65] The capability of Shi-Geva GQME was further demonstrated with projection-free inputs generated using surface hopping[66] and Ehrenfest mean field methods[67].

The Shi-Geva approach requires expressing the Hamiltonian in a system-bath form. The modified approach to GQME that was proposed by Mulvihill et al eliminates the restriction on the form of Hamiltonian, making the GQME more generally applicable.[68] The reduced-dimensionality GQME was proposed to furtherly reduce the computational costs.[70]

In this chapter, we will focus on the general form of the modified GQME approach that accounts for a general choice of projection operators. More particularly, we will focus on evaluating the ability of GQME in describing the dynamics of the coherences of GQME. The rest of this chapter is organized as follows. We first discuss some preliminary considerations in Sec. III.2. Then the modified GQME approach with a general choice of projection operator in the Liouville space is outlined in Sec. III.3. In Sec. III.4, we use the two-level spin-boson model to demonstrate the application of GQME using QC/MH-generated projection inputs. In the next section, we present the simulation results of the coherence dynamics of the two-level spin-boson model, compared to the dynamics generated with the dissipation equation of motion (DEOM). Concluding remarks are given in section III.6.

III.2 Preliminary Considerations

In what follows, we focus on simulating the dynamics of electronic coherences in molecular systems whose overall Hamiltonian has the following commonly encountered form:

$$\hat{H} = \sum_{j=1}^{N_e} \hat{H}_j |j\rangle\langle j| + \sum_{\substack{j,k=1 \\ k\neq j}}^{N_e} \hat{V}_{jk} |j\rangle\langle k|. \tag{III.1}$$

Here, $\hat{H}_j = \hat{\mathbf{P}}^2/2 + V_j\left(\hat{\mathbf{R}}\right)$ is the nuclear Hamiltonian when the system is in the diabatic electronic state $|j\rangle$, with the index j running over the N_e electronic states; $\left\{\hat{V}_{jk}|j \neq k\right\}$ are coupling terms between electronic states (which can be either nuclear operators or constants); and $\hat{\mathbf{R}} = \left(\hat{R}_1, ..., \hat{R}_{N_n}\right)$ and $\hat{\mathbf{P}} = \left(\hat{P}_1, ..., \hat{P}_{N_n}\right)$ are the mass-weighted position and momentum operators of the $N_n \gg 1$ nuclear DOF. Throughout this chapter, boldfaced variables, e.g., $\mathbf{A}$, indicate vector quantities; a hat over a variable, e.g., $\hat{B}$, indicates an operator quantity; a double braket, e.g. $|\rho\rangle\rangle$ and $\langle\langle\rho|$, indicate ket and bra in Liouville space, respectively; and calligraphic font, e.g., $\mathcal{L}$, indicates a Liouville space superoperator.

We also assume that the initial state of the overall system is of the following single product form:

$$|\rho(0)\rangle\rangle = |\rho_n(0)\rangle\rangle \otimes |\sigma(0)\rangle\rangle \quad . \tag{III.2}$$

Here, $|\rho(0)\rangle\rangle$ is the Liouville space ket that corresponds to the overall system initial density operator, $\hat{\rho}(0)$; $|\rho_n(0)\rangle\rangle$ is the Liouville space ket that corresponds to the reduced density operator that describes the initial state of the nuclear DOF, $\hat{\rho}_n(0) = \text{Tr}_e\{\hat{\rho}(0)\}$; $|\sigma(0)\rangle\rangle$ is the Liouville space ket that corresponds to the reduced density operator that describes the initial state of the electronic DOF, $\hat{\sigma}(0) = \text{Tr}_n\{\hat{\rho}(0)\}$ [$\text{Tr}_e\{\cdot\}$ and $\text{Tr}_n\{\cdot\}$ stand for partially tracing over the electronic Hilbert space and the nuclear Hilbert space, respectively].

Given the overall system Hamiltonian and initial state in Eqs. (III.1) and (III.2), respectively, the overall system state at a later time t is given by:

$$|\rho(t)\rangle\rangle = e^{-i\mathcal{L}t/\hbar}\,|\rho_n(0)\rangle\rangle \otimes |\sigma(0)\rangle\rangle\,. \tag{III.3}$$

Here, $\mathcal{L}(\cdot) = [\hat{H}, \cdot]$ is the Liouvillian superoperator, with $\hat{H}$ the overall Hamiltonian given in Eq. (III.1). The electronic state at time t is given by

$$|\sigma(t)\rangle\rangle = \sum_{j,k=1}^{N_e} \sigma_{jk}(t)\,|jk\rangle\rangle \quad , \tag{III.4}$$

where $|\sigma(t)\rangle\rangle$ and $|jk\rangle\rangle$ are the Liouville space kets that correspond to the reduced electronic density operator $\hat{\sigma}(t) = \mathrm{Tr}_n\{\hat{\rho}(t)\}$ and the electronic operator $|j\rangle\langle k|$, respectively. The electronic populations and coherences, whose time evolution underlies decoherence as well as energy, charge, and coherence transfer dynamics, are given by $\{\sigma_{jj}(t) = \langle j|\hat{\sigma}(t)|j\rangle \equiv \langle\langle jj|\sigma(t)\rangle\rangle\}$ and $\{\sigma_{jk}(t) = \langle j|\hat{\sigma}(t)|k\rangle = \langle\langle kj|\sigma(t)\rangle\rangle\}$ with $j \neq k$, respectively.

In previous studies, the main focus was simulating the dynamics of the electronic populations within a GQME approach.[68–70] In this chapter, we focus on simulating the dynamics of the electronic coherences via the GQME approach.

It should be noted that the distinction between electronic populations, which correspond to the diagonal elements of the electronic reduced density matrix, and the electronic coherences, which correspond to the off-diagonal elements of the electronic reduced density matrix, is *basis-dependent*. To see this, note that the real and imaginary parts of the coherence $\{\sigma_{jk}(t)\}$ in terms of the diabatic basis $\{|j\rangle\}$ can be written in terms of the expectation values of the following hermitian operators:

$$\hat{X}_{jk} = \frac{1}{2}\left(|j\rangle\langle k| + |k\rangle\langle j|\right) \equiv \sum_{l=1}^{N_e} \lambda_l |\lambda_l\rangle\langle\lambda_l| \tag{III.5}$$

$$\hat{Y}_{jk} = \frac{1}{2i}\left(|j\rangle\langle k| - |k\rangle\langle j|\right) \equiv \sum_{l=1}^{N_e} \kappa_l |\kappa_l\rangle\langle\kappa_l| \ , \tag{III.6}$$

where $\{\lambda_l\}$ and $\{|\lambda_l\rangle\}$ are the eigenvalues and eigenfunctions of $\hat{X}_{jk}$, respectively, such that $\hat{X}_{jk}|\lambda_l\rangle = \lambda_l|\lambda_l\rangle$, and $\{\kappa_l\}$ and $\{|\kappa_l\rangle\}$ are the eigenvalues and eigenfunctions of $\hat{Y}_{jk}$, respectively, such that $\hat{Y}_{jk}|\kappa_l\rangle = \kappa_l|\kappa_l\rangle$. Thus, the real and imaginary parts of the *off-diagonal* matrix element $\sigma_{jk}(t)$ in terms of the $\{|j\rangle\}$ basis can be written in terms of *diagonal* matrix elements in terms of the $\{|\lambda_l\rangle\}$ and $\{|\kappa_l\rangle\}$ bases:

$$\mathrm{Re}[\sigma_{jk}(t)] = Tr_e\left[\hat{\sigma}(t)\hat{X}_{jk}\right] \equiv \sum_{l=1}^{N_e} \lambda_l \langle\lambda_l|\hat{\sigma}(t)|\lambda_l\rangle \tag{III.7}$$

$$\mathrm{Im}[\sigma_{jk}(t)] = Tr_e\left[\hat{\sigma}(t)\hat{Y}_{jk}\right] \equiv \sum_{l=1}^{N_e} \kappa_l \langle\kappa_l|\hat{\sigma}(t)|\kappa_l\rangle \ . \tag{III.8}$$

This implies that there are two distinctly different ways of calculating $\{\sigma_{jk}(t)|j \neq k\}$ via the GQME approach from either the *off-diagonal* matrix elements in terms of the $\{|j\rangle\}$ basis or the *diagonal* matrix elements in terms of the $\{|\lambda_l\rangle\}$ and $\{|\kappa_l\rangle\}$ bases. One of the goals of this chapter is to compare and contrast those two approaches.

III.3 The Generalized Quantum Master Equation

The GQME formalism provides a general framework for deriving *exact* equations of motion for observables of interest while keeping the information on the projected-out DOF to the minimum necessary to account for their effect on the observables of interest. Within this formalism, the dynamics of the projected state, $\mathcal{P}\,|\rho(t)\rangle\rangle$, for any projection superoperator $\mathcal{P}$ that satisfies idempotence ($\mathcal{P}^2 = \mathcal{P}$), is given by the Nakajima-Zwanzig equation:[1, 93–95]

$$\frac{d}{dt}\mathcal{P}\hat{\rho}(t) \;=\; -\frac{i}{\hbar}\mathcal{P}\mathcal{L}\mathcal{P}\hat{\rho}(t) - \frac{i}{\hbar}\mathcal{P}\mathcal{L}e^{-i\mathcal{Q}\mathcal{L}t/\hbar}\mathcal{Q}\hat{\rho}(0) - \frac{1}{\hbar^2}\int_0^t d\tau\mathcal{P}\mathcal{L}e^{-i\mathcal{Q}\mathcal{L}\tau/\hbar}\mathcal{Q}\mathcal{L}\mathcal{P}\hat{\rho}(t-\tau), \tag{III.9}$$

where $\mathcal{P}$ is a projection superoperator, $\mathcal{Q} = \mathcal{I} - \mathcal{P}$ is the complementary superoperator (where $\mathcal{I}$ is the identity superoperator), and $\mathcal{L} = [\hat{H}, \cdot\,]$ is the overall system Liouvillian with $\hat{H}$ the overall system Hamiltonian. Previous work focused on the Hilbert space and introduced the reduced-dimensionality GQME approach with a projection onto any combination of electronic states.[70] Here, we present the reduced-dimensionality GQME in Liouville space. The motivation for this choice arises from the existence of the superoperators in Hilbert space. Moving into Liouville space will make the superoperators operators, i.e. matrices.

In Hilbert space, the projection superoperator is defined as: [70]

$$\mathcal{P}\{\,\cdot\,\} = \sum_{a,b} \mathrm{Tr}\Big\{\left(|a\rangle\langle b| \otimes \mathbb{I}_n\right)^\dagger \cdot\Big\}\,|a\rangle\langle b| \otimes \hat{\rho}_n(0), \tag{III.10}$$

where $|a\rangle\,\langle b|$ are selected projections of electronic states, $\mathbb{I}_n$ is the identity operator in nuclear

space, and $\hat{\rho}_n(0)$ is the initial nuclear density matrix, given by $\hat{\rho}_n(0) = \mathrm{Tr}_e\{\hat{\rho}(0)\}$ with Tr_e the trace over the electronic degrees of freedom (DOF) and $\hat{\rho}(0)$ the overall initial density matrix. Note that $\mathcal{P}$ is idempotent when $\mathrm{Tr}_n\left\{\hat{\rho_{\mathrm{n}}(0)}\right\} = 1$.

In Liouville space, the projector is written as:

$$\mathcal{P}\,|\cdot\rangle\rangle = \sum_{ab\in\mathcal{P}} |ab\otimes\rho_{\mathrm{n}}(0)\rangle\rangle\,\langle\langle ab\otimes\mathbb{I}_n|\cdot\rangle\rangle. \tag{III.11}$$

From here on we use the notation $ab \in \mathcal{P}$ to represent electronic state $|ab\rangle\rangle$ in the projection subspace, and $\alpha\beta \in \mathcal{Q}$ to represent electronic state $|\alpha\beta\rangle\rangle$ in the complement subspace. Similarly, $\mathcal{P}$ is a valid projection operator when $\mathrm{Tr}_n\{\rho_{\mathrm{n}}(0)\} = \langle\langle\mathbb{I}_n^\dagger|\rho_{\mathrm{n}}(0)\rangle\rangle = \langle\langle\mathbb{I}_n|\rho_{\mathrm{n}}(0)\rangle\rangle = 1$. Denoting the total electronic DOF as N_e in the Hilbert space. Then the electronic DOF in Liouville space is then N_e^2, the projected electronic DOF as $N_e^{2,\mathcal{P}}$ and the electronic DOF that is projected out as $N_e^{2,\mathcal{Q}} = N_e^2 - N_e^{2,\mathcal{P}}$. Note here that if we express the full-dimensionality projector used in the modified GQME in Ref. 68 as:

$$\mathcal{P}^{full}\,|\cdot\rangle\rangle = \mathrm{Tr}_n\{\cdot\}\otimes\hat{\rho}_n = \sum_{m=1,n=1}^{Ne} |mn\otimes\rho_{\mathrm{n}}(0)\rangle\rangle\,\langle\langle mn\otimes\mathbb{I}_n|\cdot\rangle\rangle. \tag{III.12}$$

We can then express the projector in Eq. III.11 as:

$$\mathcal{P}\,|\cdot\rangle\rangle = \sum_{ab\in\mathcal{P}} |ab\rangle\rangle\,\langle\langle ab| \sum_{m=1,n=1}^{Ne} |mn\otimes\rho_{\mathrm{n}}(0)\rangle\rangle\,\langle\langle mn\otimes\mathbb{I}_n|\cdot\rangle\rangle = \mathcal{P}_e\mathcal{P}^{full}, \tag{III.13}$$

with $\mathcal{P}_e$ defined as $\sum_{ab\in\mathcal{P}} |ab\rangle\rangle\,\langle\langle ab|$. $\mathcal{P}_e$ is a projector following idempotent. The result of the projection $\mathcal{P}_e$ acting on a vector in the same electronic Liouville space is simply a $N_e^{2,\mathcal{P}}$ dimension sub-vector matching the selected $|ab\rangle\rangle$ in Eq. III.11. Similarly, for a matrix $\hat{A}$ in the same electronic Liouville space, $\mathcal{P}_e\hat{A}\mathcal{P}_e$ results in a $N_e^{2,\mathcal{P}}\times N_e^{2,\mathcal{P}}$ dimension sub-matrix matching the selected $|ab\rangle\rangle$.

Assuming the initial state of the overall system is a separable state:

$$|\rho(0)\rangle\rangle = |\rho_{\mathrm{n}}(0)\rangle\rangle\otimes|\sigma(0)\rangle\rangle\,. \tag{III.14}$$

Recall from the previous study on the modified GQME in Ref. 68:

$$\mathcal{P}^{full}\mathcal{L} = \mathrm{Tr}_n\left\{\mathcal{L}\hat{\rho}_n(0)\right\} \equiv \langle\mathcal{L}\rangle_{\mathrm{n}}^0 . \tag{III.15}$$

With the projection superoperator expressed as Eq. (III.13) and recalling $\mathcal{P}_e,\ \mathcal{P},\ \mathcal{Q}$ are all idempotent, the GQME in Liouville space can be rewritten as:

$$\begin{aligned}\frac{d}{dt}\left|\sigma_{\mathcal{P}}(t)\right\rangle\rangle \otimes \left|\rho_{\mathrm{n}}(0)\right\rangle\rangle = &-\frac{i}{\hbar}\left\langle\mathcal{L}_{\mathcal{P}}\right\rangle_{\mathrm{n}}^0\left|\sigma_{\mathcal{P}}(t)\right\rangle\rangle \otimes \left|\rho_{\mathrm{n}}(0)\right\rangle\rangle - \mathcal{I}_{\mathcal{P}\mathcal{Q}}(t)\left|\sigma_{\mathcal{Q}}(0)\right\rangle\rangle \otimes \left|\rho_{\mathrm{n}}(0)\right\rangle\rangle \\ &- \int_0^t d\tau \mathcal{K}_{\mathcal{P}}(\tau)\left|\sigma_{\mathcal{P}}(t-\tau)\right\rangle\rangle \otimes \left|\rho_{\mathrm{n}}(0)\right\rangle\rangle , \end{aligned} \tag{III.16}$$

$$\frac{d}{dt}\left|\sigma_{\mathcal{P}}(t)\right\rangle\rangle = -\frac{i}{\hbar}\left\langle\mathcal{L}_{\mathcal{P}}\right\rangle_{\mathrm{n}}^0\left|\sigma_{\mathcal{P}}(t)\right\rangle\rangle - \mathcal{I}_{\mathcal{P}\mathcal{Q}}(t)\left|\sigma_{\mathcal{Q}}(0)\right\rangle\rangle - \int_0^t d\tau \mathcal{K}_{\mathcal{P}}(\tau)\left|\sigma_{\mathcal{P}}(t-\tau)\right\rangle\rangle , \tag{III.17}$$

$$\text{with} \qquad \left|\sigma_{\mathcal{P}}(t)\right\rangle\rangle \coloneqq \mathcal{P}_e\left|\sigma(t)\right\rangle\rangle , \tag{III.18}$$

$$\left\langle\mathcal{L}_{\mathcal{P}}\right\rangle_{\mathrm{n}}^0 = \mathcal{P}_e\left\langle\mathcal{L}\right\rangle_{\mathrm{n}}^0\mathcal{P}_e, \tag{III.19}$$

$$\mathcal{I}_{\mathcal{P}\mathcal{Q}}(t) \coloneqq \frac{i}{\hbar}\mathcal{P}\mathcal{L}e^{-i\mathcal{Q}\mathcal{L}t/\hbar}\mathcal{Q}, \tag{III.20}$$

$$\left|\sigma_{\mathcal{Q}}(0)\right\rangle\rangle \coloneqq \left|\sigma(0)\right\rangle\rangle - \mathcal{P}_e\left|\sigma(0)\right\rangle\rangle , \tag{III.21}$$

$$\mathcal{K}_{\mathcal{P}}(\tau) \coloneqq \frac{1}{\hbar^2}\mathcal{P}\mathcal{L}e^{-i\mathcal{Q}\mathcal{L}\tau/\hbar}\mathcal{Q}\mathcal{L}\mathcal{P}. \tag{III.22}$$

This is derived by plugging in Eq. (III.13) and ultilizing the fact that:

$$\mathcal{P}\left|\rho(t)\right\rangle\rangle = \mathcal{P}_e\mathcal{P}^{full}\left|\rho(t)\right\rangle\rangle = \mathcal{P}_e\left|\sigma(t)\right\rangle\rangle \otimes \left|\rho_n(0)\right\rangle\rangle , \tag{III.23}$$

$$\mathcal{P}\mathcal{L}\mathcal{P} = \mathcal{P}_e\mathcal{P}^{full}\mathcal{L}\mathcal{P}^{full}\mathcal{P}_e = \mathcal{P}_e\left\langle\mathcal{L}\right\rangle_{\mathrm{n}}^0\mathcal{P}_e, \tag{III.24}$$

$$\mathcal{Q}\left|\rho(0)\right\rangle\rangle = (\mathbb{I}_e \otimes \mathbb{I}_n - \mathcal{P}_e\mathcal{P}^{full})\left|\sigma(0)\right\rangle\rangle \otimes \left|\rho_{\mathrm{n}}(0)\right\rangle\rangle = (\left|\sigma(0)\right\rangle\rangle - \mathcal{P}_e\left|\sigma(0)\right\rangle\rangle) \otimes \left|\rho_{\mathrm{n}}(0)\right\rangle\rangle . \tag{III.25}$$

$\mathbb{I}_e$ represent the basis of electronic DOF, and $\mathbb{I}_n$ is the basis of nuclear DOF.

Following our prior discussion regarding the projection operator $\mathcal{P}_e$, we see that $\left|\sigma_{\mathcal{P}}(t)\right\rangle\rangle$ is simply a $N_e^{2,\mathcal{P}}$ dimension sub-vector of $\left|\sigma(t)\right\rangle\rangle$. $\left|\sigma_{\mathcal{Q}}(0)\right\rangle\rangle$ is a $N_e^{2,\mathcal{Q}}$ dimension sub-vector of $\left|\sigma(t)\right\rangle\rangle$

corresponding to $\alpha\beta$ that is projected out. $\langle \mathcal{L}_{\mathcal{P}} \rangle_{\rm n}^0$ is a $N_e^{2,\mathcal{P}} \times N_e^{2,\mathcal{P}}$ dimension sub-matrix of $\langle \mathcal{L} \rangle_{\rm n}^0$.

To calculate the memory kernel $\mathcal{K}_{\mathcal{P}}(\tau)$ and inhomogeneous term $\mathcal{I}_{\mathcal{PQ}}(t)$, we ultilize the dyson identity:

$$e^{-\frac{i}{\hbar}\mathcal{Q}\mathcal{L}t} = e^{-\frac{i}{\hbar}\mathcal{L}t} + \frac{i}{\hbar}\int_0^t d\tau e^{-\frac{i}{\hbar}\mathcal{L}(t-\tau)}\mathcal{P}\mathcal{L}e^{-\frac{i}{\hbar}\mathcal{Q}\mathcal{L}\tau}. \tag{III.26}$$

The memory kernel $\mathcal{K}_{\mathcal{P}}(\tau)$ is then:

$$\mathcal{K}_{\mathcal{P}}(\tau) = i\dot{\mathcal{F}}_{\mathcal{P}}(\tau) - \frac{1}{\hbar}\mathcal{F}_{\mathcal{P}}(\tau)\langle \mathcal{L}_{\mathcal{P}} \rangle_{\rm n}^0 + i\int_0^\tau d\tau' \mathcal{F}_{\mathcal{P}}(\tau-\tau')\mathcal{K}_{\mathcal{P}}(\tau'), \tag{III.27}$$

$$\text{with} \qquad \mathcal{F}_{\mathcal{P}}(\tau) = \mathcal{P}_e\mathcal{F}(\tau)\mathcal{P}_e, \tag{III.28}$$

$$\dot{\mathcal{F}}_{\mathcal{P}}(\tau) = \mathcal{P}_e\dot{\mathcal{F}}(\tau)\mathcal{P}_e, \tag{III.29}$$

$$\mathcal{F}(\tau) = \frac{1}{\hbar}\mathcal{P}^{full}\mathcal{L}e^{-\frac{i}{\hbar}\mathcal{L}\tau}\mathcal{P}^{full}, \tag{III.30}$$

$$\dot{\mathcal{F}}(\tau) = -\frac{1}{\hbar^2}\mathcal{P}^{full}\mathcal{L}e^{-\frac{i}{\hbar}\mathcal{L}\tau}\mathcal{L}\mathcal{P}^{full}. \tag{III.31}$$

$\dot{\mathcal{F}}$ and $\mathcal{F}$ are projection-free inputs. In Hilbert space, as previously discussed in Ref. 68:

$$\mathcal{F}(\tau) = \frac{1}{\hbar}\mathrm{Tr}_n\left\{\mathcal{L}e^{-\frac{i}{\hbar}\mathcal{L}\tau}\hat{\rho}_n(0)\right\}, \tag{III.32}$$

$$\dot{\mathcal{F}}(\tau) = -\frac{1}{\hbar^2}\mathrm{Tr}_n\left\{\mathcal{L}e^{-\frac{i}{\hbar}\mathcal{L}\tau}\mathcal{L}\hat{\rho}_n(0)\right\}. \tag{III.33}$$

Following our prior discussion regarding the projection operator $\mathcal{P}_e$, $\mathcal{F}_{\mathcal{P}}(\tau)$ and $\dot{\mathcal{F}}_{\mathcal{P}}(\tau)$ are $N_e^{2,\mathcal{P}} \times N_e^{2,\mathcal{P}}$ dimension sub-matrix of $\mathcal{F}(\tau)$ and $\dot{\mathcal{F}}(\tau)$.

The inhomogeneous term $\mathcal{I}_{\mathcal{PQ}}(t)$ is then:

$$\mathcal{I}_{\mathcal{PQ}}(t) = i\mathcal{F}_{\mathcal{PQ}}(t) + i\int_0^t d\tau \mathcal{F}_{\mathcal{P}}(t-\tau)\mathcal{I}_{\mathcal{PQ}}(\tau), \tag{III.34}$$

$$\text{with} \qquad \mathcal{F}_{\mathcal{PQ}}(t) = \mathcal{P}_e\mathcal{F}(\tau)(\mathbb{I}_e - \mathcal{P}_e). \tag{III.35}$$

Here, $\mathcal{F}_{\mathcal{PQ}}(t)$ is a $N_e^{2,\mathcal{P}} \times N_e^{2,\mathcal{Q}}$ dimension sub-matrix of $\mathcal{F}(\tau)$ and $\dot{\mathcal{F}}(\tau)$.

III.3.1 Full-Dimensionality GQME with Condon Approximation

Here, we briefly present the full-dimensionality GQME with Condon approximation as proposed in Ref. 68. For systems satisfying the Condon approximation, the memory kernel Eq. III.22 can be furtherly simplified. In Hilbert space, the kernel of the full-dimensionality GQME with Condon approximation is:

$$\mathcal{K}(\tau) = \frac{1}{\hbar^2}\mathrm{Tr}_n \left\{ \mathcal{L}_{\text{zero}} e^{-i\mathcal{Q}\mathcal{L}_{\text{zero}}\tau/\hbar} \mathcal{Q}\mathcal{L}_{\text{zero}} \hat{\rho}_n(0) \right\}, \tag{III.36}$$

with $\mathcal{L}_{\text{zero}}(\cdot) = \left[\sum_{i=1}^{N_e} \hat{H}_i \left|i\right\rangle\!\left\langle i\right|, \cdot\right]$ The corresponding Volterra equation is then:

$$\mathcal{K}(\tau) = \mathcal{F}_1(\tau) - \frac{1}{\hbar}\mathcal{F}_2(\tau) \left\langle \mathcal{L}_{\text{zero}} \right\rangle_{\text{n}}^{0} + i\int_0^\tau d\tau' \mathcal{F}_2(\tau-\tau')\mathcal{K}(\tau'), \tag{III.37}$$

$$\text{with,} \qquad \mathcal{F}_1(\tau) = \frac{1}{\hbar^2}\mathrm{Tr}_n \left\{ \mathcal{L}_{\text{zero}} e^{-\frac{i}{\hbar}\mathcal{L}\tau} \mathcal{L}_{\text{zero}} \hat{\rho}_n(0) \right\}, \tag{III.38}$$

$$\mathcal{F}_2(\tau) = \frac{1}{\hbar}\mathrm{Tr}_n \left\{ \mathcal{L}_{\text{zero}} e^{-\frac{i}{\hbar}\mathcal{L}\tau} \hat{\rho}_n(0) \right\}. \tag{III.39}$$

$\mathcal{F}_1$ and $\mathcal{F}_2$ are projection-free inputs. Detailed derivation can be found in Ref. 68.

III.3.2 Reduced-Dimensionality GQME in σ_x Representation for the Spin-Boson Model

As is discussed in Sec. III.2, for any electronic observable, we can transform GQME into the corresponding eigenbasis. The definition of populations, i.e. the diagonal terms in the reduced density operator, and the coherences, i.e. the off-diagonal terms in the reduced density operator are basis-dependent. In this subsection, we explore this option with the electronic observables $\hat{\sigma}_x$ for the spin-boson model:

$$\hat{\sigma}_x = \begin{pmatrix} 0 & 1 \\ 1 & 0 \end{pmatrix}. \tag{III.40}$$

This choice is prompted by the accuracy of QC/MH methods. As we observed in Table II.1, for the spin-boson model, $\langle\hat{\sigma}_x\rangle$ is the hardest to evaluate among all Pauli matrices. $\hat{\sigma}_x$ has two eigenvalues: $+1$ and -1. The corresponding eigenvectors are:

$$v_x^+ = \frac{1}{\sqrt{2}}\begin{pmatrix} 1 \\ 1 \end{pmatrix}, \quad v_x^- = \frac{1}{\sqrt{2}}\begin{pmatrix} 1 \\ -1 \end{pmatrix}. \tag{III.41}$$

The corresponding basis vectors in the tensor-product space can be arrived at by calculating outer products. Therefore, in Liouville space, with basis $\{|++\rangle\rangle, |+-\rangle\rangle, |-+\rangle\rangle, |--\rangle\rangle\}$ the transform matrices are:

$$U_{\sigma_x\leftarrow\sigma_z} = \frac{1}{2}\begin{pmatrix} 1 & 1 & 1 & 1 \\ 1 & -1 & 1 & -1 \\ 1 & 1 & -1 & -1 \\ 1 & -1 & -1 & 1 \end{pmatrix}. \tag{III.42}$$

We can therefore transform any superoperator A_{σ_z} or vector v_{σ_z} in Liouville space by:

$$A_{\sigma_x} = U_{\sigma_x\leftarrow\sigma_z} A_{\sigma_z} U^\dagger_{\sigma_x\leftarrow\sigma_z},\ v_{\sigma_x} = U_{\sigma_x\leftarrow\sigma_z} v_{\sigma_z}. \tag{III.43}$$

To implement GQME in the $\hat{\sigma}_x$ representation, we utilize the above equations to transform the $\mathcal{F}$, $\dot{\mathcal{F}}$, $\langle\mathcal{L}\rangle^0_{\mathrm{n}}$, $|\sigma\rangle\rangle$ calculated in the $\hat{\sigma}_z$ representation into the $\hat{\sigma}_x$ representation.

We note that because the transformation is unitary, the inner product is preserved. Therefore the transformation itself does not introduce any changes in the resulting simulation of the reduced electronic density matrix. However, for the reduced-dimensionality GQME, transforming into the observable eigenspace allows us to define different projections $\mathcal{P}_e$. With reduced-dimensionality GQME, the transformation of representation might introduce change to the resulting simulation of the reduced electronic density matrix.

III.4 Spin-Boson Model: Application Walkthrough

In this section, we will use LSCI as the input method to demonstrate how to apply GQME to the two-level spin-boson model described in Sec. II.4.1. The application of GQME can be described as three steps: 1) generating the projection-free inputs, 2) calculating the kernel and the inhomogeneous term, and 3) numerical integration of the GQME.

First we evaluate the projection-free inputs $\mathcal{F}, \dot{\mathcal{F}}, \mathcal{F}_1$ and $\mathcal{F}_2$ with the QC/MH approach. Note here that the elements of the projection-free inputs defined in Eq. (III.30), Eq. (III.31), Eq. (III.38) and Eq. (III.39) can be expressed as the following.

$$\begin{aligned}\mathcal{F}_{abcd}(\tau) &= \frac{1}{\hbar}\mathrm{Tr}_n\left\{|b\rangle\langle a|\,\mathcal{L}e^{-\frac{i}{\hbar}\mathcal{L}\tau}\hat{\rho}_n(0)\,|c\rangle\langle d|\right\} = \frac{1}{\hbar}\mathrm{Tr}_n\left\{\hat{\rho}_n(0)\,|c\rangle\langle d|\,e^{\frac{i}{\hbar}\hat{H}\tau}\,|b\rangle\langle a|\,\mathcal{L}e^{-\frac{i}{\hbar}\hat{H}\tau}\right\} \\ &= \frac{1}{\hbar}\mathrm{Tr}_n\left\{\hat{\rho}_n(0)\,|c\rangle\langle d|\,e^{\frac{i}{\hbar}\hat{H}\tau}\left[|b\rangle\langle a|\,,\hat{H}\right]e^{-\frac{i}{\hbar}\hat{H}\tau}\right\}. \qquad \text{(III.44)}\end{aligned}$$

$$\begin{aligned}\dot{\mathcal{F}}_{abcd}(\tau) &= -\frac{1}{\hbar^2}\mathrm{Tr}_n\left\{|b\rangle\langle a|\,\mathcal{L}e^{-\frac{i}{\hbar}\mathcal{L}\tau}\mathcal{L}\hat{\rho}_n(0)\,|c\rangle\langle d|\right\} = -\frac{1}{\hbar^2}\mathrm{Tr}_n\left\{\mathcal{L}\hat{\rho}_n(0)\,|c\rangle\langle d|\,e^{\frac{i}{\hbar}\hat{H}\tau}\,|b\rangle\langle a|\,\mathcal{L}e^{-\frac{i}{\hbar}\hat{H}}\right\} \\ &= -\frac{1}{\hbar^2}\mathrm{Tr}_n\left\{\left[\hat{H},\hat{\rho}_n(0)\,|c\rangle\langle d|\right]e^{\frac{i}{\hbar}\hat{H}\tau}\left[|b\rangle\langle a|\,,\hat{H}\right]e^{-\frac{i}{\hbar}\hat{H}}\right\}. \qquad \text{(III.45)}\end{aligned}$$

$$\begin{aligned}\mathcal{F}_{2,abcd}(\tau) &= \frac{1}{\hbar}\mathrm{Tr}_n\left\{|b\rangle\langle a|\,\mathcal{L}_{\text{zero}}e^{-\frac{i}{\hbar}\mathcal{L}\tau}\hat{\rho}_n(0)\,|c\rangle\langle d|\right\} = \frac{1}{\hbar}\mathrm{Tr}_n\left\{\hat{\rho}_n(0)\,|c\rangle\langle d|\,e^{\frac{i}{\hbar}\hat{H}\tau}\,|b\rangle\langle a|\,\mathcal{L}_{\text{zero}}e^{-\frac{i}{\hbar}\hat{H}\tau}\right\} \\ &= \frac{1}{\hbar}\mathrm{Tr}_n\left\{\hat{\rho}_n(0)\,|c\rangle\langle d|\,e^{\frac{i}{\hbar}\hat{H}\tau}\left[|b\rangle\langle a|\,,\hat{H}_{\text{zero}}\right]e^{-\frac{i}{\hbar}\hat{H}\tau}\right\}. \qquad \text{(III.46)}\end{aligned}$$

$$\begin{aligned}\mathcal{F}_{1,abcd}(\tau) &= \frac{1}{\hbar^2}\mathrm{Tr}_n\left\{|b\rangle\langle a|\,\mathcal{L}_{\text{zero}}e^{-\frac{i}{\hbar}\mathcal{L}\tau}\mathcal{L}_{\text{zero}}\hat{\rho}_n(0)\,|c\rangle\langle d|\right\} = \frac{1}{\hbar^2}\mathrm{Tr}_n\left\{\mathcal{L}_{\text{zero}}\hat{\rho}_n(0)\,|c\rangle\langle d|\,e^{\frac{i}{\hbar}\hat{H}\tau}\,|b\rangle\langle a|\,\mathcal{L}_{\text{zero}}e^{-\frac{i}{\hbar}\hat{H}\tau}\right\}. \\ &= \frac{1}{\hbar^2}\mathrm{Tr}_n\left\{\left[\hat{H}_{\text{zero}},\hat{\rho}_n(0)\,|c\rangle\langle d|\right]e^{\frac{i}{\hbar}\hat{H}\tau}\left[|b\rangle\langle a|\,,\hat{H}_{\text{zero}}\right]e^{-\frac{i}{\hbar}\hat{H}\tau}\right\}. \qquad \text{(III.47)}\end{aligned}$$

Appling the LSC approximation to the correlation functions results in:

$$\begin{aligned}
&\mathrm{Tr}_n\left\{\hat{A}\left|c\right\rangle\!\left\langle d\right|e^{\frac{i}{\hbar}\hat{H}\tau}\left|b\right\rangle\!\left\langle a\right|\hat{B}e^{-\frac{i}{\hbar}\hat{H}\tau}\right\} \\
&\quad\approx\left(\frac{1}{2\pi\hbar}\right)^{N_e+N_n}\int\mathbf{dR}_0\int\mathbf{dP}_0\int\mathbf{dq}_0\int\mathbf{dp}_0[\hat{A}\hat{\rho}_n(0)]_W(\mathbf{R}_0,\mathbf{P}_0)B_W(\mathbf{R}_\tau,\mathbf{P}_\tau) \\
&\qquad\qquad\times\mathrm{Tr}\{e^{\frac{i}{\hbar}\hat{H}\tau}\left|b\right\rangle\!\left\langle a\right|e^{-\frac{i}{\hbar}\hat{H}\tau}\left|c\right\rangle\!\left\langle d\right|\}. \qquad \text{(III.48)}
\end{aligned}$$

where $\hat{A}$ and $\hat{B}$ are all nuclear operators and $\mathrm{Tr}\{e^{\frac{i}{\hbar}\hat{H}\tau}\left|b\right\rangle\!\left\langle a\right|e^{-\frac{i}{\hbar}\hat{H}}\left|c\right\rangle\!\left\langle d\right|\}$ is the ab-th element of the electronic density matrix with initial electronic state set as $\left|c\right\rangle\!\left\langle d\right|$. Here, the wigner transform of $\hat{H}_i\hat{\rho}_n(0)$ can be derived with the following equations:

$$\begin{aligned}
&\left[\hat{H}_i\hat{\rho}_n(0)\right]_W(\mathbf{R}_0,\mathbf{P}_0)=H_{i,W}(\mathbf{R}_0,\mathbf{P}_0)e^{i\hbar\hat{T}/2}\rho_{n,W}(\mathbf{R}_0,\mathbf{P}_0), \\
&\text{with}\qquad\hat{T}=\sum_\mu\left[\left(\frac{\overleftarrow{\partial}}{\partial R_\mu}\right)\left(\frac{\overrightarrow{\partial}}{\partial P_\mu}\right)-\left(\frac{\overleftarrow{\partial}}{\partial P_\mu}\right)\left(\frac{\overrightarrow{\partial}}{\partial R_\mu}\right)\right]. \qquad \text{(III.49)}
\end{aligned}$$

Once we have calculated the projection-free inputs, the next step is to calculate the kernel and the inhomogeneous term in Eq. (III.27) and Eq. (III.34). The kernel and the inhomogeneous terms can be calculated through an iterative algorithm. We first perform the numerical integration based on the trapezoidal rule and calculate the kernel and inhomogeneous term from $t = 0$ to $t = t$. Then we repeat this numerical integration with the newly generated kernel and inhomogeneous term until the deviation between two iterations falls in our pre-determined threshold. The typical choice of threshold is 10^{-10} to 10^{-13}. More detail on this algorithm can be found in Ref. 68.

Once we complete the calculation on the kernel and the inhomogeneous, we can then use them to integrate GQME to acquire the dynamics of the electronic density matrix as described in Eq. (III.17). There are multiple ways to perform numerical integration. We will lay out the general steps in the fourth-order Runge–Kutta methods here. For a differential equation in the form of

$\frac{dy}{dt} = f(y,t)$ with stepsize set as h, propagting y_n to y_{n+1} is done by:

$$y_{n+1} = y_n + \frac{1}{6}h(k_1 + 2k_2 + 2k_3 + k_4), \tag{III.50}$$

$$k_1 = f(y_n, t_n), \tag{III.51}$$

$$k_2 = f(y_n + \frac{1}{2}hk_1, t_n + \frac{1}{2}h), \tag{III.52}$$

$$k_3 = f(y_n + \frac{1}{2}hk_2, t_n + \frac{1}{2}h), \tag{III.53}$$

$$k_4 = f(y_n + hk_3, t_n + h). \tag{III.54}$$

III.5 Results with Spin-Boson Model

The simulation results with GQME on the populations of the spin-boson model are extensively discussed in Ref. 68–70, 91, 92. Therefore, In this section, we will show tests of the capability of GQME, both the full-dimensionality and the reduced-dimensionality versions, in describing electronic coherences, demonstrated with the two-level spin-boson model. Here, we will use the above-mentioned QC/MH methods to generate input for different versions of GQME. Detailed evaluations of the QC/MH methods applying to multiple models, including the spin-boson model, have been presented in Ref. 85. The summary of QC/MH methods results of simulating coherences can be found in Table II.4. It has been shown in the previous section that most QC/MH methods have limited ability to provide precise descriptions of electronic coherences. Building off of these previous findings, we adopt the same two-level spin-boson model as in Sec. II.4.1 and same parameters as summarized in Table II.3. The results reported were obtained with a time step of $\Delta t = 0.005$ and by averaging over $N_{\text{traj}} = 3 \times 10^6$ trajectories for each initial state and model. The quantum-mechanically exact results were calculated via the dissipation equation of motion (DEOM) method.[23] The convergence of GQME with memory time was determined with the algorithm described in Ref. 70 with the threshold set as 5×10^{-3}.

III.5.1 Results with the Full-Dimensionality GQME

The simulation results for the spin-boson model with full-dimensionality GQME are shown in Fig. III.1. A summary of the figure is presented in Table III.1. Note that, as discussed in Ref. 68, because the two-level spin-boson model follows the Condon approximation, we apply the Condon version of the GQME here. The results obtained using the full-dimensionality GQME with the non-Condon method and the reduced-dimensionality GQME will be presented in the next subsection

Spin-boson Model	A symmetric/high T		B symmetric/low T		C asymmetric/high T		D asymmetric/low T	
Input Methods	$\langle\hat{\sigma}_x\rangle$	$\langle\hat{\sigma}_y\rangle$	$\langle\hat{\sigma}_x\rangle$	$\langle\hat{\sigma}_y\rangle$	$\langle\hat{\sigma}_x\rangle$	$\langle\hat{\sigma}_y\rangle$	$\langle\hat{\sigma}_x\rangle$	$\langle\hat{\sigma}_y\rangle$
LSCI	$\surd$	–	$\surd$	$\surd$	$\surd$	–	$\surd$	$\surd$
LSCII	$\surd$	–	$\surd$	$\surd$	$\surd$	–	$\surd$	–
MF	$\surd$	–	$\surd$	–	$\surd$	–	$\surd$	$\surd$
mLSC/$\phi^1\phi^1$	$\times$	–	$\surd$	$\surd$	–	–	$\surd$	$\surd$
mLSC/$\phi^1\phi^2$	$\times$	–	$\times$	$\surd$	–	–	$\times$	–
mLSC/$\phi^2\phi^2$	$\surd$	–	–	$\surd$	–	–	–	–

Table III.1: Summary of full-dimensionality Condon GQME results. $\surd$ indicates that full-dimensionality GQME with QC/MH-generated input provides improved simulation results compared to QC/MH methods themselves. $\times$ indicates that full-dimensionality GQME with QC/MH-generated input provides worse simulation results compared to QC/MH methods themselves. – indicates no significant improvement of simulation by applying full-dimensionality GQME.

It is worth noting here that we are mainly focusing on the observable $\hat{\sigma}_x(t)$ because most of the input methods themselves are capable to generate sufficiently accurate dynamics of $\hat{\sigma}_y(t)$. We see that using MF, LSCI, LSCII, and mLSC/$\phi^2\phi^2$ as input methods for the full-dimensionality GQME can lead to accurate simulation results for coherences, even in the cases where the input methods themselves cannot generate accurate results. We also see that full-dimensionality GQME with MF, LSCI, LSCII, and mLSC/$\phi^2\phi^2$ as inputs generate more accurate results even when those input methods themselves are generating accurate enough simulations. For using mLSC/$\phi^1\phi^1$ and mLSC/$\phi^1\phi^2$ as input methods, full-dimensionality GQME seems to either provide equivalently

non-accurate results or slightly worse results.

III.5.2 Results with Reduced-Dimensionality GQMEs in the $\hat{\sigma}_z$ representation

Here we present the PFIs $\mathcal{F}(\tau)$ and $\dot{\mathcal{F}}(\tau)$ for model D in Figs. III.2 and III.3, respectively, generated with LSCII. As illustrated in Eqs. (III.30) and (III.31), for different choices of projection operators, we simply apply the corresponding sub-matrix of the PFIs. Therefore, this set of PFIs is used consistently across different versions of projection. Here, model D is the same as model 1 in Ref. 70. We note that the choice of projection operator does not affect the PFIs $\mathcal{F}(\tau)$ and $\dot{\mathcal{F}}(\tau)$. Therefore what we present here should be the same as those presented in Ref. 70, and this is confirmed by comparison.

Our choice of projection operators are:

1. One coherence reduced-dimensionality GQME

$$\mathcal{P}\,|\cdot\rangle\rangle = \sum_{ab\in\{01\}} |ab\otimes\rho_{\mathrm{n}}(0)\rangle\rangle\,\langle\langle ab\otimes\mathbb{I}_n|\cdot\rangle\rangle. \tag{III.55}$$

2. One coherence + one population reduced-dimensionality GQME

$$\mathcal{P}\,|\cdot\rangle\rangle = \sum_{ab\in\{00,01\}} |ab\otimes\rho_{\mathrm{n}}(0)\rangle\rangle\,\langle\langle ab\otimes\mathbb{I}_n|\cdot\rangle\rangle. \tag{III.56}$$

3. One coherence + full population reduced-dimensionality GQME

$$\mathcal{P}\,|\cdot\rangle\rangle = \sum_{ab\in\{00,01,11\}} |ab\otimes\rho_{\mathrm{n}}(0)\rangle\rangle\,\langle\langle ab\otimes\mathbb{I}_n|\cdot\rangle\rangle. \tag{III.57}$$

The rationale behind these choices is based on the observable of interest here. Since we are evaluating the capability of the GQMEs to describe coherence dynamics, making projections onto subspaces that contain one or more coherences are natural choices.

In Figs. III.4 and III.5, we show the memory kernel of different reduced-dimensionality GQMEs for model D, generated using LSCII as the input method. Here, we note that because of the difference in the dimensionality of different choices of projection operators, the dimensionality of kernel elements varies.

Here, we note that since we chose the initial state to be $\hat{\rho}_n(0) \otimes |0\rangle\langle 0|$, following Eq. (III.17), we see that the only projection with a non-vanishing $\mathcal{I}_{\mathcal{PQ}}(t) \, |\sigma_{\mathcal{Q}}(0)\rangle\rangle$ is the one coherence projection shown in Eq. (III.55). Therefore, in Fig. III.6, we present the inhomogenous term $\mathcal{I}(t)$ for model D, with one coherence reduced-dimensionality GQME, generated using LSCII as the input method.

The simulation results for $\langle \hat{\sigma}_x(t) \rangle$ and $\langle \hat{\sigma}_y(t) \rangle$ with reduced-dimensionality GQME is shown in Fig. III.7 and Fig. III.8, and a summary of the figure is presented in Table III.2.

We observe that although most input methods can simulate $\langle \hat{\sigma}_y(t) \rangle$ quite accurately, using reduced-dimensionality GQME can still improve the result. For $\langle \hat{\sigma}_x(t) \rangle$, we observed reduced-dimensionality GQME with projection onto subspace containing only one coherence state or only one coherence state and one population state do not provide good improvement compared to the input methods. But projecting onto a subspace of one coherence state and all the population states can provide good improvement and even accurate results. This might stem from the discovery made in Ref. 70 that a trace equal to 1 is only preserved when all population elements are included in the projection.

III.5.3 Results with Reduced-Dimensionality GQME in the $\hat{\sigma}_x$ representation

As we discussed in Sec. III.3.2, we transformed the PFIs $\mathcal{F}(\tau)$ and $\dot{\mathcal{F}}(\tau)$ acquired in the above section to the $\hat{\sigma}_x$ representation, then perform the reduced-dimensionality GQME. In the eigenspace of $\hat{\sigma}_x$, the observable $\hat{\sigma}_x$ is given by:

$$\sigma_{++} - \sigma_{--} \tag{III.58}$$

Spin-boson Model	Selection of ab in $\mathcal{P}$ presented	A: high T symmetric		B: low T symmetric		C: high T asymmetric		D: low T asymmetric	
Input Methods	as in Eq. III.11	$\langle\hat{\sigma}_x\rangle$	$\langle\hat{\sigma}_y\rangle$	$\langle\hat{\sigma}_x\rangle$	$\langle\hat{\sigma}_y\rangle$	$\langle\hat{\sigma}_x\rangle$	$\langle\hat{\sigma}_y\rangle$	$\langle\hat{\sigma}_x\rangle$	$\langle\hat{\sigma}_y\rangle$
LSCI	$\{01\}$	$\surd$	–	$\times$	/	–	–	–	/
	$\{00,01\}$	$\surd$	–	/	/	/	–	/	/
	$\{00,01,11\}$	$\surd$	–	–	/	$\surd$	–	$\surd$	$\surd$
LSCII	$\{01\}$	–	–	–	–	–	–	–	–
	$\{00,01\}$	/	–	/	–	/	–	/	–
	$\{00,01,11\}$	$\surd$	–	$\surd$	–	$\surd$	–	$\surd$	–
mLSC/$\phi^1\phi^1$	$\{01\}$	–	–	/	/	–	–	–	/
	$\{00,01\}$	/	–	/	/	–	–	$\times$	/
	$\{00,01,11\}$	$\surd$	–	/	$\surd$	–	–	$\surd$	/

Table III.2: Summary of reduced-dimensionality GQME in $\hat{\sigma}_z$ representation results. $\surd$ indicates that reduced-dimensionality GQME with QC/MH-generated input provide improved simulation results comparing to QC/MH methods themselves. $\times$ indicates that reduced-dimensionality GQME with QC/MH-generated input provide worse simulation results comparing to QC/MH methods themselves. – indicates no significant improvement of simluation by reduced-dimensionality GQME. / indicates an improvement, but not at the same level of exact result.

The initial state of the spin-boson model Eq. (II.32) in the $\hat{\sigma}_x$ representation is:

$$\hat{\rho}(0) = \hat{\rho}_n(0) \otimes \sum_{i,j=1}^{Ne} \frac{1}{2} |i\rangle\langle j| \tag{III.59}$$

The transformation into the $\hat{\sigma}_x$ representation will allow us to then choose the projector to contain only diagonal electronic states (i.e. population-only as in Ref. 70).

Our choice of projection operators are:

1. Population-only reduced-dimensionality GQME

$$\mathcal{P} |\cdot\rangle\rangle = \sum_{ab\in\{++,--\}} |ab \otimes \rho_{\mathrm{n}}(0)\rangle\rangle \langle\langle ab \otimes \mathbb{I}_n| \cdot\rangle\rangle. \tag{III.60}$$

2. Scalar reduced-dimensionality GQME

$$\mathcal{P} |\cdot\rangle\rangle = \sum_{ab\in\{++\}} |ab \otimes \rho_{\mathrm{n}}(0)\rangle\rangle \langle\langle ab \otimes \mathbb{I}_n| \cdot\rangle\rangle, \tag{III.61}$$

$$\mathcal{P} |\cdot\rangle\rangle = \sum_{ab\in\{--\}} |ab \otimes \rho_{\mathrm{n}}(0)\rangle\rangle \langle\langle ab \otimes \mathbb{I}_n| \cdot\rangle\rangle. \tag{III.62}$$

In Figs. III.9 and III.10, we show the memory kernel of different reduced-dimensionality GQMEs for model D, generated using LSCII as the input method. Here, we note that because of the difference in the dimensionality of different choices of projection operators, the dimensionality of kernel elements varies.

In the $\hat{\sigma}_x$ representation, due to the initial density matrix in Eq. (III.60), all terms in $\mathcal{I}(t)$ contribute to the GQME. Therefore, in Fig. III.11 and Fig. III.12, we present the inhomogeneous term $\mathcal{I}(t)$ for model D, with the three choices of projection operator, generated using LSCII as the input method.

The simulation results for $\langle\hat{\sigma}_x(t)\rangle$ with reduced-dimensionality GQME is shown in Fig. III.13, and a summary of the figure is presented in Table III.3.

We observe that the scalar GQME in $\hat{\sigma}_x$ representation does not bring significant improvement

Spin-Boson Model	Selection of ab in $\mathcal{P}$ presented as in Eq. III.11	A: high T symmetric	B: low T symmetric	C: high T asymmetric	D: low T asymmetric
Input Methods		$\langle\sigma_x\rangle$	$\langle\sigma_x\rangle$	$\langle\sigma_x\rangle$	$\langle\sigma_x\rangle$
LSCI	$\{++\}$	/	–	–	/
	$\{--\}$	/	/	/	/
	$\{++,--\}$	$\surd$	$\surd$	$\surd$	/
LSCII	$\{++\}$	/	/	/	/
	$\{--\}$	/	/	/	/
	$\{++,--\}$	$\surd$	$\surd$	$\surd$	$\surd$
mLSC/$\phi^1\phi^1$	$\{++\}$	/	–	–	–
	$\{--\}$	/	$\surd$	–	–
	$\{++,--\}$	/	$\surd$	–	–

Table III.3: Summary of reduced-dimensionality GQME in $\hat{\sigma}_x$ representation results. $\surd$ indicates that reduced-dimensionality GQME with QC/MH-generated input provides improved simulation results compared to QC/MH methods themselves. $\times$ indicates that reduced-dimensionality GQME with QC/MH-generated input provides worse simulation results compared to QC/MH methods themselves. – indicates no significant improvement of simulation by reduced-dimensionality GQME. / indicates an improvement, but not at the same level as the exact result.

compared to the QC/MH methods. This might stem from the discovery made in Ref. 70 that a trace equal to 1 is only preserved when all population elements are included in the projection. However, by applying the population-only projection, we can then acquire fairly accurate descriptions of $\hat{\sigma}_x$ for all four systems via GQME. The results generated in $\hat{\sigma}_z$ representation with one coherence + full population GQME are comparable to the results here. But in the $\hat{\sigma}_z$ representation, we need at least three electronic states to generate accurate results, in contrast to the two electronic states required here. This difference in dimensionality suggests that simulating the coherences of the spin-boson model can be performed more efficiently in the $\hat{\sigma}_x$ representation.

III.5.4 Convergence Memory Time

The convergence memory times determined by the algorithm described in Ref. 70 are summarized in Table III.4 and Table III.5. The convergence threshold needed by the algorithm is determined by approximately 1% of the scale of the dynamics. Therefore, we employ 0.001 as the threshold for model A and 0.005 for other models.

Convergence memory time for full-electronic states non-Condon GQME:

Spin-boson Model	A: high T symmetric	B: low T symmetric	C: high T asymmetric	D: low T asymmetric
Input Methods	t_{mem}	t_{mem}	t_{mem}	t_{mem}
LSCI	19.43	16.25	18.61	17.97
LSCII	19.10	14.95	14.85	17.29
MF	18.59	11.36	9.13	14.19
mLSC/$\phi^1\phi^1$	19.37	13.46	18.82	17.62
mLSC/$\phi^1\phi^2$	19.43	18.17	18.71	18.06
mLSC/$\phi^2\phi^2$	19.33	17.24	18.77	18.15

Table III.4: Summary of convergence memory time for the above mentioned system and full-dimensionality non-Condon GQME.

With the same threshold, we see that the time needed for convergence is generally the largest for the reduced-dimensionality GQMEs in the $\hat{\sigma}_z$ representation. Interestingly, the reduced-dimensionality GQMEs in the $\hat{\sigma}_x$ representation requires less time to converge compared to the full GQME. This is consistent with the trend observed for population observables that were reported in Ref. 70. We also note here that since we are applying a smaller threshold in this manuscript, the memory times are typically longer compare to what was reported in Ref. 70. For the reduced-dimensionality GQMEs, we find that it is easier for the GQME in $\hat{\sigma}_x$ representation to converge compared to that in $\hat{\sigma}_z$ representation. We also see that GQME with projection containing all the populations converge faster. This can be explained by the intrinsic constraint between the populations, which requires them to sum up to one, resulting in more stability in the dynamics.

Convergence memory time for reduced-dimentionality GQME in $\hat{\sigma}_z$ representation:

Spin-boson Model	Selection of ab in $\mathcal{P}$ presented	A: high T symmetric	B: low T symmetric	C: high T asymmetric	D: low T asymmetric
Input Methods	as in Eq. III.11	t_{mem}	t_{mem}	t_{mem}	t_{mem}
LSCI	$\{01\}$	18.91	18.61	19.39	19.53
	$\{00, 01\}$	19.28	19.80	19.59	19.77
	$\{00, 01, 11\}$	18.38	19.49	8.05	17.24
	full	19.02	16.07	5.83	10.98
LSCII	$\{01\}$	19.18	19.37	19.42	19.61
	$\{00, 01\}$	19.39	19.69	19.53	19.75
	$\{00, 01, 11\}$	19.15	19.43	7.99	18.90
	full	19.11	11.92	2.37	6.87
mLSC/$\phi^1\phi^1$	$\{01\}$	15.74	18.64	19.42	19.54
	$\{00, 01\}$	19.14	19.73	19.55	19.76
	$\{00, 01, 11\}$	19.01	19.68	8.45	17.18
	full	19.13	12.09	2.68	13.97

Convergence memory time for reduced-dimentionality GQME in $\hat{\sigma}_x$ representation:

Spin-boson Model	Selection of ab in $\mathcal{P}$ presented	A: high T symmetric	B: low T symmetric	C: high T asymmetric	D: low T asymmetric
Input Methods	as in Eq. III.11	t_{mem}	t_{mem}	t_{mem}	t_{mem}
LSCI	$\{++\}$	17.32	15.43	16.15	19.64
	$\{--\}$	16.71	10.73	11.25	19.04
	$\{++, --\}$	16.78	3.39	18.61	18.97
LSCII	$\{++\}$	14.44	17.71	14.77	19.49
	$\{--\}$	14.60	10.01	13.67	19.30
	$\{++, --\}$	13.32	3.44	18.66	18.94
mLSC/$\phi^1\phi^1$	$\{++\}$	16.89	17.44	16.20	19.58
	$\{--\}$	17.30	10.06	13.68	19.15
	$\{++, --\}$	14.80	3.35	18.68	18.93

Table III.5: Summary of convergence memory time for the above mentioned system and versions of GQME.

III.6 Concluding Remarks

In this chapter, we presented the modified approach to the generalized quantum master equation with a general form of projection operator. We have shown that the projection operator can be chosen to contain only a subset of electronic states. The derivation of the GQME in the Liouville space was presented. The path to generate the projection-free inputs with the quasi-classical mapping Hamiltonian approach was also discussed. Then we presented the general steps to perform GQME, which include 1) generating the projection-free inputs, 2) generating the kernels and the inhomogeneous terms via an iterative algorithm, and 3) propagating the GQME to acquire the electronic density matrices. We then reported the simulation results for the coherences of the two-level spin-boson model, acquired with various versions of GQME, with the projection-free inputs generated with the QC/MH methods. By comparing results generated with all variations of GQME, we found performing the reduced-dimensionality GQME in the $\hat{\sigma}_z$ representation, with the projection operator chosen to be population-only, can provide accurate descriptions of the real term of coherences and also requires the least dimension, i.e. computational resource. We also observed that the reduced-dimensionality GQME in the $\hat{\sigma}_x$ generally requires a smaller memory time compared to that in the $\hat{\sigma}_z$ representation.

It was shown that the GQME is a powerful method that can utilize different QC/MH methods to generate accurate results and expanding the application of GQME to a wider range of systems seems promising. Systems with conical intersections, for example, are one type of system of interest. The linearized vibronic model that we will discuss in the next chapter can be considered a benchmark for systems with conical intersections. Applying GQME to systems with a higher dimension would also be interesting, especially when we are equipped with the reduced-dimensionality GQME to ease the computational cost.

One future direction of the development of GQME is to expand the reduced-dimensionality approach to GQME with Condon approximation. The Condon approximation significantly reduced the terms to be calculated for the projection-free inputs, minimizing the computational cost and potential numerical errors. For now, development on the reduced-dimensionality GQME focuses on

the non-Condon GQME. Developing a reduced-dimensionality GQME with the Condon approximation can then further reduce the computational cost. This can be beneficial to large systems that follow Condon approximations.

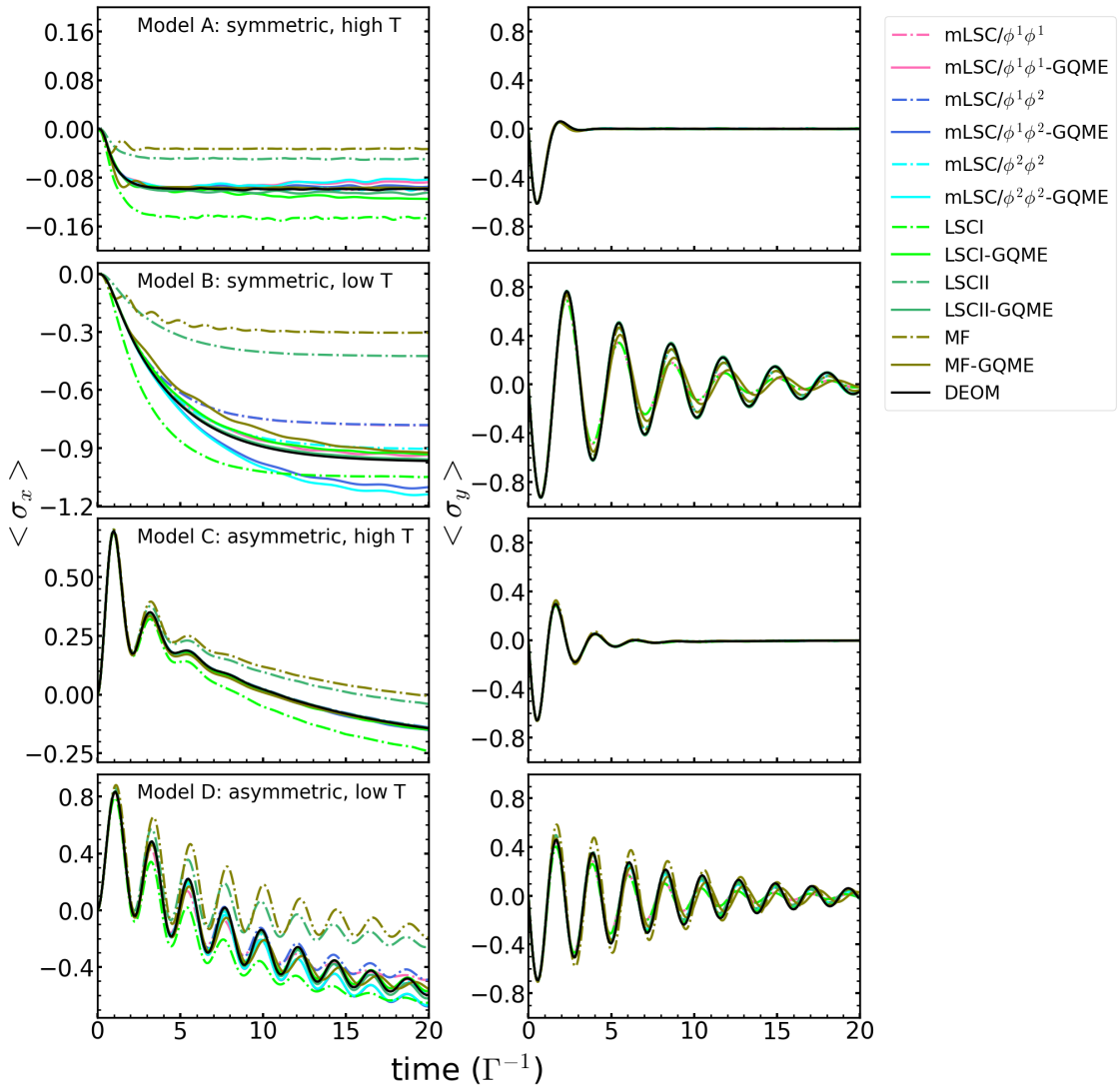

Figure III.1: Coherence dynamics of two-level spin-boson model. Model parameters are set according to Table II.3. Dash lines represent results generated directly with input methods, solid lines represent results generated with GQME. The DEOM results, represented by the black line, give the exact dynamics.

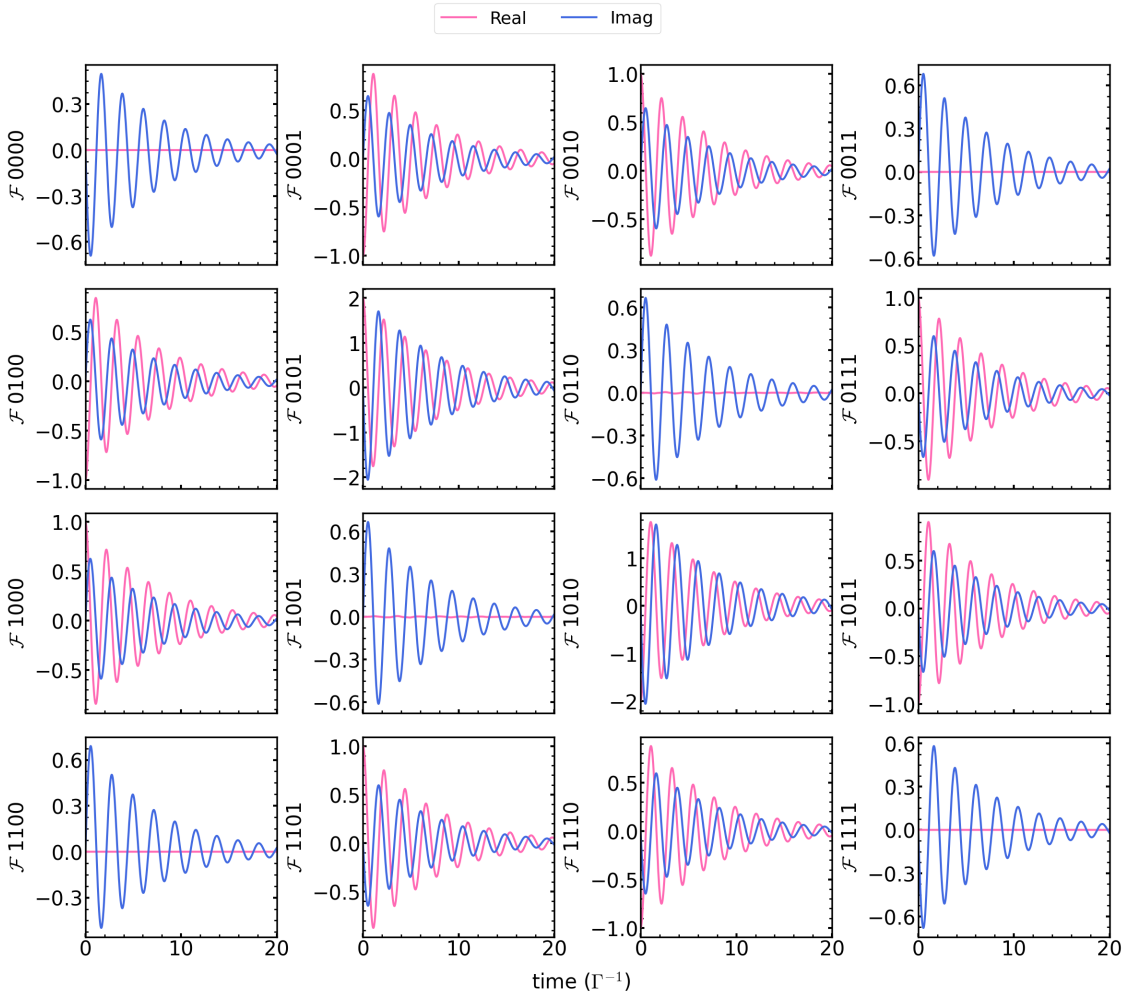

Figure III.2: Matrix elements of PFIs $\mathcal{F}$, described in Eq. III.30, for model D in Table II.3, with LSCII chosen as input method. The real part of the elements are presented in pink lines and the imaginary parts are presented in blue lines.

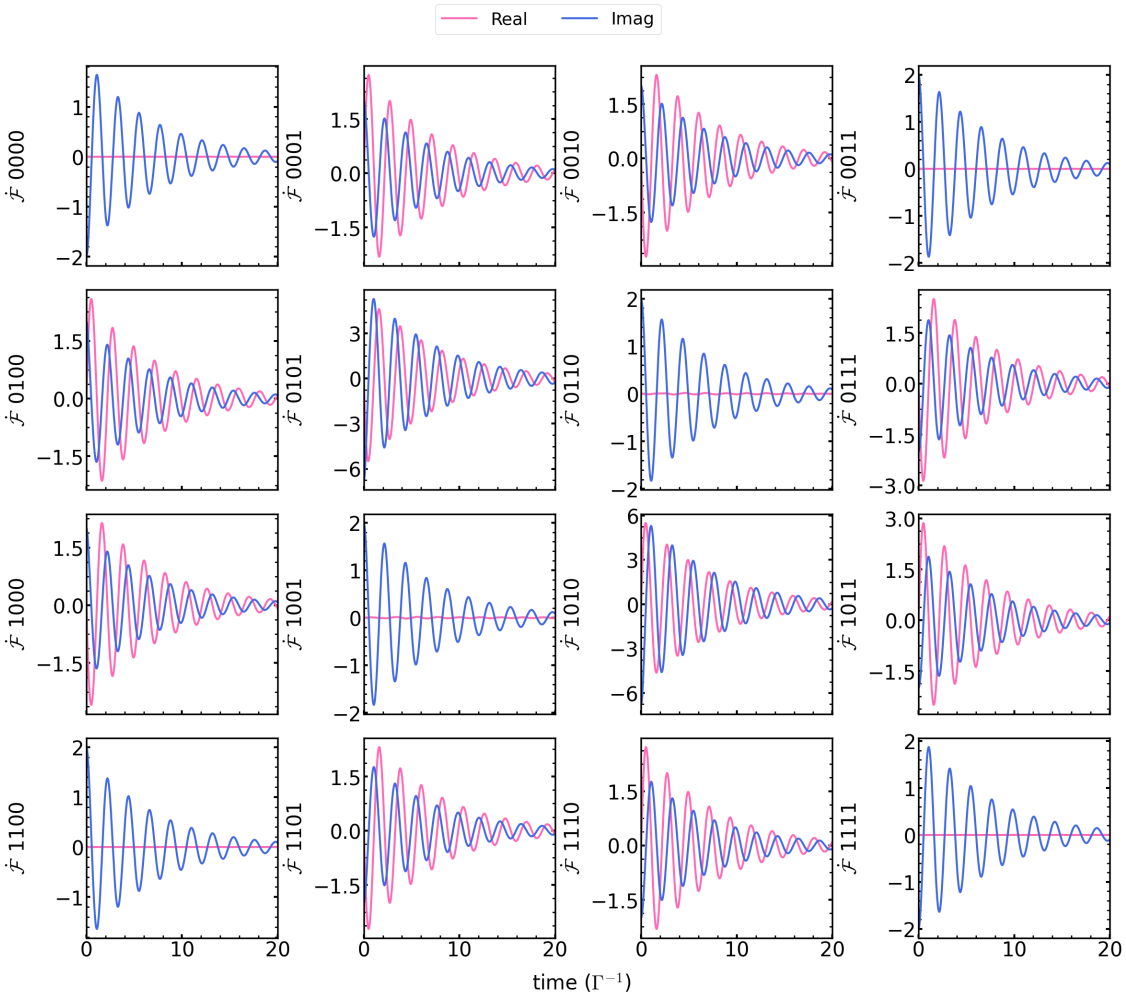

Figure III.3: Matrix elements of PFIs $\dot{\mathcal{F}}$, described in Eq. III.31, for model D in Table II.3, with LSCII chosen as input method. The real part of the elements are presented in pink lines and the imaginary parts are presented in blue lines.

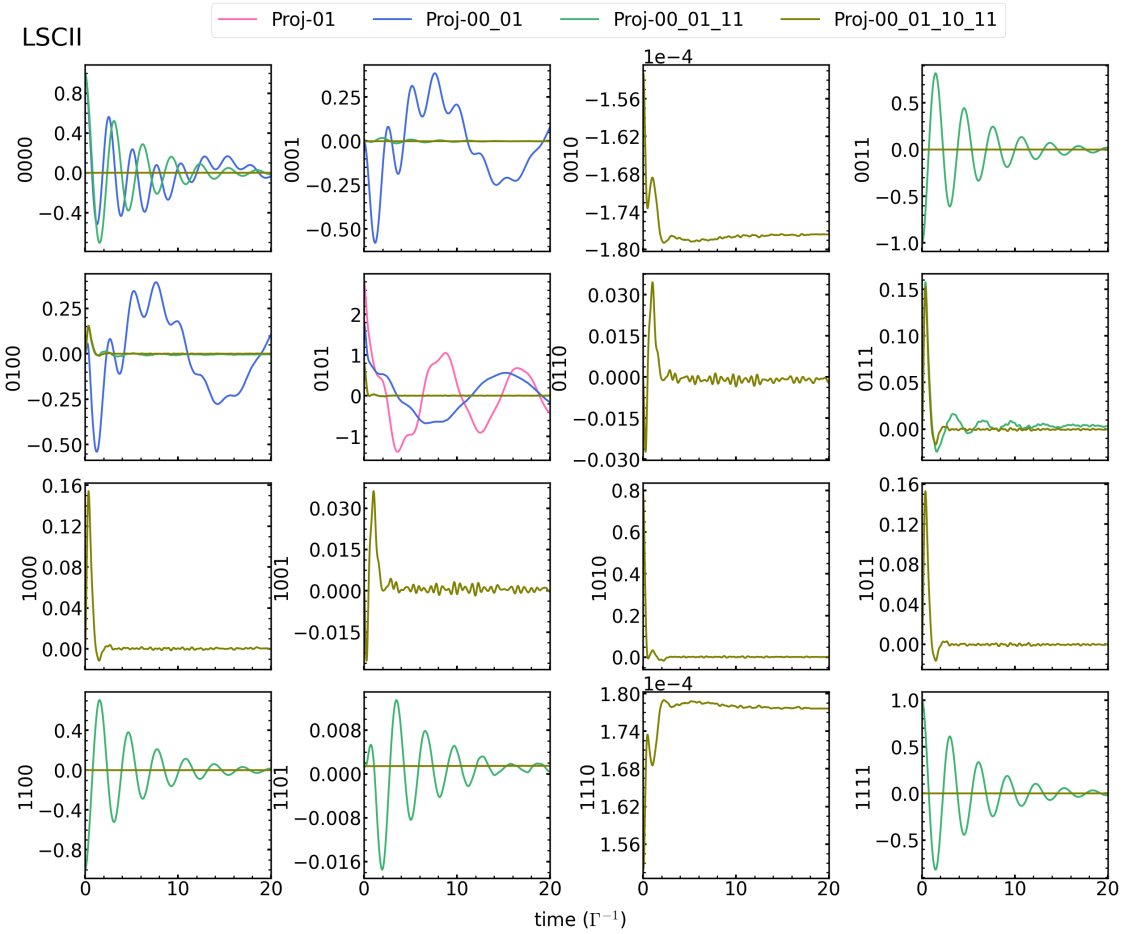

Figure III.4: Real part of matrix elements of the memory kernel $\mathcal{K}$of different choice of projection operators, for model D in Table II.3, with LSCII chosen as input method.

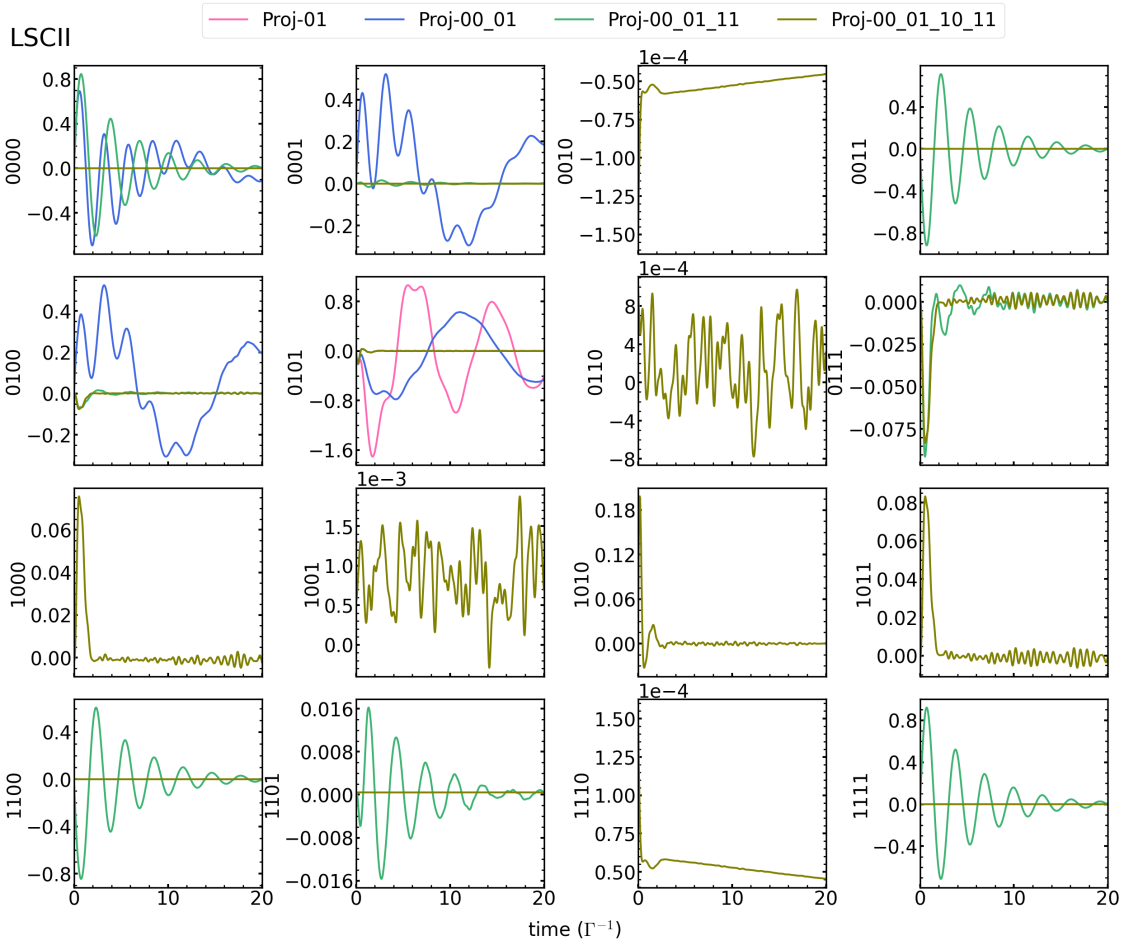

Figure III.5: Imaginary part of matrix elements of the memory kernel $\mathcal{K}$of different choice of projection operators, for model D in Table II.3, with LSCII chosen as input method.

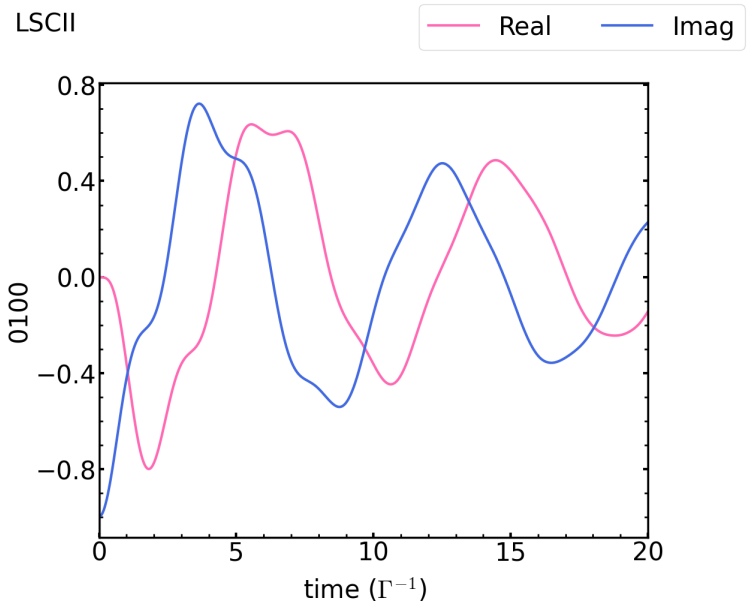

Figure III.6: Inhomogeneous term $\mathcal{I}$ for $\mathcal{P}$ chosen to include only electronic state $|0\rangle\langle 1|$, for model D in Table II.3, with LSCII chosen as input method.

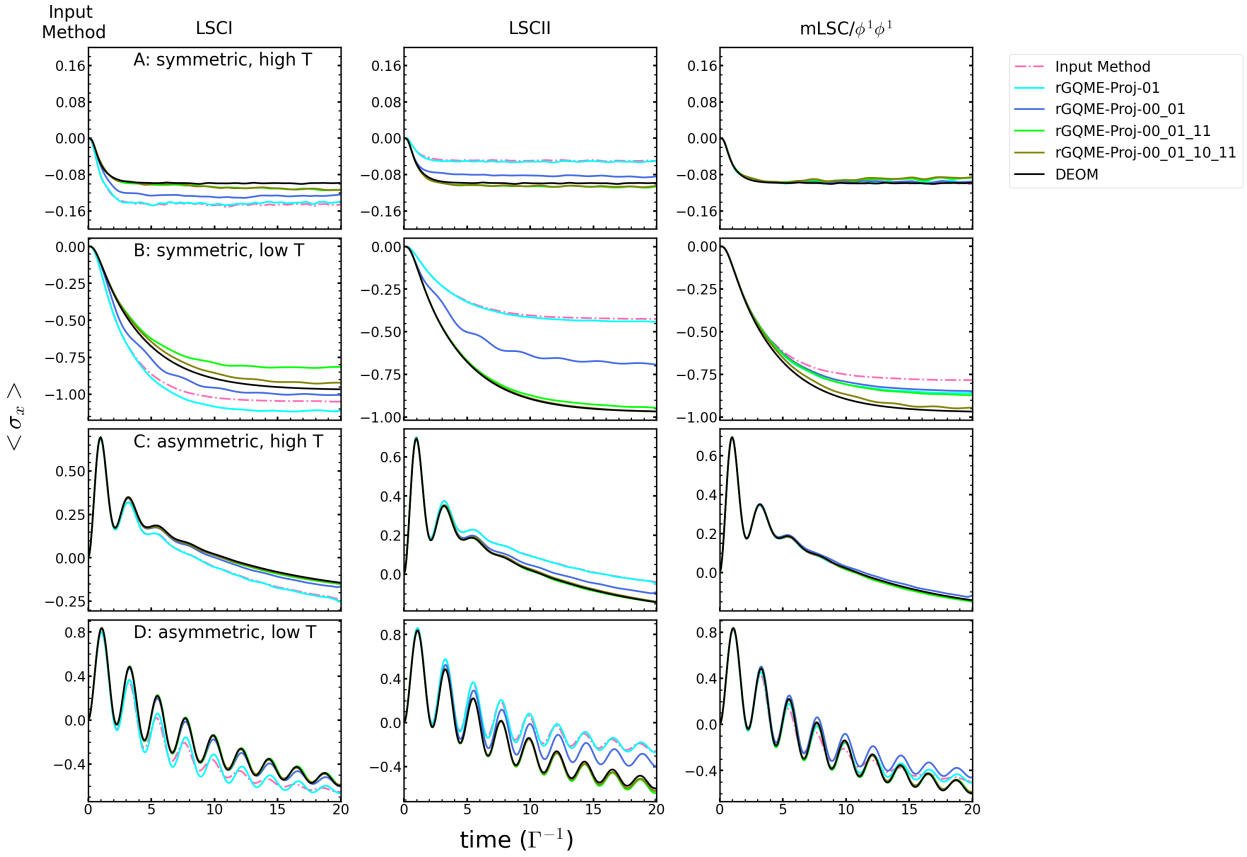

Figure III.7: $\langle \hat{\sigma}_x \rangle$ dynamics of two-level spin-boson model. Model parameters are set according to Table II.3. Dashlines represent results generated directly with input methods, solid lines represent results generated with reduced-dimensionality GQME in $\hat{\sigma}_z$ representation. The DEOM results, represented by the black line, give the exact dynamics.

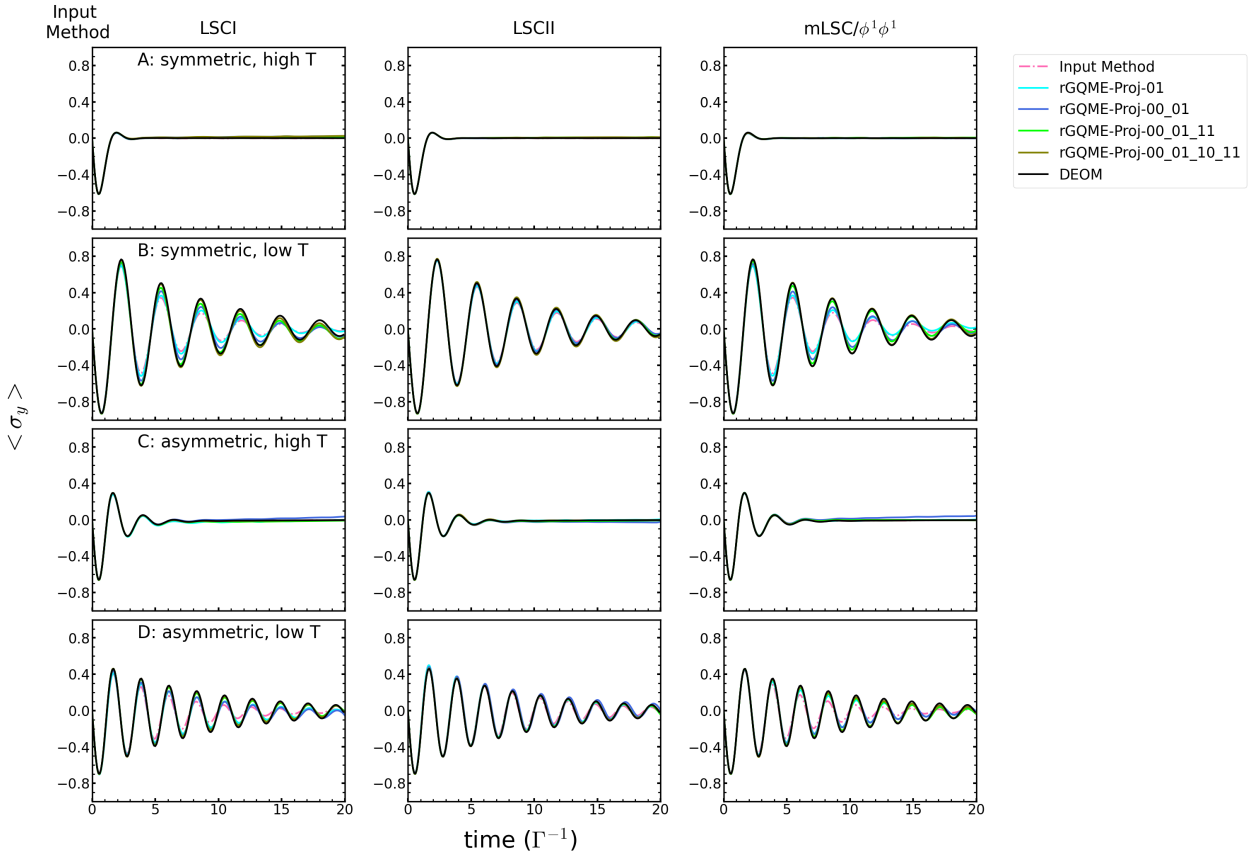

Figure III.8: $\langle \hat{\sigma}_y \rangle$ dynamics of two-level spin-boson model. Model parameters are set according to Table II.3. Dashlines represent results generated directly with input methods, solid lines represent results generated with reduced-dimensionality GQME in $\hat{\sigma}_z$ representation. The DEOM results, represented by the black line, give the exact dynamics.

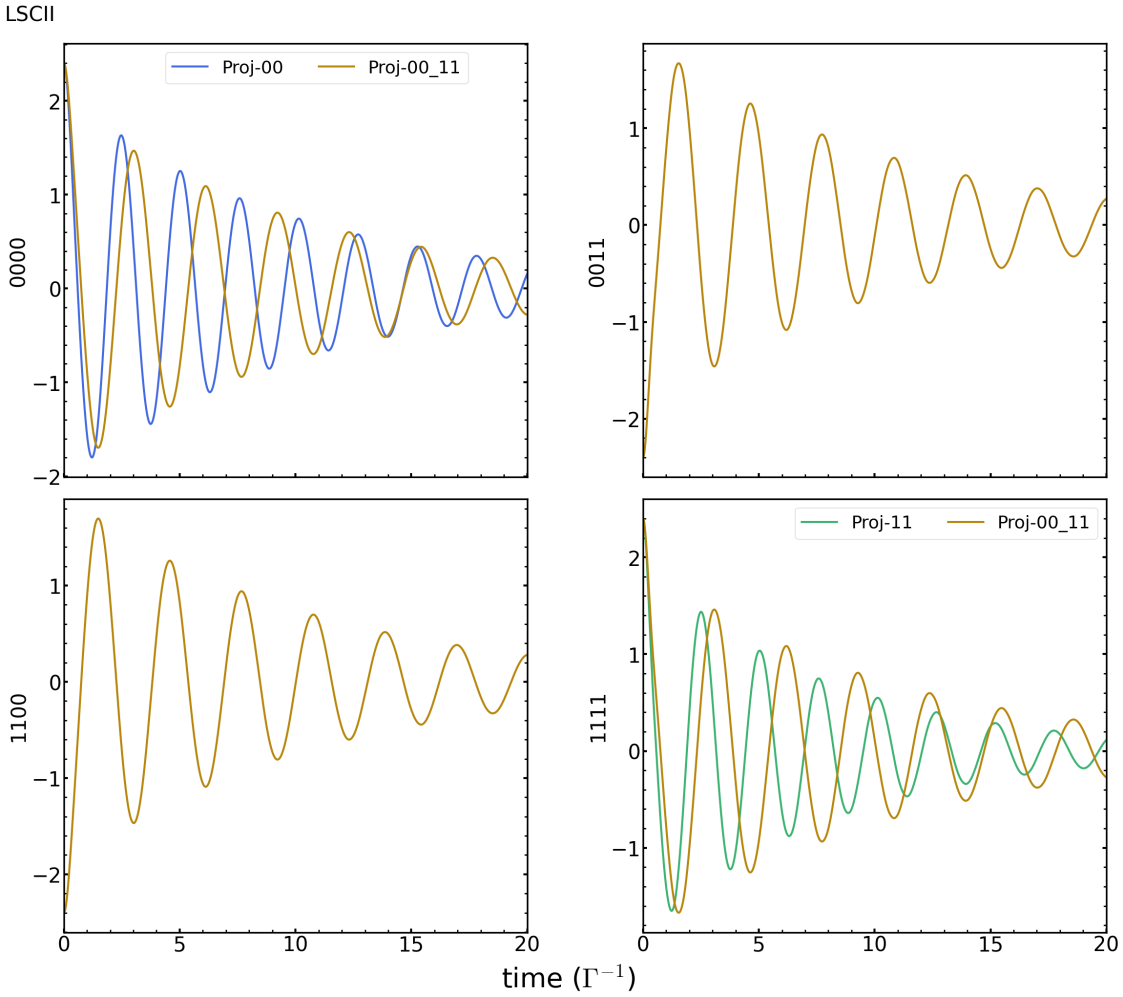

Figure III.9: Real part of matrix elements of the memory kernel $\mathcal{K}$of different choice of projection operators, for model D in Table II.3, with LSCII chosen as the input method.

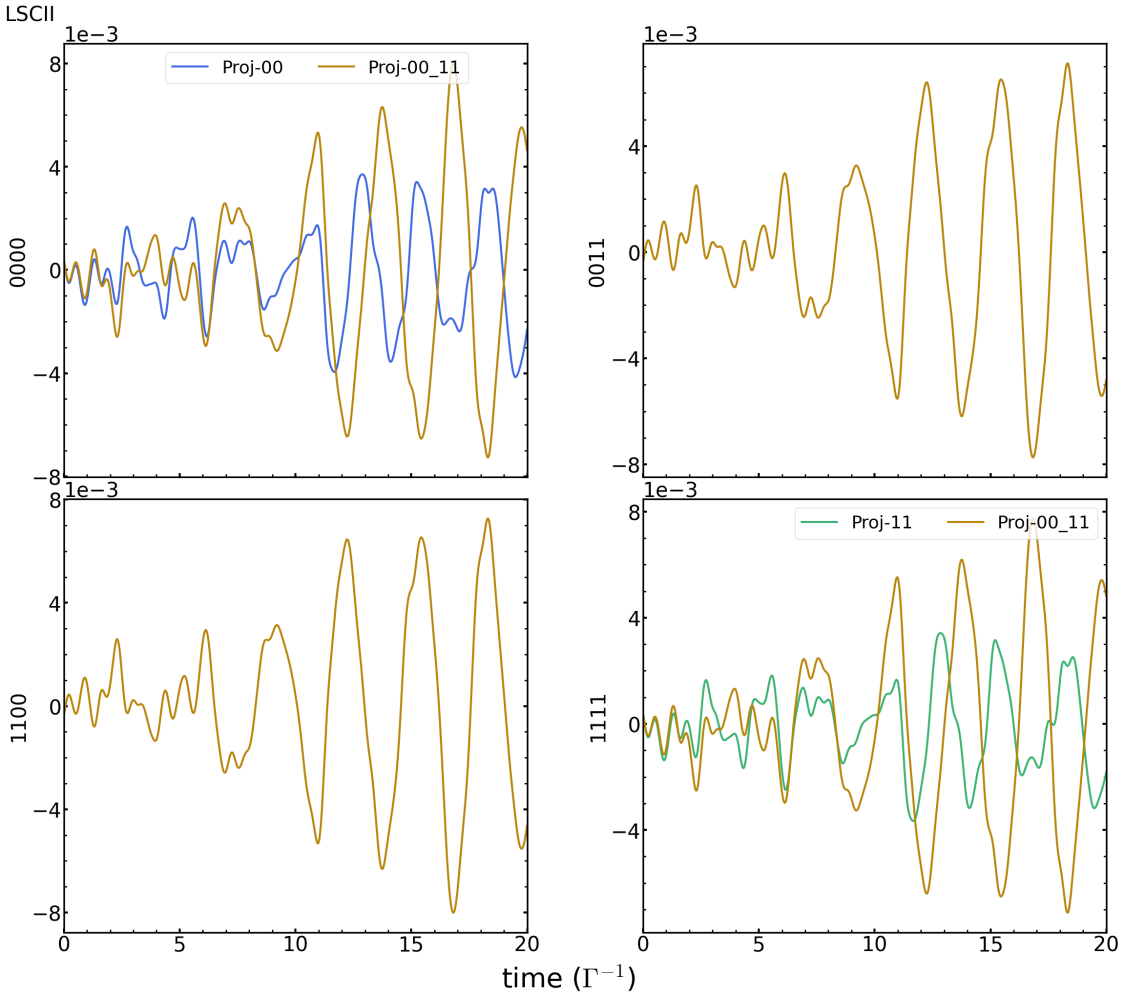

Figure III.10: Imaginary part of matrix elements of the memory kernel $\mathcal{K}$ of different choice of projection operators, for model D in Table II.3, with LSCII chosen as input method.

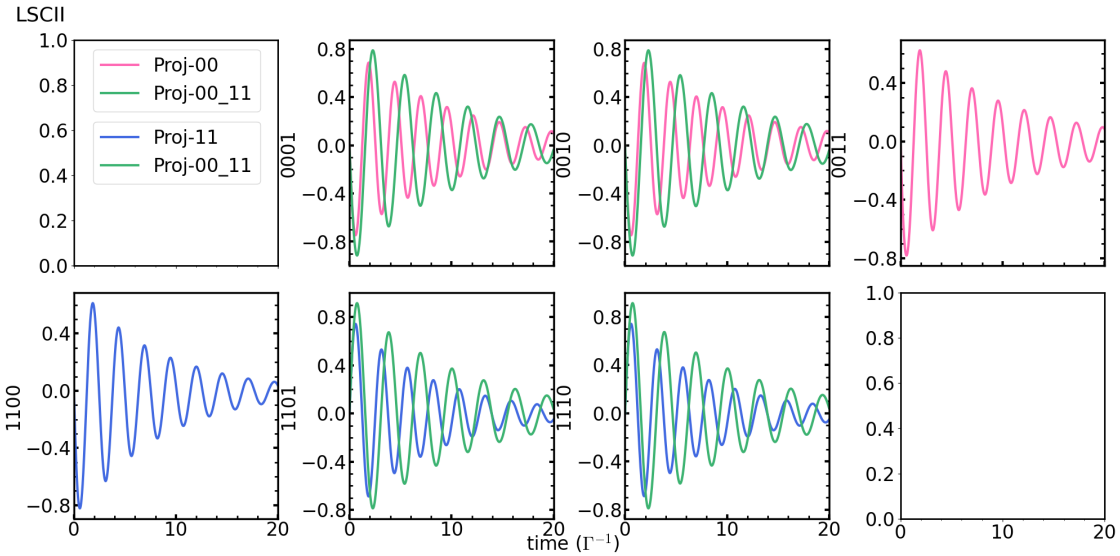

Figure III.11: Real part of the inhomogeneous term $\mathcal{I}$ for $\mathcal{P}$ chosen to include only electronic state $|0\rangle\langle 1|$, for model D in Table II.3, with LSCII chosen as input method.

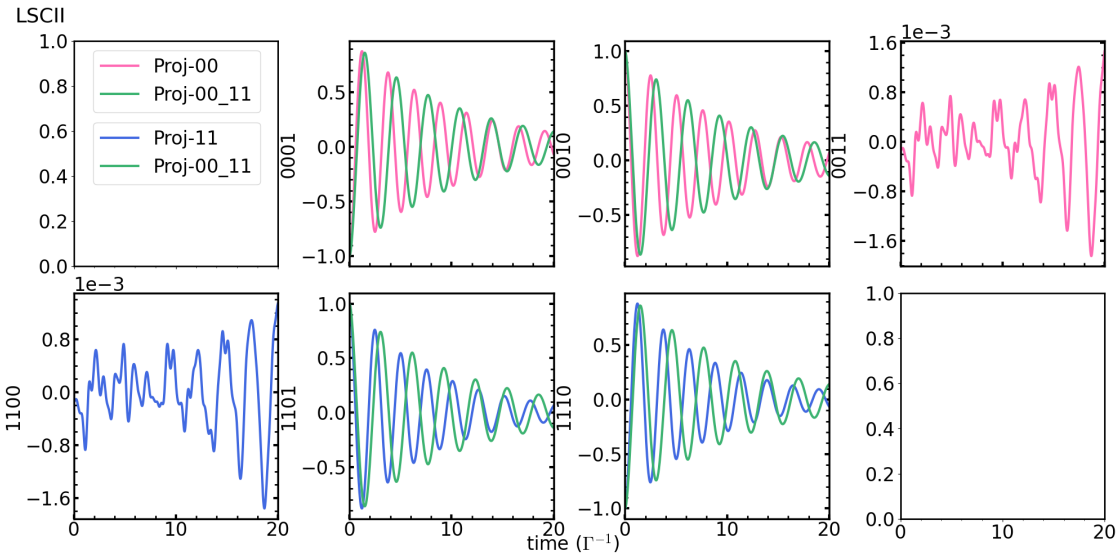

Figure III.12: Imaginary part of the inhomogeneous term $\mathcal{I}$ for $\mathcal{P}$ chosen to include only electronic state $|0\rangle\langle 1|$, for model D in Table II.3, with LSCII chosen as input method.

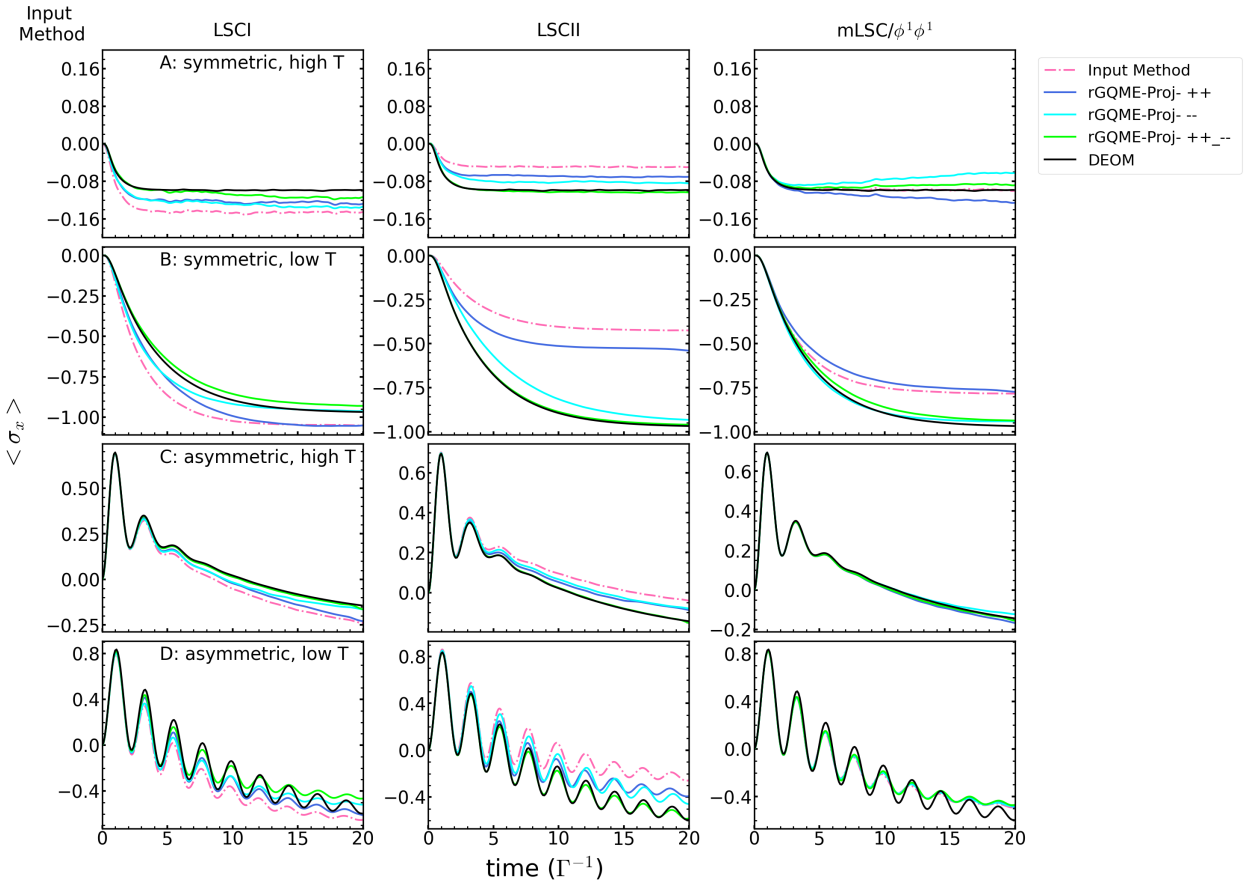

Figure III.13: Coherence dynamics of two-level spin-boson model. Model parameters are set according to Table II.3. Dash lines represent results generated directly with input methods, solid lines represent results generated with reduced-dimensionality GQME in $\hat{\sigma}_z$ representation. The DEOM results, represented by the black line, give the exact dynamics.

CHAPTER IV

Simulating The Linear Vibronic Coupling (LVC) Model

IV.1 Introduction

Conical intersections (CIs) are believed to play a central role in many photochemical processes.[28, 96–106] Being able to calculate the rates of electronic transitions through CIs in a reliable and feasible manner is therefore key for understanding such processes and developing rational design principles towards controlling them. An exact fully quantum-mechanical simulation of the dynamics of electronic transitions through CIs is limited to relatively low-dimensional molecular systems and/or simple model Hamiltonians.[36, 107–109] Thus, developing approximate methods for simulating the dynamics of electronic transitions through CIs in complex molecular systems is highly desirable.

A wide variety of approximate methods that can be used for simulating nonadiabatic dynamics in systems with CIs have been proposed, including the Ehrenfest (mean-field) method,[110] surface hopping methods,[27, 29, 33, 111–119] the mixed quantum-classical Liouville (MQCL) method,[38, 56, 120–125] and mapping Hamiltonian (MH) approaches.[36–38, 40, 42–49, 78–84, 126] These approximate methods reduce the computational cost by describing the dynamics of the nuclear degrees of freedom (DOF), and sometimes also of the electronic DOF, in terms of classical-like trajectories.

Approximate methods based on combining the MH approach with quasi-classical (QC) ap-

proximations have recently emerged as a promising approach towards modeling nonadiabatic dynamics in complex molecular systems.[43, 85] Several variations of those QC/MH methods have been found to be accurate for a variety of benchmark models, including the spin-boson model, a Frenkel bi-exciton model, Tully models, and a model for the Fenna-Matthews-Olson (FMO) light-harvesting complex.[43] Importantly, none of those models include CIs. Our goal in this paper is to extend the range of applications of QC/MH methods to systems with CIs. We do so in the context of the linear vibronic coupling (LVC) model Hamiltonian.[98, 127] The choice of the LVC model Hamiltonian as a benchmark for testing the ability of QC/MH methods to describe the dynamics of electronic transitions through CIs is motivated by the fact that it has been reported to provide a rather accurate description of CI photophysics in many polyatomic molecules and the ability to calculate quantum-mechanically exact electronic transition rates for it. The analysis was performed on LVC Hamiltonians parameterized for three polyatomic systems: fulvene, the 2,6-bis(methylene) adamanyl (BMA) radical cation, and the 2-methylene-6-isopropylidene adamantyl (MIA) radical cation. The choice of these systems was motivated by the availability of ab-initio parameter sets and the fact that these systems were used in the past as benchmarks for equilibrium Fermi's golden rule (EQ-FGR) , nonequilibrium Fermi's golden rule (NE-FGR) and LSC approximations with EQ-FGR and NE-FGR [100, 128]. It should also be noted that these systems represent the inverted region (fulvene), normal region (BMA) and in the vicinity of the transition point between those two regions (MIA).

The rest of the paper is organized as follows. The LVC model and choice of initial state are described in Sec. IV.2. The results of obtained by applying the QC/MH methods described in chapter II to the aforementioned molecular systems described by the LVC Hamiltonian and the discussion of the results are presented in Sec. IV.3. The results obtained by using QC/MH methods to generate projection-free inputs for GQME and discussion of the results are presented Sec. IV.4. Concluding remarks are given in Sec. IV.5.

IV.2 The Linear Vibronic Coupling (LVC) Model

The LVC model Hamiltonian is given by[98, 127]

$$\hat{H} = \hat{H}_1|1\rangle\langle 1| + \hat{H}_2|2\rangle\langle 2| + V_{12}(\hat{\mathbf{R}})|1\rangle\langle 2| + V_{21}(\hat{\mathbf{R}})|2\rangle\langle 1| \ , \tag{IV.1}$$

where

$$\begin{aligned} \hat{H}_j &= \frac{\hat{\mathbf{P}}^2}{2} + V_{jj}(\hat{\mathbf{R}}) \quad , \\ V_{jj}(\hat{\mathbf{R}}) &= \Delta_j + \sum_{i=1}^{N_n} \frac{1}{2}\omega_i^2 \hat{R}_i^2 + d_i^{(j)} \hat{R}_i \quad , \\ V_{12}(\hat{\mathbf{R}}) &= V_{21}(\hat{\mathbf{R}}) = \sum_{i=1}^{N_n} c_i \hat{R}_i \quad . \end{aligned} \tag{IV.2}$$

$\hat{H}_j$ represents the nuclear Hamiltonian when the system is in the electronic state $|j\rangle$ ($j = 1, 2$), $V_{12}(\hat{\mathbf{R}}) = V_{21}(\hat{\mathbf{R}})$ are the coupling terms between the two electronic states, and N_n is the number of nuclear DOF. Boldfaced variables, e.g., $\mathbf{A}$, indicate vector quantities and a hat over a variable, e.g., $\hat{B}$, indicates an operator quantity.

Within the LVC Hamiltonian, Eq. (IV.1), the nuclear DOF are given in terms of their mass-weighted coordinates, $\hat{\mathbf{R}} = (\hat{R}_1, \ldots, \hat{R}_{N_n})$, and momenta, $\hat{\mathbf{P}} = (\hat{P}_1, \ldots, \hat{P}_{N_n})$. Importantly, the diabatic potential energy surfaces (PESs), $V_j(\hat{\mathbf{R}}) = \sum_{i=1}^{N_n} \left[\frac{1}{2}\omega_i^2 \hat{R}_i^2 + d_i^{(j)} \hat{R}_i\right]$, are assumed harmonic and identical, except for a shift in equilibrium energy and geometry. The electronic coupling terms, $V_{12}(\hat{\mathbf{R}}) = V_{21}(\hat{\mathbf{R}})$, are assumed linear in the nuclear coordinates. The fact that the electronic coupling terms are explicitly $\hat{\mathbf{R}}$-dependent (i.e., in the non-Condon regime) is what makes it possible for the LVC Hamiltonian to account for CIs.

We also note for future reference that the reaction free energy and reorganization energy for the

LVC model are given by:

$$\begin{aligned}\Delta E =& \Delta_1 - \Delta_2 - \sum_{i=1}^{N_n} \frac{\left(d_i^{(1)}\right)^2 - \left(d_i^{(2)}\right)^2}{2\omega_i^2} \quad , \\ E_r =& \sum_{i=1}^{N_n} \frac{\left(d_i^{(1)} - d_i^{(2)}\right)^2}{2\omega_i^2} \quad .\end{aligned} \tag{IV.3}$$

$E_r > |\Delta E|$ and $E_r < |\Delta E|$ correspond to the Marcus normal and inverted regions, respectively.

In what follows, we assume that the initial state of the overall system is given by

$$\hat{\rho}(0) = \hat{\rho}_n(0) \otimes \hat{\sigma}(0) \quad , \tag{IV.4}$$

where $\hat{\rho}_n(0)$ and $\hat{\sigma}(0)$ are the reduced density operators that describe the initial states of the nuclear DOF and electronic DOF, respectively. The initial electronic state, $\hat{\sigma}(0)$, is assumed to be given by $|1\rangle\langle 1|$ or $|2\rangle\langle 2|$. The initial nuclear state, $\hat{\rho}_n(0)$, is assumed to be given by $\hat{\rho}_n(0) = e^{-\beta \hat{H}_2} \Big/ \mathrm{Tr}\Big\{e^{-\beta \hat{H}_2}\Big\}$ if $\hat{\sigma}(0) = |1\rangle\langle 1|$ or $\hat{\rho}_n(0) = e^{-\beta \hat{H}_1} \Big/ \mathrm{Tr}\Big\{e^{-\beta \hat{H}_1}\Big\}$ if $\hat{\sigma}(0) = |2\rangle\langle 2|$. Here, $\beta = 1/k_B T$ where T is the absolute temperature and k_B is the Boltzmann constant. It should be noted that this choice corresponds to a *nonequilibrium* initial state since the nuclear DOF are in equilibrium with respect to one electronic state while the electronic DOF are described by the other state.

The electronic density operator at a later time t is given by

$$\hat{\sigma}(t) = \sigma_{11}(t)|1\rangle\langle 1| + \sigma_{22}(t)|2\rangle\langle 2| + \sigma_{12}(t)|1\rangle\langle 2| + \sigma_{21}(t)|2\rangle\langle 1| \quad , \tag{IV.5}$$

where

$$\sigma_{jk}(t) = \mathrm{Tr}\Big\{\hat{\rho}_n(0)|\alpha\rangle\langle\alpha|e^{i\hat{H}t/\hbar}|k\rangle\langle j|e^{-i\hat{H}t/\hbar}\Big\} \quad . \tag{IV.6}$$

Here, $\hat{\rho}_n(0)|\alpha\rangle\langle\alpha|$ is the aforementioned nonequilibrium initial state. $\sigma_{jj}(t)$ corresponds to the population of the j-th electronic state and $\sigma_{jk}(t)$ (where $j \neq k$) corresponds to the electronic coherence between the j-th and the k-th electronic states. It should be noted that the coherence,

$\sigma_{10}(t)$, is relatively small ($\sim 10^{-3}$) for the systems under consideration in this paper. As a result, getting converged results for the coherence would have required a significantly larger number of trajectories, which we felt was not justified, given that population transfer dynamics is often the main quantity of interest for systems with CIs. In what follows, we will focus on the population dynamics, i.e. on the dynamics of $\sigma_{11}(t)$ and $\sigma_{22}(t)$.

As outlined in Refs. 42 and 43, the electronic population operator can also be mapped as the sum of the identity operator $\hat{1}$ and a trace zero term, giving the alternative form

$$|a\rangle\langle a| \mapsto \frac{1}{N_e}(\hat{1} + \hat{Q}_a) \quad , \tag{IV.7}$$

where

$$\hat{Q}_a = N_e \hat{M}_{aa} - \sum_{b=1}^{N_e} \hat{M}_{bb} \quad . \tag{IV.8}$$

in which $\hat{M}_{aa} \equiv |a\rangle\langle a|$, and N_e is the number of electronic DOF. Plugging Eq. (IV.7) into Eq. (IV.6) leads to the following alternative expressions for the electronic density matrix elements:

$$\begin{aligned} \sigma_{\lambda\lambda}(t) &= \frac{1}{N_e^2}\Big[N_e + C_{\hat{1}\hat{Q}_\lambda}(t) + C_{\hat{Q}_\alpha\hat{Q}_\lambda}(t)\Big] \\ \sigma_{\lambda\zeta}(t) &= \frac{1}{N_e}\Big[C_{\hat{1}\hat{M}_{\zeta\lambda}}(t) + C_{\hat{Q}_\alpha\hat{M}_{\zeta\lambda}}(t)\Big] \quad . \end{aligned} \tag{IV.9}$$

Here $\hat{M}_{\zeta\lambda} \equiv |\zeta\rangle\langle\lambda|$. The indices λ and ζ will be used consistently throughout this paper to indicate indices that are different ($\lambda \neq \zeta$). This should be contrasted to all other indices, e.g., j and k, which can be equal unless explicitly stated otherwise.

IV.3 Results with Quasi-Classical Mapping Hamiltonian Methods

In this section, we report the results of calculations performed on the LVC model for three sets of parameters that correspond to the following three gas-phase molecules: fulvene, the 2,6-

bis(methylene) adamantyl (BMA) radical cation, and the 2-methylene-6-isopropylidene adamantyl (MIA) radical cation. Those parameters were adopted from Ref. 100, where they were obtained from electronic structure calculations and the Köppel diabatization scheme.[129–131] Several key model parameters for the three molecules are shown in Table IV.1. It should be noted that fulvene corresponds to the Marcus inverted region ($|\Delta E| > E_r$), while BMA and MIA correspond to the Marcus normal region ($|\Delta E| < E_r$).

	fulvene	BMA	MIA
# modes	30	78	96
$\|\Delta E\|$ (a.u.)	0.0989	0.0004	0.0250
E_r (a.u.)	0.0887	0.0297	0.0274

Table IV.1: Number of nuclear modes, absolute value of the reaction free energy, $|\Delta E|$, and reorganization energy, E_r, for fulvene, BMA, and MIA (adopted from Ref. 100).

We compare results obtained by applying the above-mentioned seven QC/MH methods (LSCI, LSCII, mLSC/$\phi^1\phi^1$, mLSC/$\phi^1\phi^2$, mLSC/$\phi^2\phi^2$, SQC, and MF) with quantum-mechanically exact results obtained via ML-MCTDH.[108, 132] Previously reported results for the same models via NE-FGR[128] are also included for comparison. The results shown for all methods, except for LSCI, were obtained by averaging over 10^6 trajectories. LSCI results were obtained by averaging over 5×10^7 trajectories. It should be noted that the number of trajectories needed for achieving convergence in the systems under consideration is somewhat larger than that needed for achieving convergence in previously considered models.[42, 69, 85] In the case of BMA and MIA, we believe that this is caused by the smaller overall change in the population over the time scale under consideration, which requires a smaller absolute error in order to reach the same tolerance with respect to the relative error. In the case of fulvene, we believe that this is caused by the highly nonequilibrium nature of the initial state. This results in stepwise population relaxation, which implies that much of the population relaxation happens before the system is able to reach equilibrium on the donor PES.

We also note that the MCTDH results reported below are somewhat different from previously reported results obtained via the variational multi-configurational Gaussian (vMCG) wave packet

method[100] (not shown). While the origin of this discrepancy is difficult to ascertain, we speculate that they may reflect an insufficiently large Gaussian basis set used to obtain the vMCG results.

IV.3.1 Fulvene molecule

The results for fulvene are shown in Fig. IV.1. In this case, $\hat{\sigma}(0) = |2\rangle\langle 2|$ and $\hat{\rho}_n(0) = e^{-\beta\hat{H}_1} \Big/ \mathrm{Tr}\Big\{e^{-\beta\hat{H}_1}\Big\}$ (the electronic states are as labeled in Ref. 100).

We first note that while NE-FGR follows a similar trend to that of MCTDH, there are significant quantitative deviations between the two, with NE-FGR overestimating the electronic transition rate. This suggests a breakdown of the weak electronic coupling approximation underlying NE-FGR and the necessity of a post-FGR method for quantitatively predicting electronic transition rates for this molecule.

MF, which is arguably the simplest such post-FGR method, is seen to reproduce the MCTDH electronic transition rate rather well at short times, but to significantly underestimate the electronic transition rate at longer times. LSCII is seen to follow a similar behavior to MF, and is in fact slightly worse than MF at longer times. LSCI, on the other hand, is seen to reproduce the MCTDH result rather well throughout the entire time range.

Among the modified LSC methods, mLSC/$\phi^1\phi^1$ and mLSC/$\phi^1\phi^2$ are seen to reproduce the MCTDH result rather well throughout the entire time range, with mLSC/$\phi^1\phi^1$ performing slightly better than mLSC/$\phi^1\phi^2$. At the same time, mLSC/$\phi^2\phi^2$ is seen to not only significantly overestimate the electronic transition rate beyond very short times, but to also predict a negative electronic population at longer times, which is clearly non-physical.

Finally, SQC, with either square or triangular sampling windows, is seen to reproduce the MCTDH result rather well throughout the entire time range and is in fact very close to the best performing modified LSC method, mLSC/$\phi^1\phi^1$.

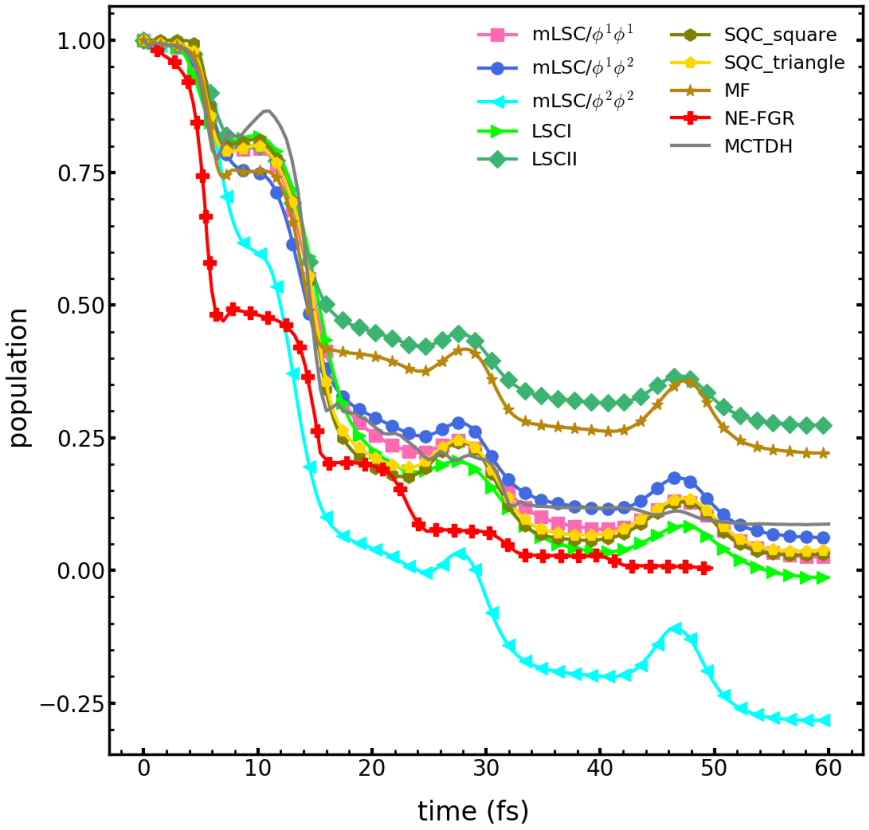

Figure IV.1: Comparison of donor population dynamics for the gas-phase fulvene molecule via different methods at T=0. The MCTDH results, represented by a black line, give the exact dynamics for fulvene with the LVC model.

IV.3.2 2,6-bis(methylene) adamantyl (BMA) radical cation

The results for BMA are shown in Fig. IV.2. In this case, $\hat{\sigma}(0) = |1\rangle\langle 1|$ and $\hat{\rho}_n(0) = e^{-\beta\hat{H}_2} \Big/ \mathrm{Tr}\left\{e^{-\beta\hat{H}_2}\right\}$ (the electronic states are as labeled in Ref. 100).

For BMA, NE-FGR reproduces the MCTDH result rather well, implying that the weak electronic coupling approximation underlying NE-FGR is valid and, given its relative simplicity, may in fact be the method of choice for this molecule.

At the same time, MF is seen to deviate significantly from the MCTDH result and to actually overestimate the electronic transition rate. LSCII is seen to follow a similar behavior to MF and is in fact somewhat worse than MF at longer times. In contrast, and similarly to fulvene, LSCI is seen to reproduce the MCTDH result rather well throughout the entire time range.

Among the modified LSC methods, only mLSC/$\phi^1\phi^1$ is seen to reproduce the MCTDH result rather well throughout the entire time range, while mLSC/$\phi^1\phi^2$ and mLSC/$\phi^2\phi^2$ are seen to significantly overestimate the MCTDH electronic transition rate. In fact, the quality of the mLSC/$\phi^1\phi^1$ result is seen to be comparable to that of LSCI, while that of the mLSC/$\phi^1\phi^2$ and mLSC/$\phi^2\phi^2$ is comparable to that of LSCII.

Finally, the SQC result for BMA is seen to be of comparable quality to that of MF and is therefore relatively inaccurate. Furthermore, significant deviations are observed between SQC results obtained with square or triangular sampling windows.

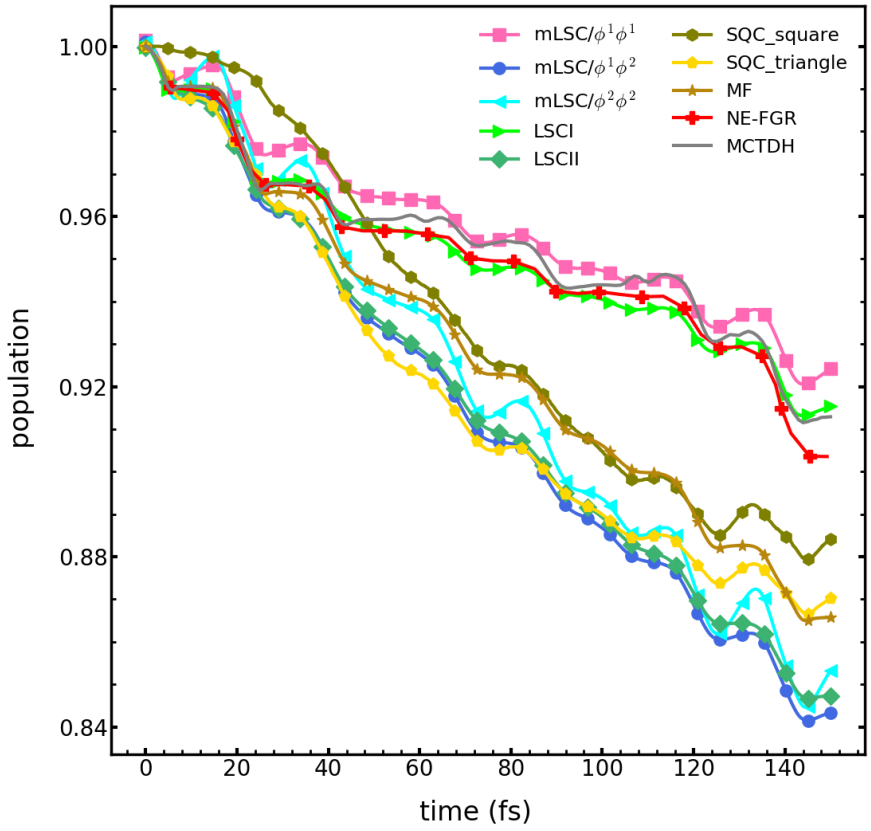

Figure IV.2: Comparison of donor population dynamics for the gas-phase BMA radical cation via different methods at T=0. The MCTDH results, represented by a black line, give the exact dynamics for BMA with the LVC model.

IV.3.3 2-methylene-6-isopropylidene adamantyl (MIA) radical cation

The results for BMA are shown in Fig. IV.3. In this case, $\hat{\sigma}(0) = |1\rangle\langle 1|$ and $\hat{\rho}_n(0) = e^{-\beta\hat{H}_2} \Big/ \mathrm{Tr}\Big\{e^{-\beta\hat{H}_2}\Big\}$ (the electronic states are as labeled in Ref. 100).

NE-FGR is seen to somewhat overestimate the electronic transition rate in MIA, which suggests a breakdown of the weak electronic coupling approximation, although to a lesser extent than in the case of fulvene.

Interestingly, the MF result is in excellent agreement with the MCTDH result for this molecule, which stands in sharp contrast to the poor performance of MF in fulvene and BMA. Also in contrast to fulvene and BMA, LSCI and LSCII yield rather similar results in this case, which are in reasonable agreement with MCTDH, but clearly not as accurate as MF.

Among the modified LSC methods, mLSC/$\phi^1\phi^1$, and mLSC/$\phi^1\phi^2$ are seen to reproduce the MCTDH result rather well throughout the entire time range under consideration, with mLSC/$\phi^1\phi^2$ yielding similar accuracy to MF and being somewhat more accurate than mLSC/$\phi^1\phi^1$. At the same time, and similarly to fulvene and BMA, mLSC/$\phi^2\phi^2$ is seen to significantly overestimate the electronic transition rate, with the deviation increasing with increasing time.

Finally, while the SQC results are seen to agree reasonably well with the MCTDH result, using triangular sampling windows clearly yields a more accurate transition rate compared to using square windows. Furthermore, the quality of the results obtained via SQC with triangular sampling windows is seen to be comparable to that of MF and mLSC/$\phi^1\phi^2$.

For the sake of comparing the performance of the different methods over the three systems they were applied to, we classify them as *accurate* ($\surd$) and *inaccurate* ($\times$) based on their ability to reproduce the MCTDH results over the time range under consideration. A summary of the performance of the different methods based on this classification is give in Table IV.2. It should be noted that classifying the methods as accurate and inaccurate is somewhat subjective and obviously cannot account for more nuanced behavior (e.g., methods that are accurate at short time but whose

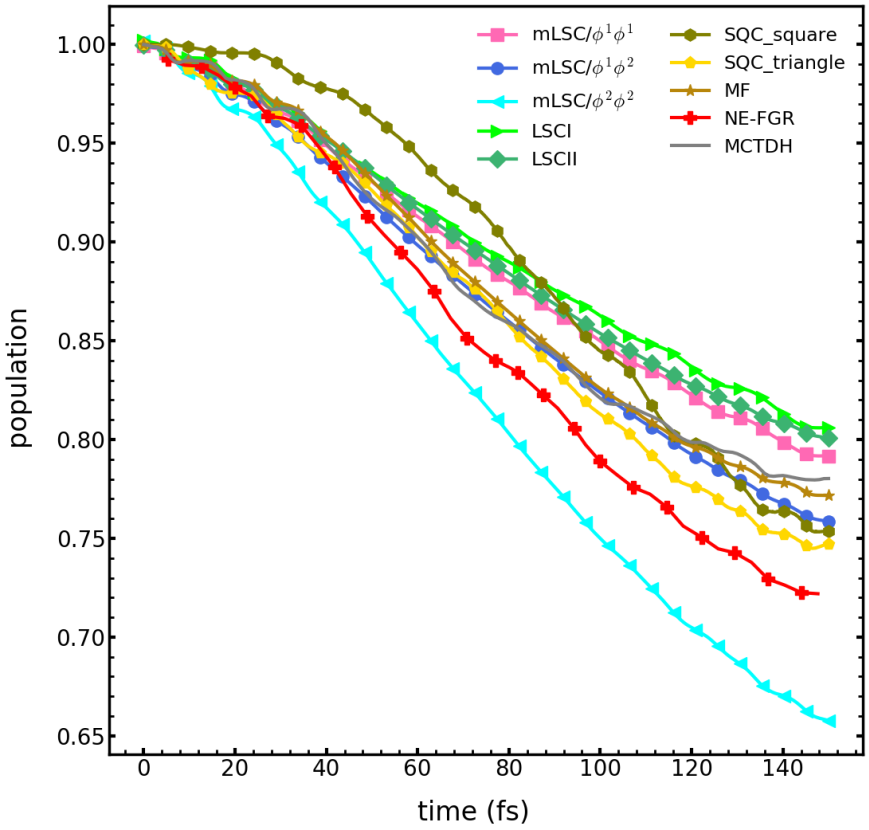

Figure IV.3: Comparison of donor population dynamics for the gas-phase MIA radical cation via different methods at T=0. The MCTDH results, represented by a black line, give the exact dynamics for MIA with the LVC model.

accuracy deteriorate at longer times). However, given the large number of methods, we believe that it serves as a useful organizational tool to guide the following discussion.

Based on the aforementioned classification of methods as *accurate* and *inaccurate*, they can be grouped into three categories: (1) methods which are consistently accurate for all three molecules; (2) methods which are consistently inaccurate for all molecules; and (3) methods with inconsistent accuracy, which are accurate for some molecules but inaccurate for others.

mLSC/$\phi^1\phi^1$ and LSCI fall into the first category (accurate for all three molecules). The fact that mLSC/$\phi^1\phi^1$ is seen to be somewhat more accurate and LSCI has been previously observed to be significantly less accurate than mLSC/$\phi^1\phi^1$ for other benchmark models[43, 85] points to mLSC/$\phi^1\phi^1$ as the method of choice.

mLSC/$\phi^2\phi^2$ is the only method that falls into the second category (inaccurate for all three

Method	LSCI	LSCII	mLSC/$\phi^1\phi^1$	mLSC/$\phi^1\phi^2$	mLSC/$\phi^2\phi^2$
fulvene	$\surd$	$\times$	$\surd$	$\surd$	$\times$
BMA	$\surd$	$\times$	$\surd$	$\times$	$\times$
MIA	$\surd$	$\surd$	$\surd$	$\surd$	$\times$

Method	SQC square	SQC triangle	MF	NE-FGR
fulvene	$\surd$	$\surd$	$\times$	$\times$
BMA	$\times$	$\times$	$\times$	$\surd$
MIA	$\times$	$\surd$	$\surd$	$\times$

Table IV.2: Summary of results. $\surd$ implies that the method is accurate and $\times$ implies that the method is inaccurate.

molecules). The poor performance of mLSC/$\phi^2\phi^2$ is particularly surprising in light of its previously reported ability to produce accurate results for the spin-boson and Tully models.[85] This observation underscores the limitations of those popular benchmark models and the need for extending the testing of approximate methods to other benchmark models, such as the LVC model considered here. It should also be noted that unlike mLSC/$\phi^1\phi^1$ and mLSC/$\phi^1\phi^2$, the derivation of mLSC/$\phi^2\phi^2$ is somewhat ad-hoc.

The remaining methods fall into the third category. Within this category, one can distinguish between two sub-categories: (3A) methods that are accurate for two out of the three molecules and (3B) methods that are accurate for one out of the three molecules.

Two methods fall into category (3A), namely mLSC/$\phi^1\phi^2$ and SQC with triangular windows. Both methods are seen to only be inaccurate in the case of BMA, which is also the only molecule for which NE-FGR is seen to be accurate. This correlation between weak electronic coupling and inaccuracy of mapping methods has been previously pointed out in the context of SQC.[49] The problem has been traced back to inefficient transfer of classical trajectories from one sampling window to another when the electronic coupling is weak. Switching from SQC with square sam-

pling windows to SQC with triangular sampling windows was proposed in Ref. 49 as a remedy for this problem. Interestingly, the poor performance of SQC with either square or triangular windows seem to suggest that this remedy is not sufficient in the case of BMA. The fact that unlike SQC, mLSC/$\phi^1\phi^1$ and LSCI are seen to be accurate for BMA can be traced back to the lack of a window function at time t in both, which guarantees that contributions from all trajectories are accounted for (as opposed to only accounting for contributions from trajectories that manage to transfer from one sampling window to another).

Finally, category (3B) includes the MF and SQC with square sampling windows methods. The only system for which MF is accurate is MIA, which can be attributed to the fact that MIA is the system with the smallest barrier and largest number of nuclear modes. As a result, the MF approximation is expected to be more valid. The failure of SQC with square sampling windows to reproduce the MCTDH result in BMA can be traced back to the weak electronic coupling in this system (see discussion above). The behavior of SQC with square sampling windows in the case of MIA is more subtle. On the one hand, the actual transition rate constant, as measured by the slope of the population as a function of time, is comparable to the exact one. On the other hand, there appears to be a delay in establishing rate kinetics within SQC with square sampling windows, which can be traced back to the gap between sampling windows in action space. More specifically, there is lag time between the time a trajectory leaves one sampling window and time it reaches another.

IV.4 Results with Generalized Quantum Master Equation

As we observed, several QC/MH methods cannot describe the dynamics of these LVC models well. The natural next step is to use these QC/MH methods to generate projection-free inputs for the generalized quantum master equation described in Chapter III. Because the LVC models do not satisfy the Condon approximation, we applied the non-Condon GQME here. Initial testing is done with full-projection GQME, i.e. choosing the projection operator to contain all electronic states.

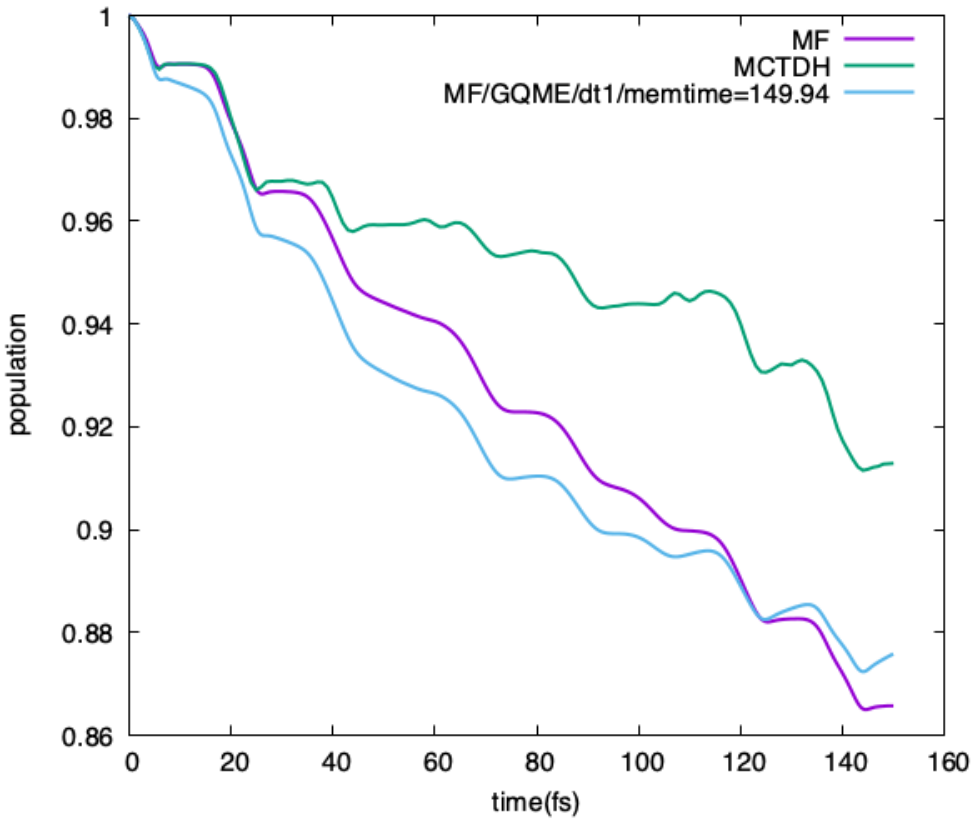

Figure IV.4: The donor population dynamics of BMA simulated with MF and GQME. The green line shows the exact results by MCTDH. The purple line shows the results generated by the input methods, i.e. MF. The Light-blue line shows the full-dimensionality non-Condon GQME results generated with MF as input methods and 149.94 fs as memory time.

The input method is selected to be Ehrenfest mean field. Here we choose the stepsize to be 0.024 fs, i.e. 1 a.u., and the number of trajectories to be 5×10^6.

Preliminary testing results of the GQME on the LVC models are shown in Figure IV.4 and Figure IV.5, for BMA and MIA, respectively. We observe that for BMA, the GQME using MF-generated projection-free inputs produces results slightly worse than those generated with MF. For MIA, we see a straight upward-trending curve after $t = 100$ fs. This behavior can be explained by inspecting the memory kernels of MIA presented in Figure IV.6. Not only do the kernels elements not diminish over time, but they start to increase after $t = 100$ fs. The memory kernels of BMA are presented in Figure IV.7. We see that the memory kernels of both BMA and MIA still persist for a longer time. A persisting kernel means that the systems do not forget. This might be caused by

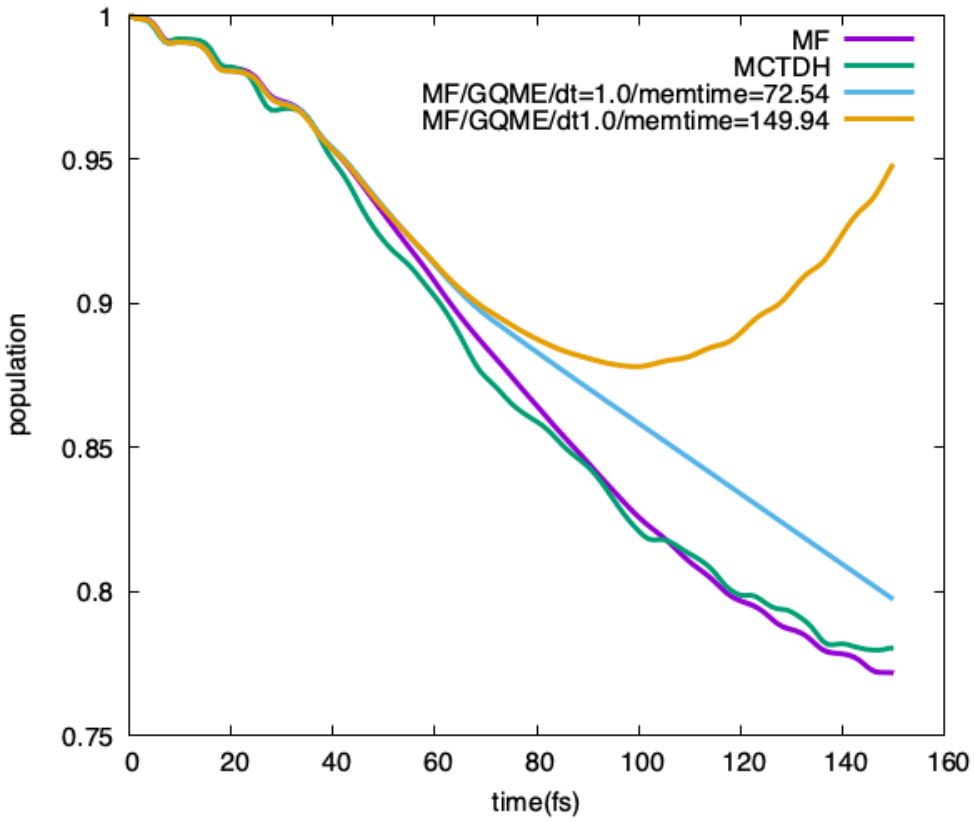

Figure IV.5: The donor population dynamics of MIA simulated with MF and GQME. The green line shows the exact results by MCTDH. The purple line shows the results generated by the input methods, i.e. MF. The Light-blue line shows the full-dimensionality non-Condon GQME results generated with MF as input methods and 72.5 fs as memory time. The orange line shows the full-dimensionality non-Condon GQME results generated with MF as input methods and 149.94 fs as memory time.

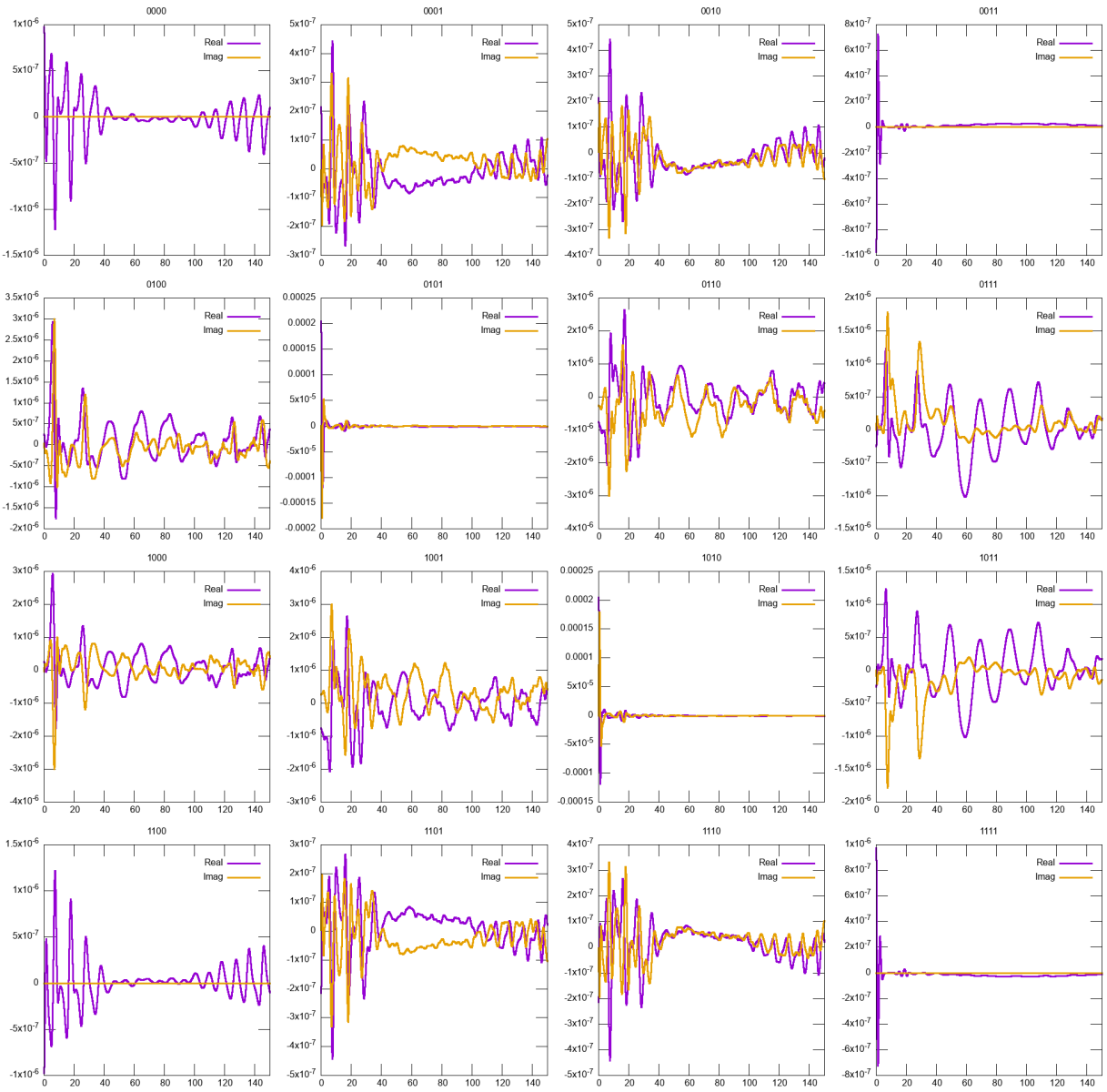

Figure IV.6: The memory kernel elements of MIA generated with MF projection-free inputs. The horizontal axis represents time, with the unit of fs. The orange line shows the imaginary parts and the purple line shows the real parts.

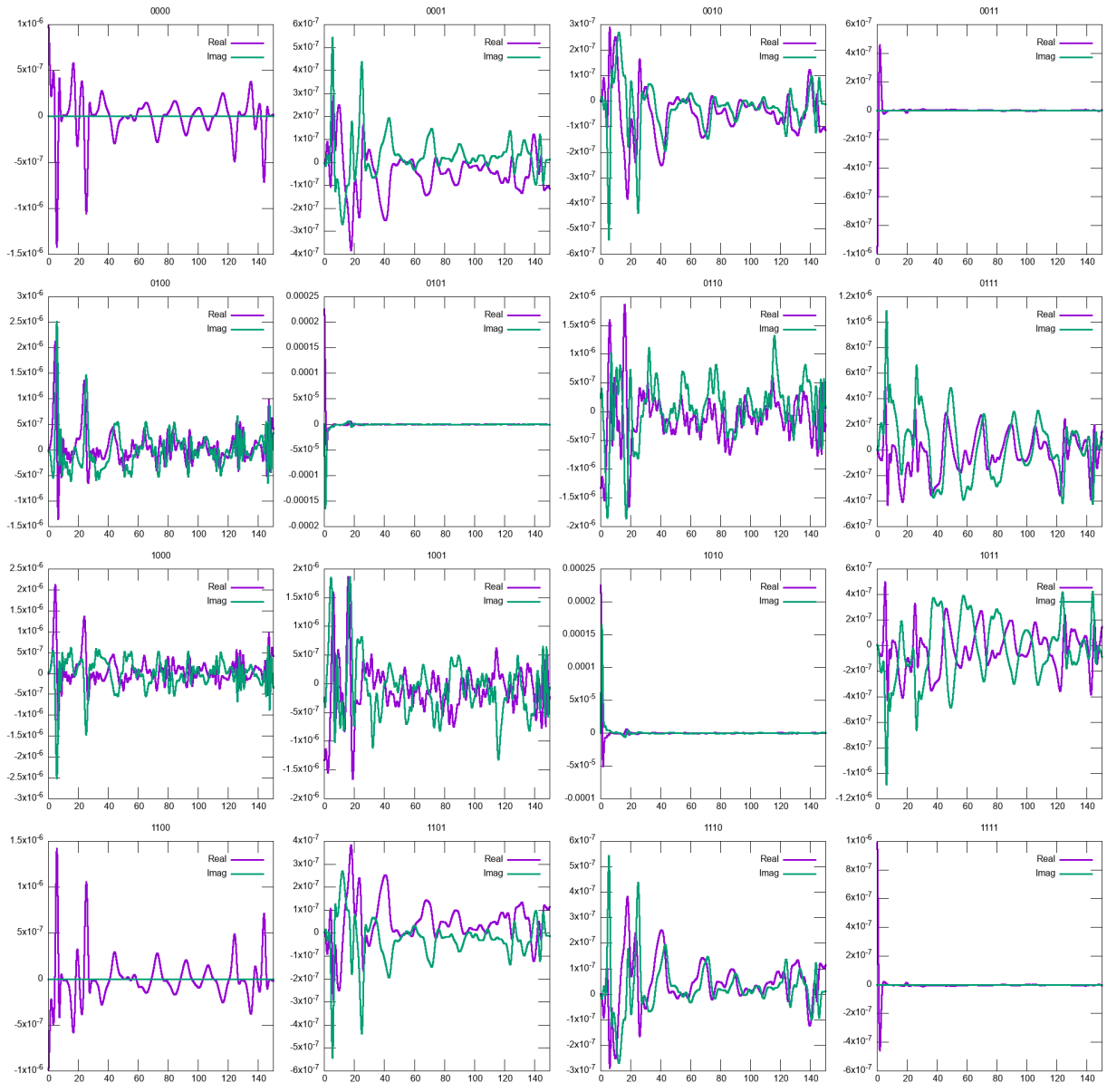

Figure IV.7: The memory kernel elements of BMA generated with MF projection-free inputs. The horizontal axis represents time, with the unit of fs. The orange line shows the imaginary parts and the purple line shows the real parts.

the necessity to use the non-Condon GQME. Compared to the Condon GQME, the non-Condon GQME requires the calculation of significantly more terms. This might introduce more numerical errors and leads to the strange behaviors of the kernels and the population dynamics.

IV.5 Concluding Remarks

Our main goal in this chapter was to extend the testing of QC/MH methods to systems with CIs. One reason for doing so is the central role CIs play in many photochemical processes of practical interest. Another reason is the need to extend the testing of those methods beyond the popular spin-boson and Tully benchmark models. Indeed, using the LVC model as a benchmark demonstrates the importance of going beyond the spin-boson and Tully models. More specifically, application of QC/MH methods to the LVC model was found to shed new light on the ability of those methods to yield accurate results. On the one hand, methods like SQC and mLSC/$\phi^2\phi^2$ were found to be significantly less accurate in LVC than they were in the spin-boson and Tully models. On the other hand, a method like mLSC/$\phi^1\phi^1$ was seen to emerge as the method of choice due to its reasonable accuracy for all benchmark models.

It should be noted that the analysis presented in this chapter was performed on systems with relatively high vibrational frequencies at zero temperature, which corresponds to the most challenging test for a QC method due to the pronounced quantum nature of the system under those conditions. On the one hand, it is encouraging to see that at least some QC/MH methods are accurate under those extreme conditions. On the other hand, one expects the accuracy of the other methods to improve with increasing temperatures.

We then explored the option of using QC/MH methods to calculate the memory kernel of the generalized quantum master equation (GQME). Preliminary assessments of GQME on LVC models done with MF-generated projection-free inputs show that the memory kernels do not decay over time. This results in strange behavior in the population dynamics. The cause of this might be with the non-Condon GQME. The non-Condon GQME requires significantly more terms to be gener-

ated, which might introduce additional numerical errors. Therefore one future direction of better describing the population dynamics of LVC models is to apply the reduced-dimensionality GQME. The reduced-dimensionality GQME can limit the terms applied and can potentially decrease the numerical errors introduced. Another direction is to apply the non-Condon GQME to various non-Condon systems. This will allow us to further understand the capability of the non-Condon GQME and gain a better understanding of the non-vanishing kernels.

CHAPTER V

Simulating The Fenna-Matthews-Olson (FMO) Complex

V.1 Introduction

Photosynthesis is a process that converts light energy to chemical energy and can be divided into four phases: light absorption and energy delivery by antenna systems, primary electron transfer in reaction centers, energy stabilization by secondary processes, and synthesis and export of stable products.[2] During the first phase of photosynthesis, photons are absorbed, leading to an excited state that causes charge separation in the reaction center. The antenna system typically transfers the excitation energy from one molecule to another, resulting in an excited donor in the reaction center. In the second phase, the electronic excitation energy is converted to chemical energy as the excited donor rapidly transfers charges to a nearby electron acceptor, which is where the primary reaction takes place. The excitation energy is thus transformed into chemical energy during this process. The process of electronic energy transfer and charge transfer are crucial steps in photosynthesis and are therefore the focus of numerous studies.[3–7] Understanding the dynamical processes of excitation energy transfer and electron transfer of photosynthetic light-harvesting systems can provide insights into the development of new technologies for energy production, such as biofuels, that can reduce the reliance on fossil fuels and mitigate climate change.

The discovery of long-lasting quantum coherence in certain photosynthetic systems has generated interest in the potential impact of quantum effects on their remarkable efficiency.[133] The

Fenna-Matthews-Olson (FMO) complex is a model system for studying the fundamental principles of energy transfer in photosynthesis. The FMO complex is also one of the first photosynthetic systems observed to have long-lived coherences.[134–137] Because of the availability of exact results, one model Hamiltonian of the FMO complex is considered to be a benchmark for approximate methods. In this chapter, we will focus on using the FMO complex as the benchmark to assess the ability of quasi-classical mapping Hamiltonian methods and generalized quantum master equation on simulating the energy transfer process for photosynthetic light-harvesting models.

The rest of this chapter is organized as follows. We outline the model Hamiltonian of the FMO complex in Sec. V.2. In Sec. V.3, the simulation results of the energy transfer via linearized semi-classical methods and the generalized quantum master equation are presented, compared to those generated with the hierarchical equations of motion (HEOM) method. Concluding remarks are given in section V.4.

V.2 Fenna-Matthews-Olson(FMO) Complex

The Fenna-Matthews-Oslon (FMO) complex is a trimer made of identical subunits. Each subunit contains seven bacteriochlorophyll (BChl) molecules. Here, we follow the same convention as shown in Ref. 138 to label the seven BChls. This then results in seven localized singly excited states. Studies have shown that the two primary pathways for energy transfer is[139]: 1) with BChl1 excited and then the energy transfer into BChl2 then to BChl3, after BChl3 is populated, excitation energy equilibrate between BChl3 and BChl4. 2) Wtih BChl6 excited and then the energy transfer into BChl5, BChl7 and BChl4 adn then to BChl3. A graph showing these two pathways is presented in Fig. V.1

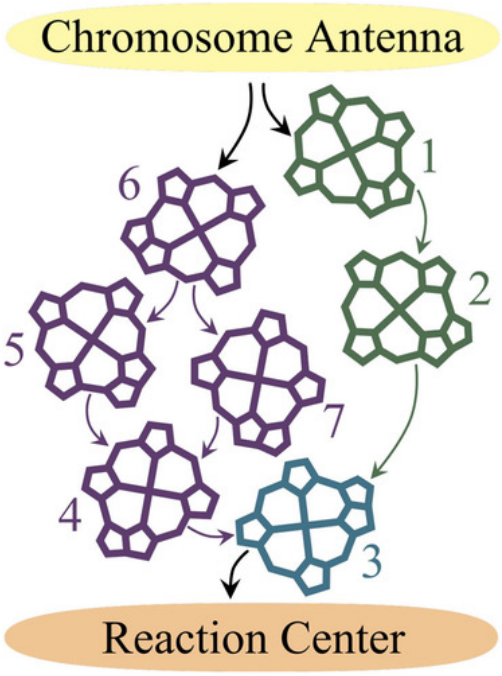

Figure V.1: Demonstration of the two primary pathways of FMO complex, adopted from Ref. 91 for demonstration purposes.

In this study, we test the following Hamiltonian for FMO complex[139, 140]:

$$\hat{H} = \sum_{i=1}^{N_e} \hat{H}_i(\hat{\mathbf{R}}, \hat{\mathbf{P}}) \, |i\rangle\langle i| + \sum_{\substack{j,k=1 \\ j\neq k}}^{N_e} \hat{V}_{jk}(\hat{\mathbf{R}}) \, |j\rangle\langle k| \,, \tag{V.1}$$

$$\hat{H}_i = \epsilon_i + \sum_{m=1}^{N_n} \sum_{i=1}^{N_e} \frac{\hat{P}_{m,i}^2}{2} + V_i(\hat{\mathbf{R}}), \tag{V.2}$$

$$V_i(\hat{\mathbf{R}}) = \sum_{m=1}^{N_n} \frac{1}{2}\omega_m^2 \left(\hat{\mathbf{R}}_{m,i} - \frac{c_m}{\omega_m^2} \right)^2 + \sum_{\substack{l=1 \\ l\neq i}}^{N_e} \sum_{m=1}^{N_n} \frac{1}{2}\omega_m^2 \hat{\mathbf{R}}_{m,l}^2, \tag{V.3}$$

$$\hat{V}_{jk} = \Gamma_{jk}. \tag{V.4}$$

Here, $N_e = 7$ is the electronic DOF, $N_n = 200$ is the nuclear DOF per BChl molecules. Therefore, the overall nuclear DOF is then $N_N = N_n \times N_e = 1400$. $\{c_1, ..., c_{N_n}\}$ and $\{\omega_1, ..., \omega_{N_n}\}$ are the mass-weighted coupling coefficients and frequencies for the nuclear normal modes, respectively; $\{\hat{R}_{1,1}, \ldots, \hat{R}_{N_e,N_n}\}$ and $\{\hat{P}_{1,1}, \ldots, \hat{P}_{N_e,N_n}\}$ are the mass-weighted position and momentum operators of the nuclear DOF, respectively; ϵ_i is the energy of the electronic state $|i\rangle$ at the equi-

librium geometry; and Γ_{jk} are the electronic coupling coefficients. The energy transfer processes are initiated at the excited electronic state 1 or 6, with the nuclear density operator corresponding to thermal equilibrium at the ground electronic state:

$$\hat{\rho}(0) = |1\rangle\langle 1| \otimes \hat{\rho}_n(0), \text{ or } \hat{\rho}(0) = |6\rangle\langle 6| \otimes \hat{\rho}_n(0), \tag{V.5}$$

$$\text{with } \hat{\rho}_n(0) = \frac{exp\left[-\beta \sum_{m=1}^{N_n} \sum_{i=1}^{N_e} \frac{\hat{P}_{m,i}^2}{2} + \frac{1}{2}\omega_m^2 \hat{\mathbf{R}}_{m,i}^2\right]}{Tr\left\{exp\left[-\beta \sum_{m=1}^{N_n} \sum_{i=1}^{N_e} \frac{\hat{P}_{m,i}^2}{2} + \frac{1}{2}\omega_m^2 \hat{\mathbf{R}}_{m,i}^2\right]\right\}}. \tag{V.6}$$

Here, $\beta = 1/k_B T$ is the inverse temperature, T is the absolute temperature, k_B is the Boltzmann constant. The electronic energy and coupling ϵ_i and Γ_{jk} are given by:[139, 140]

$$\begin{pmatrix} 12410 & -87.7 & 5.5 & -5.9 & 6.7 & -13.7 & -9.9 \\ -87.7 & 12530 & 30.8 & 8.2 & 0.7 & 11.8 & 4.3 \\ 5.5 & 30.8 & 12210 & -53.5 & -2.2 & -9.6 & 6.0 \\ -5.9 & 8.2 & -53.5 & 12320 & -70.7 & -17.0 & -63.3 \\ 6.7 & 0.7 & -2.2 & -70.7 & 12480 & 81.1 & -1.3 \\ -13.7 & 11.8 & -9.6 & -17.0 & 81.1 & 12630 & 39.7 \\ -9.9 & 4.3 & 6.0 & -63.3 & -1.3 & 39.7 & 12440 \end{pmatrix}, \tag{V.7}$$

with cm^{-1} as the unit. The spectral density of the nuclear modes are set up to be the Debye spectral density:

$$J(\omega) = \frac{\pi}{2} \sum_{k=1}^{N_n} \frac{c_k^2}{\omega_k} \delta(\omega - \omega_k) \xrightarrow[N_n \to \infty]{} \frac{2\lambda\omega_c\omega}{\omega_c^2 + \omega^2}, \tag{V.8}$$

$$c_k = \omega_k \sqrt{\frac{2\lambda}{N_n}},\ \omega_k = \omega_c \tan\left\{\frac{\pi}{2N_n}\left(k - \frac{1}{2}\right)\right\}, \tag{V.9}$$

with ω_c being the cutoff frequency and $\lambda = 35\text{cm}^{-1}$ being the reorganization energy.[139–141]

Here we present the parameters we tested in Table V.1, adapted from Ref. 139 and Ref. 91.

Table V.1: Fenna-Matthews-Olson (FMO) Model and Simulation Parameters

	Model Parameters		Numerical Parameters	
Model #	T(K)	$\omega_c(\text{cm}^{-1})$	Δt(fs)	N_{traj}
1	300	31.98	0.10	2.5×10^5

V.3 Results with Quasi-Classical Mapping Hamiltonian Methods and Generalized Quantum Master Equation

Because the Hamiltonian we are using here follows the Condon approximation, naturally, we choose to apply the GQME with the Condon approximation presented in Sec. III.3.1. Previous studies on the FMO model focused on using the Ehrenfest mean field method to generate the projection-free input [91], here we will apply the two versions of the linearized semi-classical approach, LSCI, and LSCII, to generate the projection-free inputs $\mathcal{F}_1$ and $\mathcal{F}_2$. The overall procedure is similar to that outlined in Sec. III.4. For model 1 in Table. V.1, the simulation results of GQME with Condon approximation and projection-free inputs generated with LSCI/LSCII are shown in Fig. V.2. From the dynamics, we observe that the GQME significantly improves the LSCI and LSCII dynamics, for both choices of the initial state ($|1\rangle\langle 1|$ or $|6\rangle\langle 6|$). The exceptions are with state 3 for LSCII-generated projection-free inputs. We observe from the right panel that using LSCII as the input method does not improve the dynamics of state 3 regardless of the initial states. Inspection on the top-left penal also shows that GQME with LSCI as input methods does not improve the description of state 1 with the electronic initial state set as $|1\rangle\langle 1|$. The convergence memory time is also reported in Fig. V.2. The convergence threshold is set up to be 1% of the scale of the dynamics.

We note here that in LSC methods, the trajectories required to achieve convergence are significantly large. As reported in Ref. [91], 35000 trajectories are enough for convergence for GQME with Ehrenfest-generated projection-free inputs. For GQME with LSC-generated projection-free inputs, we observed that even for the model 1, the model with high temperature and low cutoff frequencies, 250000 is required for convergence. This arises from the additional sampling on the

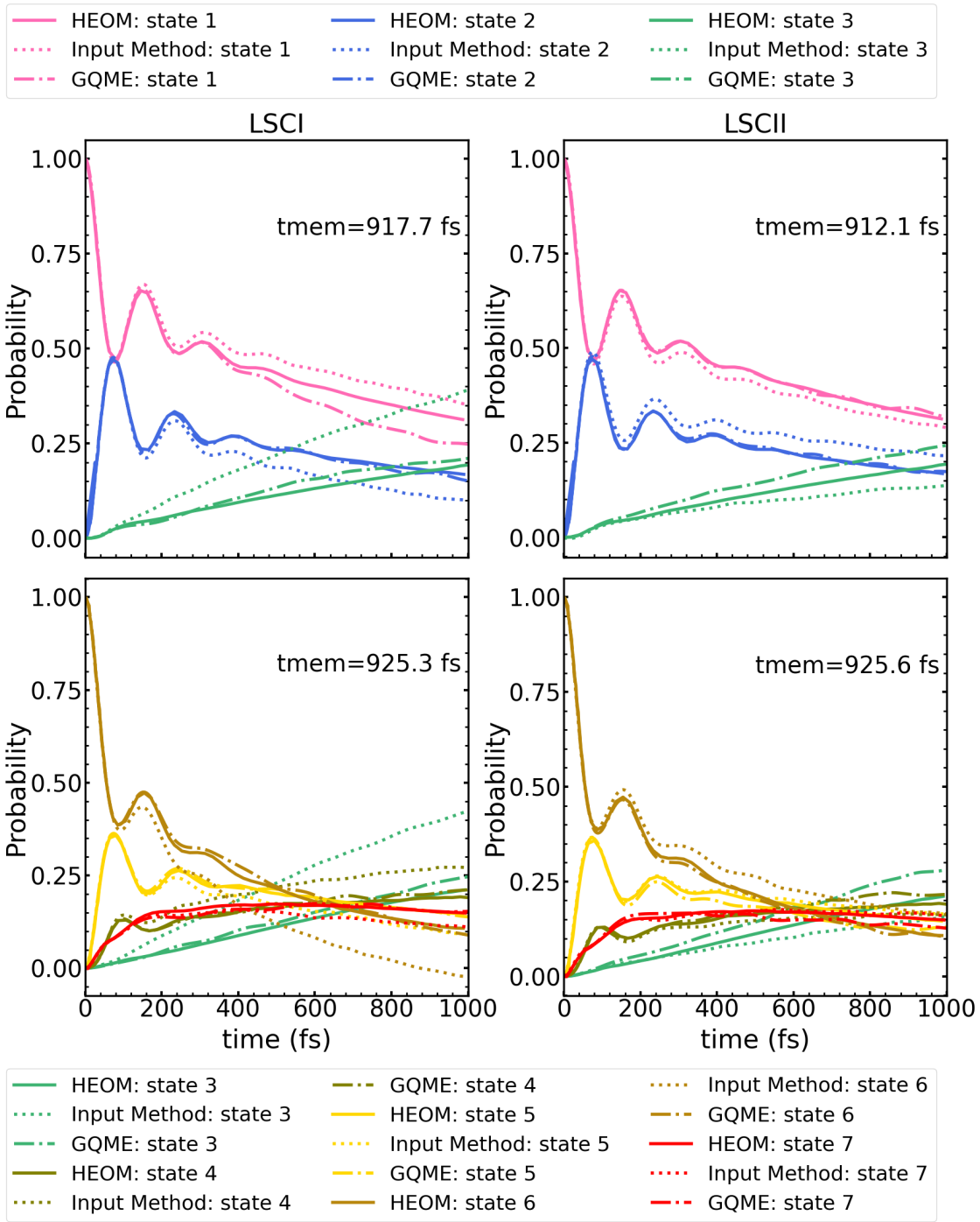

Figure V.2: The population dynamics of the FMO model 1 with parameters set as in Tabel V.1. Solid lines show the exact results by the hierarchical equation of motion (HEOM) reported in Ref. 139. Dashed lines show the results generated by the input methods, i.e. LSCI and LSCII, for the left and right column, respectively. Dotted-dashed lines on the left and right column show the GQME results generated with LSCI and LSCII as input methods, respectively. The top row of dynamics corresponds to the electronic initial state set as $|1\rangle\langle 1|$. The bottom row of dynamics corresponds to the electronic initial state set as $|6\rangle\langle 6|$. The convergenced memory time is reported on the graph.

electronic DOF that is required for the LSC methods. For FMO specifically, because there are seven electronics states involved, the convergence differences between Ehrenfest and LSC become more significant.

V.4 Concluding Remarks

In this chapter, we extend the application of QC/MH methods and the GQME to the FMO complex. Investigating the results, we found that GQME is capable of providing accurate descriptions by using LSCI and LSCII to generate projection-free inputs. We also observed a significantly large number of trajectories that are required for convergence. In fact, for the low temperature high ω_c model, i.e. model 1 in Ref. [91], we found that the LSCI requires an unfeasible number of trajectories to converge.

This prompts one of the future directions for the development of QC/MH methods to improve the convergence speed to limit the required computational costs. Another direction to reduce the computational cost is to apply the reduced-dimensionality GQME to the FMO model. Particularly, the development of the reduced-dimensionality GQME under the Condon approximation. As we previously discussed, the non-Condon GQME requires significantly more terms to be calculated in order to generate projection-free inputs. Since the FMO model follows the Condon approximation, it is natural to consider applying the Condon approximation to the reduced-dimensionality GQME.

CHAPTER VI

Methods for Calculating the Propagator for a Quantum Open System Governed by the GQME

VI.1 Introduction

Quantum computers have the potential to solve problems much faster than classical computers, and even provide solutions that are impossible by classical computing. However, simulating open quantum system dynamics on a quantum computer presents a significant challenge, as the time evolution operator of a quantum open system is non-unitary, while quantum gates are unitary. However, a quantum algorithm based on the Sz.-Nagy unitary dilation theorem has been developed to convert non-unitary operators into unitary operators in an extended Hilbert space. This algorithm has been successfully applied to simulate a Markovian two-level model [142] and a non-Markovian two-level model [143]. The same algorithm was also extended to Lindblad-type quantum master equations (QMEs) and was used to simulate the dynamics of the Fenna-Matthews-Olson complex [144]. Although this quantum algorithm has been effective in simulating open quantum systems described by the operator sum representation or Lindblad-type QMEs, there are limitations to these approaches. The Lindblad QME has restrictive approximations, including Markovianity and the ensemble of Lindbladian trajectories method involves user selection of system-bath parameters, limiting its applicability. While the operator sum representation of open quantum system dynamics is general, it requires knowledge of the Kraus operators.

An alternative route is to utilize a pre-established time evolution superoperator as input for the

quantum computing algorithm. Then apply the Sz.-Nagy unitary dilation theorem to convert the non-unitary time evolution superoperator into a unitary superoperator in an extended Hilbert space. With the dilated and now unitary time evolution superoperator and the system's initial state, we can then evolve the dynamics of any open quantum system on quantum computers. In this chapter, we present various methods that can be used to generate the time evolution superoperator for the reduced density matrix.

The rest of this chapter is organized as follows. The method to acquire the time evolution superoperators via the transfer tensor method and directly through the generalized quantum master equation are described in Sec. VI.2 and Sec. VI.3, respectively. In the next section, we present the comparison of the time evolution superoperators using these methods. Concluding remarks are given in section III.6.

VI.2 Generating the Propagator Through The Transfer Tensor Method

The transfer tensor method (TTM) provides a way to calculate the propagator $\mathcal{G}(t)$ for electronic density matrix:

$$\hat{\sigma}(t) = \mathcal{G}(t)\hat{\sigma}(0) \ . \tag{VI.1}$$

In the transfer tensor method, the dynamics can be calculated with: [145]

$$\hat{\sigma}(t_{n+1}) = \sum_{m=0}^{n} \mathcal{T}_{n+1,m}\hat{\sigma}(t_m), \tag{VI.2}$$

$$\mathcal{T}_n = \mathcal{G}_n - \sum_{m=1}^{n-1} \mathcal{T}_{n-m}\mathcal{G}_m. \tag{VI.3}$$

T_n is the transfer tensor, which measures the correlation between the system at time t and the system at previous times. In TTM, we assume time-tranlational invariant. This means that $\mathcal{T}_{n-m}$

only depends on the length of the time interval, instead of the initial or final time. Recall that the generalized quantum master equation discussed in Chapter III:

$$\frac{d}{dt}\hat{\sigma}(t) = -\frac{i}{\hbar}\langle\mathcal{L}\rangle_n^0\hat{\sigma}(t) - \int_0^t d\tau\ \mathcal{K}(\tau)\hat{\sigma}(t-\tau)\ . \tag{VI.4}$$

Comparing the GQME to Eq. VI.2, we can then find connections between transfer tensors and the memory kernels in GQME. Then with Eq. VI.3, we can use the resulting transfer tensors to generate the propagator $\mathcal{G}(t)$.

To make the connection, we apply numerical integration methods to GQME. The most straightforward choice is the forward and backward Euler methods. With forward Euler, the electronic density matrix propagated by one step can be expressed as:

$$\hat{\sigma}(t_{n+1}) = \hat{\sigma}(t_n) - \Delta t\left(\frac{i}{\hbar}\langle\mathcal{L}\rangle_n^0\hat{\sigma}(t_n) + \sum_{i=0}^{n-1}\Delta t\ \mathcal{K}(t_n,t_i)\hat{\sigma}(t_i)\right), \tag{VI.5}$$

$$T_{n+1,i} = \begin{cases} -\Delta t^2\mathcal{K}(t_n,t_i), & i\neq n \\ \mathcal{I} - \frac{i}{\hbar}\langle\mathcal{L}\rangle_n^0\Delta t. & i=n \end{cases} \tag{VI.6}$$

with Δt represent the step size, $\mathcal{I}$ is an identity matrix.

With backward Euler, the electronic density matrix propagated by one step can be expressed as:

$$\hat{\sigma}(t_{n+1}) = \hat{\sigma}(t_n) - \Delta t\left(\frac{i}{\hbar}\langle\mathcal{L}\rangle_n^0\hat{\sigma}(t_{n+1}) + \sum_{i=0}^{n}\Delta t\ \mathcal{K}(t_{n+1},t_i)\hat{\sigma}(t_i)\right), \tag{VI.7}$$

$$T_{n+1,i} = \begin{cases} -\Delta t^2\left(\mathcal{I} + \frac{i}{\hbar}\langle\mathcal{L}\rangle_n^0\Delta t\right)^{-1}\mathcal{K}(t_{n+1},t_i), & i\neq n \\ \left(\mathcal{I} + \frac{i}{\hbar}\langle\mathcal{L}\rangle_n^0\Delta t\right)^{-1}\left(\mathcal{I} - \Delta t^2\mathcal{K}(t_{n+1},t_i)\right), & i=n \end{cases} \tag{VI.8}$$

Another choice of numerical integration scheme is the trapezoidal method. With the trapezoidal

method, the electronic density matrix propagated by one step can be expressed as:

$$\begin{aligned}\hat{\sigma}(t_{n+1}) &= \hat{\sigma}(t_n) - \frac{1}{2}\Delta t\left(\frac{i}{\hbar}\langle\mathcal{L}\rangle_n^0\hat{\sigma}(t_n) + \sum_{i=0}^{n-1}\Delta t\,\mathcal{K}(t_n,t_i)\hat{\sigma}(t_i)\right) \\ &\quad -\frac{1}{2}\Delta t\left(\frac{i}{\hbar}\langle\mathcal{L}\rangle_n^0\hat{\sigma}(t_{n+1}) + \sum_{i=0}^{n}\Delta t\,\mathcal{K}(t_{n+1},t_i)\hat{\sigma}(t_i)\right), \qquad \text{(VI.9)}\end{aligned}$$

$$T_{n+1,i} = \begin{cases} -\left(\mathcal{I} + \frac{i}{2\hbar}\langle\mathcal{L}\rangle_n^0\Delta t\right)^{-1}\frac{1}{2}\Delta t^2\left(\mathcal{K}(t_n,t_i) + \mathcal{K}(t_{n+1},t_i)\right), & i \neq n \\ \left(\mathcal{I} + \frac{i}{2\hbar}\langle\mathcal{L}\rangle_n^0\Delta t\right)^{-1}\left[\mathcal{I} - \frac{i}{2\hbar}\langle\mathcal{L}\rangle_n^0\Delta t - \frac{1}{2}\Delta t^2\mathcal{K}(t_{n+1},t_i)\right]. & i = n \end{cases} \qquad \text{(VI.10)}$$

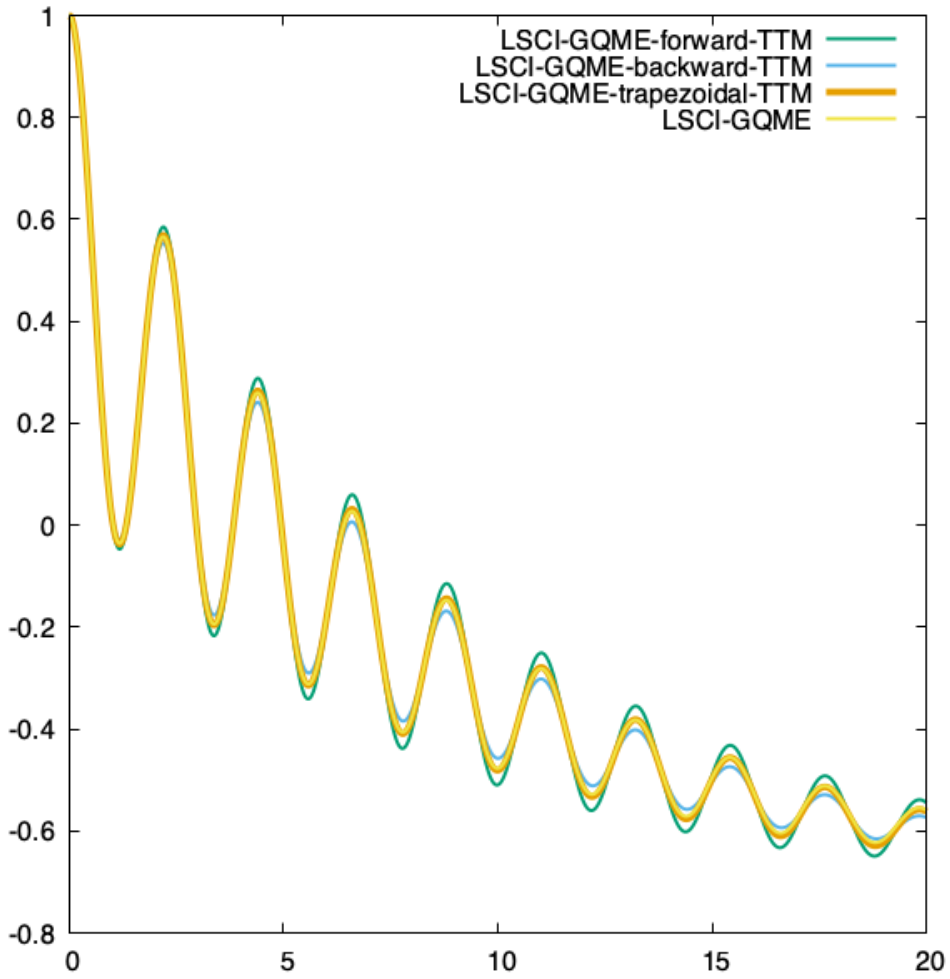

Figure VI.1: Comparison of different numerical methods on simulating the population dynamics for model D of the two-level spin-boson model described in Sec. II.4. The vertical axis represents the electronic observable $\hat{\sigma}_z$, and the horizontal axis represents the time with Γ^{-1} as the unit. Here we use LSCI to generate the projection-free inputs. The results with the three numerical methods are presented and compared to the results generated by directly solving the GQME.

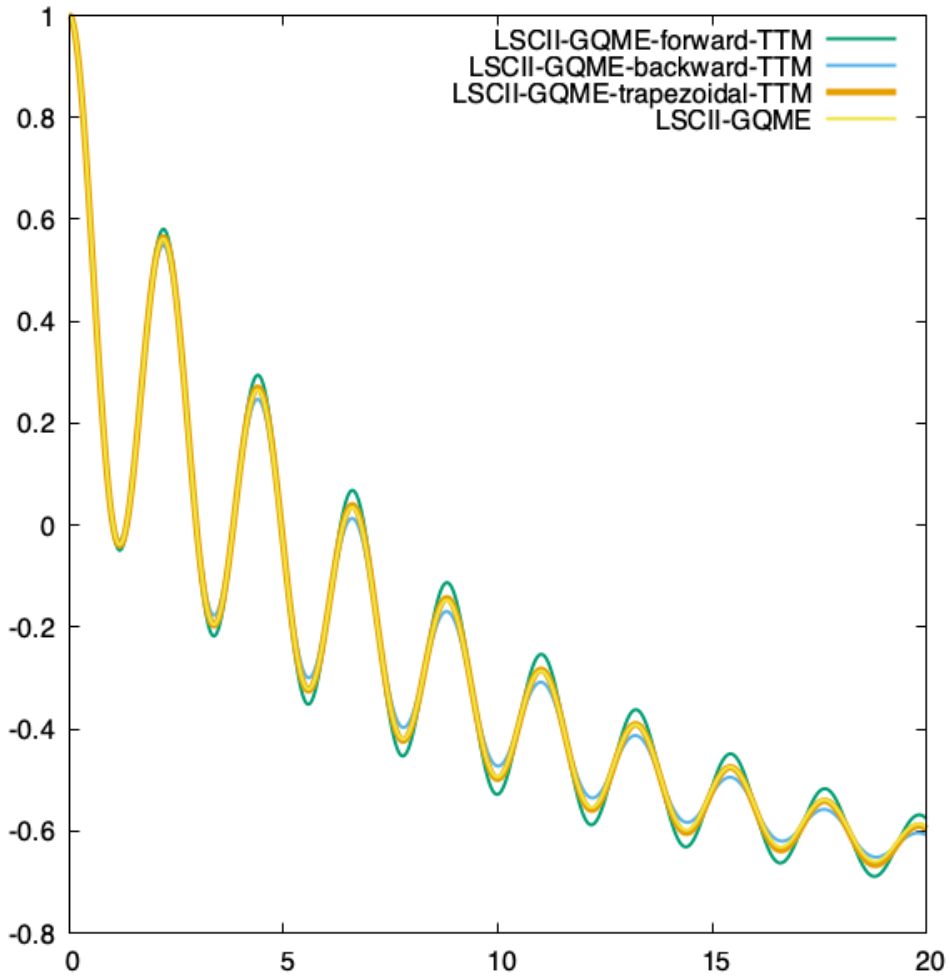

Figure VI.2: Comparison of different numerical methods on simulating the population dynamics for model D of the two-level spin-boson model described in Sec. II.4. The vertical axis represents the electronic observable $\hat{\sigma}_z$, and the horizontal axis represents the time with Γ^{-1} as the unit. Here we use LSCII to generate the projection-free inputs. The results with the three numerical methods are presented and compared to the results generated by directly solving the GQME.

The comparison of these methods is presented in Fig. VI.1 and VI.2. From the comparison, we observe that only the trapezoidal method can replicate the GQME method well. We note here that, both the backward Euler and the trapezoidal method require calculating the matrix inverse. Calculating matrix inverse can be hazardous and is typically expensive. Therefore, although the trapezoidal method can provide an accurate description, alternative routes to the propagator are still desired.

VI.3 Generating the Propagator Directly Through The Generalized Quantum Master Equations

In this section, we will introduce the direct way to calculate the propagator $\mathcal{G}$ with GQME. For the sake of concreteness, we will focus on molecular systems with an overall Hamiltonian of the following commonly encountered form:

$$\hat{H} = \sum_{j=1}^{N_e} \hat{H}_j |j\rangle\langle j| + \sum_{\substack{j,k=1 \\ k\neq j}}^{N_e} \hat{V}_{jk} |j\rangle\langle k| \tag{VI.11}$$

and an overall system initial state of the following commonly used single-product form:

$$\hat{\rho}(0) = \hat{\rho}_n(0) \otimes \hat{\sigma}(0) \ . \tag{VI.12}$$

The system and bath in this case correspond to the electronic and nuclear DOF, respectively. In Eqs. (VI.11) and (VI.12), $\hat{H}_j = \hat{\mathbf{P}}^2/2 + V_j\left(\hat{\mathbf{R}}\right)$ is the nuclear Hamiltonian when the system is in the diabatic electronic state $|j\rangle$, with the index j running over the N_e electronic states; $\hat{\mathbf{R}} = \left(\hat{R}_1, ..., \hat{R}_{N_n}\right)$ and $\hat{\mathbf{P}} = \left(\hat{P}_1, ..., \hat{P}_{N_n}\right)$ are the mass-weighted position and momentum operators of the $N_n \gg 1$ nuclear DOF, respectively; $\left\{\hat{V}_{jk} | j \neq k\right\}$ are the coupling terms between electronic states (which can be either nuclear operators or constants); and $\hat{\rho}_n(0)$ and $\hat{\sigma}(0)$ are the reduced density operators that describe the initial states of the nuclear (bath) and electronic (system) DOF, respectively. Throughout this section, boldfaced variables, e.g., $\mathbf{A}$, indicate vector quantities; a hat over a variable, e.g., $\hat{B}$, indicates an operator quantity; and calligraphic font, e.g., $\mathcal{L}$, indicates a superoperator.

Using projection operator techniques, one can then derive the following formally exact EOM, or GQME, for the reduced electronic density operator, $\hat{\sigma}(t)$ [68, 70, 91, 92]:

$$\frac{d}{dt}\hat{\sigma}(t) = -\frac{i}{\hbar}\langle\mathcal{L}\rangle_n^0 \hat{\sigma}(t) - \int_0^t d\tau \ \mathcal{K}(\tau)\hat{\sigma}(t-\tau) \ . \tag{VI.13}$$

The open quantum system dynamics of the reduced electronic density matrix described by this GQME are generated by the two terms on the R.H.S. of Eq. (VI.13). The first term is given in terms of the projected overall system Liouvillian $\langle\mathcal{L}\rangle_n^0 \equiv \mathrm{Tr}_n\{\hat{\rho}_n(0)\mathcal{L}\}$ (where $\mathcal{L}(\cdot) = [\hat{H}, \cdot]$ is the overall system Liouvillian and $\mathrm{Tr}_n\{\cdot\}$ is the trace over the nuclear (bath) Hilbert space), which is represented by a $N_e^2 \times N_e^2$ time-independent matrix. The second term is given in terms of the memory kernel $\mathcal{K}(\tau)$, which is represented by a $N_e^2 \times N_e^2$ time-dependent matrix. Further details about the GQME approach are provided in Chapter. III. From Eq. (VI.13), we can obtain a GQME for the system's time evolution superoperator, $\mathcal{G}(t)$, which is defined by:

$$\hat{\sigma}(t) = \mathcal{G}(t)\hat{\sigma}(0) \ . \tag{VI.14}$$

Substituting Eq. (VI.14) into Eq. (VI.13) and noting that the GQME should be satisfied for an arbitrary choice of $\hat{\sigma}(0)$, it is straightforward to show that $\mathcal{G}(t)$ satisfies the same GQME as $\hat{\sigma}(t)$:

$$\frac{d}{dt}\mathcal{G}(t) = -\frac{i}{\hbar}\langle\mathcal{L}\rangle_n^0\mathcal{G}(t) - \int_0^t d\tau\ \mathcal{K}(\tau)\mathcal{G}(t-\tau) \ . \tag{VI.15}$$

Thus, given the projected Liouvillian and memory kernels [$\langle\mathcal{L}\rangle_n^0$ and $\mathcal{K}(\tau)$, respectively], $\mathcal{G}(t)$ can be obtained by solving Eq. (VI.15). The propagator, $\mathcal{G}(t)$, can then be dilated to a unitary form which can be implemented on a quantum computer. The demonstration of this approach combined with an exact method is reported in Ref. [146].

VI.4 Concluding Remarks

In this chapter, we discussed multiple ways to generate the propagator for the reduced density matrix. These propagators can then be used as an input for the quantum computers to generate the dynamics for a longer time. The approaches we discussed all arise from the generalized quantum master equation. The generalized quantum master equation is a general method and does not presume approximations. This makes GQME a valuable method in developing a quantum computing

algorithm to describe the dynamics of open quantum systems.

We explored two routes to generate the propagator. The first route is through connecting to the transfer tensor method, and the second route is directly through GQME. Among all the choices to generate the propagator, directly through GQME seems to be the most straightforward one. Even though connecting TTM to GQME seems to be a detour in acquiring the propagator, this connection provides insights into the similarities between the two methods. Because GQME is reported to generate accurate results for various types of open quantum systems, this connection can lead to a new direction of development of TTM to improve accuracy.

CHAPTER VII

Conclusion

VII.1 Summary

The simulation of the electronic energy transfer and charge transfer dynamics is a topic of considerable interest. The studies in this area can further the development of many fields, including photochemistry, solar energy, photosynthesis, and photovoltaics. These processes are often described by open quantum systems. The theoretical studies on open quantum systems can be challenging due to the large dimensionality, as quantum-mechanically exact methods scale exponentially with dimension. Methods that apply classical approximations are then of great interest since the approximations can help reduce computational costs. An alternative route to minimize the computational costs is to reduce the dimension by focusing on the reduced dynamics.

In Chapter II, we described the quasi-classical mapping Hamiltonian methods (QC/MH), which applied the classical approximations to reduce the computational costs. The mapping Hamiltonian approach maps the electronic operators to auxiliary position and momentum operators that satisfy the same commutation relations. This mapping allows one to take the classical limit by applying Hamilton's equation. Several mapping schemes were introduced in this chapter along with one demonstration of the application of the LSCI approach to the two-level spin-boson model. We found that several QC/MH methods, including modified LSC and SQC, are capable of providing accurate descriptions for the dynamics of some electronic observables. Most methods, however, failed to generate accurate dynamics for the two-level spin-boson model. This prompts the alter-

native route of using the QC/MH methods to generate projection-free inputs for the generalized quantum master equations.

In Chapter III, the modified approach to the generalized quantum master equation with a general choice of projection operator is outlined. In this chapter, the GQME formalism is presented in the Liouville space, to facilitate the understanding of the effect of the projection operators of choice. In this chapter, we focused on evaluating the capability of GQME by observing the coherence dynamics of the two-level spin-boson model, as the population dynamics were previously extensively studied.[68–70]. We found that in addition to modified GQME's well-known capability to describe the population dynamics, it can also generate accurate descriptions of the coherence dynamics, when using projection-free inputs generated using the QC/MH methods, even when the QC/MH methods failed to generate accurate descriptions themselves.

The capability of QC/MH methods and GQME in describing the two-level spin-boson model leads to the interest in applying these methods to a wider range of models. In Chapter IV, the application of these two methods to the linear vibronic coupling (LVC) model is then presented. The significance of the LVC model is that it is one of the simplest models containing conical intersection, as conical intersection plays a central role in many photochemical processes. By comparing different QC/MH methods' ability to describe the LVC model, we found an inconsistency of performance, which means that even if a method performs well for the two-level spin-boson model, it might not perform well for the LVC model. This further suggested the necessity of benchmarking method accuracy with the LVC model. Since the LVC model no longer satisfies the Condon approximation, we explored the application of non-Condon GQME to the LVC model and found that the LVC model has long-lasting memory. This arguably leads to inaccurate simulation results from GQME. Another possible reason for the inaccurate results might arise from the large number of terms in the projection-free inputs required for the non-Condon GQME. This may lead to the accumulation of numerical errors.

The Fenna-Matthews-Olson (FMO) complex is the center of many studies, as it is one of the first photosynthetic systems observed to have long-lived coherences. In Chapter V, the energy transfer

process for an FMO model was simulated with linearized semi-classical methods and generalized quantum master equation. The results showed that GQME is capable of describing the energy transfer in FMO when using LSC methods to generate projection-free inputs.

Quantum computers have the potential to allow faster computation than classical computers. Developing a quantum computing algorithm for the study of energy and charge transfer process is then of natural interest. The problem arises from the non-unitary nature of the time evolution operators in open systems. One route to work around this is to invoke the Sz.-Nagy unitary dilation theorem to convert non-unitary operators into unitary operators in an extended Hilbert space. In Chapter VI, various methods to generate the time evolution operators were discussed and compared. We found that GQME has the capability to directly generate time evolution operators that can be used to propagate a reduced system on quantum computers.

VII.2 Future Directions

This dissertation outlined an introduction, exploration, and application of the QC/MH methods and the GQME. The application of these methods to various systems was also presented. Future directions include using these methods to study other systems of interest. Cavity-modified charge transfer, for example, is one of the processes of interest. It described the charge transfer process when the molecular electronic and vibrational degrees of freedom are coupled to the electromagnetic field modes of a cavity. The quantum heat engine and heat pump are also one type of systems of interest. The engine is composed of an oscillating external field-driven. Open quantum systems driven by time-dependent fields are an important topic for nonequilibrium thermodynamics as well as spectroscopy.

Further development of the QC/MH and GQME is another direction. The reduced-dimensionality GQME that was presented is completed without applying Condon approximations. It is interesting to develop reduced-dimensionality GQME with the Condon approximation due to the fact that lots of systems of interest satisfy this approximation. It is also an important sub-

ject as we observed that the non-Condon GQME requires a significalty large number of terms to be calculated, which can result in increasing computational costs and accumulation of numerical errors.

BIBLIOGRAPHY

[1] A. Nitzan, *Chemical Dynamics in Condensed Phases* (Oxford University Press, New York, 2006).

[2] R. E. Blankenship, *Molecular Mechanisms of Photosynthesis* (John Wiley & Sons, Ltd, 2002).

[3] R. van Grondelle, V. I. Novoderezhkin, *Physical Chemistry Chemical Physics* **8**, 793 (2006).

[4] N. Nelson, W. Junge, *Annual Review of Biochemistry* **84**, 659 (2015). PMID: 25747397.

[5] A. Chenu, G. D. Scholes, *Annual Review of Physical Chemistry* **66**, 69 (2015). PMID: 25493715.

[6] H. Wang, *et al.*, *Science* **316**, 747 (2007).

[7] M. Hervás, J. A. Navarro, M. A. De la Rosa, *Accounts of Chemical Research* **36**, 798 (2003).

[8] H. Cha, S. Lee, *2008 IEEE Industry Applications Society Annual Meeting* (IEEE, 2008), pp. 1–5.

[9] J.-M. Kwon, K.-H. Nam, B.-H. Kwon, *IEEE Transactions on Industrial Electronics* **53**, 1048 (2006).

[10] J. Zhao, A. Wang, M. A. Green, *Solar Energy Materials and Solar Cells* **65**, 429 (2001).

[11] G. Chamberlain, *Solar Cells* **8**, 47 (1983).

[12] G. Yu, J. Gao, J. C. Hummelen, F. Wudl, A. J. Heeger, *Science* **270**, 1789 (1995).

[13] J. Hou, O. Inganäs, R. H. Friend, F. Gao, *Nature materials* **17**, 119 (2018).

[14] D. Qian, *et al.*, *Nature materials* **17**, 703 (2018).

[15] M. E. Ziffer, *et al.*, *Journal of the American Chemical Society* **140**, 9996 (2018).

[16] W. Zhao, *et al.*, *Journal of the American Chemical Society* **139**, 7148 (2017).

[17] M. H. Lee, B. D. Dunietz, E. Geva, *J. Phys. Chem. Lett.* **5**, 3810 (2014).

[18] M. Beck, A. Jäckle, G. Worth, H.-D. Meyer, *Physics Reports* **324**, 1 (2000).

[19] S. López-López, R. Martinazzo, M. Nest, *J. Chem. Phys.* **134**, 094102 (2011).

[20] M. Nest, H. D. Meyer, *J. Chem. Phys.* **119**, 24 (2003).

[21] N. Makri, W. H. Miller, *The Journal of chemical physics* **87**, 5781 (1987).

[22] G. A. Worth, H.-D. Meyer, H. Köppel, L. Cederbaum, I. Burghardt, *International Reviews in Physical Chemistry* **27**, 569 (2008).

[23] Y. Yan, J. Jin, R.-X. Xu, X. Zheng, *Frontiers of Physics* **11** (2016).

[24] Y. Tanimura, *Phys. Rev. A* **41**, 6676 (1990).

[25] R.-X. Xu, Y. Yan, *Physical Review E* **75**, 031107 (2007).

[26] B. H. Lengsfield III, P. Saxe, D. R. Yarkony, *The Journal of chemical physics* **81**, 4549 (1984).

[27] J. C. Tully, *J. Chem. Phys.* **93**, 1061 (1990).

[28] R. Gherib, I. G. Ryabinkin, A. F. Izmaylov, *Journal of Chemical Theory and Computation* **11**, 1375 (2015).

[29] E. R. Bittner, P. J. Rossky, *J. Chem. Phys.* **103**, 8130 (1995).

[30] B. J. Schwartz, e. R. Bittner, O. V. Prezhdo, P. J. Rossky, *J. Chem. Phys.* **104**, 5942 (1996).

[31] J.-Y. Fang, S. Hammes-Schiffer, *The Journal of Physical Chemistry A* **103**, 9399 (1999).

[32] J.-Y. Fang, S. Hammes-Schiffer, *The Journal of chemical physics* **110**, 11166 (1999).

[33] O. V. Prezhdo, P. J. Rossky, *J. Chem. Phys.* **107**, 5863 (1997).

[34] O. V. Prezhdo, P. J. Rossky, *J. Chem. Phys.* **107**, 825 (1997).

[35] J. E. Subotnik, W. Ouyang, B. R. Landry, *The Journal of Chemical Physics* **139**, 214107 (2013).

[36] H. D. Meyer, W. H. Miller, *J. Chem. Phys.* **70**, 3214 (1979).

[37] G. Stock, M. Thoss, *Phys. Rev. Lett.* **78**, 578 (1997).

[38] A. Nassimi, S. Bonella, R. Kapral, *J. Chem. Phys.* **133**, 134115 (2010).

[39] H. Kim, A. Nassimi, R. Kapral, *J. Chem. Phys.* **129**, 084102 (2008).

[40] X. Sun, H. Wang, W. H. Miller, *J. Chem. Phys.* **109**, 7064 (1998).

[41] H. Wang, X. Song, D. Chandler, W. H. Miller, *J. Chem. Phys.* **110**, 4828 (1999).

[42] M. A. C. Saller, A. Kelly, J. O. Richardson, *J. Chem. Phys.* **150**, 071101 (2019).

[43] M. A. C. Saller, A. Kelly, J. O. Richardson, *Faraday Discuss.* **221**, 150 (2020).

[44] S. J. Cotton, W. H. Miller, *J. Phys. Chem. A* **117**, 7190 (2013).

[45] S. J. Cotton, W. H. Miller, *J. Chem. Phys.* **139**, 234112 (2013).

[46] S. J. Cotton, K. Igumenshchev, W. H. Miller, *J. Chem. Phys.* **141**, 084104 (2014).

[47] S. J. Cotton, W. H. Miller, *J. Phys. Chem. A* **119**, 12138 (2015).

[48] S. J. Cotton, W. H. Miller, *J. Chem. Theory Comput.* **12**, 983 (2016).

[49] S. J. Cotton, W. H. Miller, *J. Chem. Phys.* **145**, 144108 (2016).

[50] R. Kapral, *Annu. Rev. Phys. Chem.* **57**, 129 (2006).

[51] A. A. Kananenka, C.-Y. Hsieh, J. Cao, E. Geva, *J. Phys. Chem. Lett.* **7**, 4809 (2016).

[52] M. Santer, U. Manthe, G. Stock, *J. Chem. Phys.* **114**, 2001 (2001).

[53] C. Wan, J. Schofield, *J. Chem. Phys.* **113**, 7047 (2000).

[54] C. Wan, J. Schofield, *J. Chem. Phys.* **112**, 4447 (2000).

[55] G. Hanna, R. Kapral, *J. Chem. Phys.* **122**, 244505 (2005).

[56] D. Mac Kernan, G. Ciccotti, R. Kapral, *J. Phys. Chem. B* **112**, 424 (2008).

[57] D. A. Uken, A. Sergi, F. Petruccione, *Phys. Rev. E* **88**, 033301 (2013).

[58] A. Kelly, R. Kapral, *J. Chem. Phys.* **133**, 084502 (2010).

[59] N. Makri, *International Journal of Quantum Chemistry* **115**, 1209 (2015).

[60] N. Makri, *Chemical Physics Letters* **593**, 93 (2014).

[61] S. Kundu, N. Makri, *The Journal of Physical Chemistry Letters* **13**, 3492 (2022).

[62] A. G. Redfield, *Adv. Mag. Reson.* **1**, 1 (1965).

[63] Q. Shi, E. Geva, *J. Chem. Phys.* **119**, 12063 (2003).

[64] Q. Shi, E. Geva, *J. Chem. Phys.* **120**, 10647 (2004).

[65] M.-L. Zhang, B. J. Ka, E. Geva, *J. Chem. Phys.* **125**, 044106 (2006).

[66] A. Kelly, T. E. Markland, *J. Chem. Phys.* **139**, 014104 (2013).

[67] A. Kelly, N. Brackbill, T. E. Markland, *J. Chem. Phys.* **142**, 094110 (2015).

[68] E. Mulvihill, A. Schubert, X. Sun, B. D. Dunietz, E. Geva, *J. Chem. Phys.* **150**, 034101 (2019).

[69] E. Mulvihill, *et al.*, *J. Chem. Phys.* **151**, 074103 (2019).

[70] E. Mulvihill, E. Geva, *The Journal of Chemical Physics* **156**, 044119 (2022).

[71] M. Thoss, G. Stock, *Phys. Rev. A* **59**, 64 (1999).

[72] G. Stock, U. Müller, *The Journal of chemical physics* **111**, 65 (1999).

[73] W. H. Miller, *J. Phys. Chem. A* **105**, 2942 (2001).

[74] N. Ananth, C. Venkataraman, W. H. Miller, *J. Chem. Phys.* **127**, 084114 (2007).

[75] W. H. Miller, S. J. Cotton, *J. Chem. Phys.* **145**, 081102 (2016).

[76] W. H. Miller, S. J. Cotton, *Farad. Discuss.* **195**, 9 (2016).

[77] S. J. Cotton, R. Liang, W. H. Miller, *J. Chem. Phys.* **147**, 064112 (2017).

[78] J. Liu, *J. Chem. Phys.* **145**, 204105 (2016).

[79] A. Kelly, R. van Zon, J. Schofield, R. Kapral, *J. Chem. Phys.* **136**, 084101 (2012).

[80] G. Tao, *J. Phys. Chem. C* **118**, 17299 (2014).

[81] G. Tao, *J. Chem. Phys.* **144**, 094108 (2016).

[82] G. Tao, N. Shen, *J. Phys. Chem. A* **121**, 1734 (2017).

[83] G. Tao, *ChemPhysChem* **62**, 39 (2019).

[84] X. He, J. Liu, *J. Chem. Phys.* **151**, 024105 (2019).

[85] X. Gao, *et al.*, *J. Chem. Theory Comput.* **16**, 2883 (2020).

[86] Y. Liu, X. Gao, Y. Lai, E. Mulvihill, E. Geva, *J. Chem. Theory Comput.* **16**, 4479 (2020).

[87] H. Wang, M. Thoss, W. H. Miller, *J. Chem. Phys.* **112**, 47 (2000).

[88] J. E. Runeson, J. O. Richardson, *J. Chem. Phys.* **151**, 044119 (2019).

[89] S. J. Cotton, W. H. Miller, *The Journal of Chemical Physics* **150**, 194110 (2019).

[90] X. Gao, E. Geva, *The Journal of Physical Chemistry A* **124**, 11006 (2020).

[91] E. Mulvihill, *et al.*, *J. Chem. Phys.* **154**, 204109 (2021).

[92] E. Mulvihill, E. Geva, *The Journal of Physical Chemistry B* **125**, 9834 (2021).

[93] R. Zwanzig, *Nonequilibrium statistical mechanics* (Oxford University Press, New York, 2001).

[94] S. Mukamel, *Principles of Nonlinear Optical Spectroscopy* (Oxford, New York, 1995).

[95] H.-P. Breuer, F. Petruccione, *The Theory of Open Quantum Systems* (Oxford Press, Oxford, 2002).

[96] W. Domcke, D. R. Yarkony, H. Köppel, *Conical Intersections* (World Scientific, 2004).

[97] G. A. Worth, L. S. Cederbaum, *Annu. Rev. Phys. Chem.* **55**, 127 (2004).

[98] H. Köppel, W. Domcke, L. S. Cederbaum, *The Multi-Mode Vibronic-Coupling Approach* (World Scientific, 2004), pp. 323–367.

[99] B. G. Levine, T. J. Martínez, *Annu. Rev. Phys. Chem.* **58**, 613 (2007).

[100] A. F. Izmaylov, *et al.*, *J. Chem. Phys.* **135**, 234106 (2011).

[101] S. Deb, P. M. Weber, *Annu. Rev. Phys. Chem.* **62**, 19 (2011).

[102] S. Matsika, P. Krause, *Annu. Rev. Phys. Chem.* **62**, 621 (2011).

[103] W. Domcke and D.R. Yarkony and H. Köppel, *Conical Intersections: Theory, Computation and Experiment* (World Scientific, Singapore, 2011).

[104] W. Domcke, D. R. Yarkony, *Ann. Rev. Phys. Chem.* **63**, 325 (2012).

[105] J. S. Endicott, L. Joubert-Doriol, A. F. Izmaylov, *J. Chem. Phys.* **141**, 034104 (2014).

[106] Y. Shu, B. G. Levine, *Journal of Physical Chemistry C* **119**, 1737 (2015).

[107] R. Kosloff, *Ann. Rev. Phys. Chem.* **45**, 145 (1994).

[108] H.-D. Meyer, F. Gatti, G. A. Worth, *Multidimensional Quantum Dynamics*, MCTDH Theory and Applications (John Wiley & Sons, 2009).

[109] S. M. Greene, V. S. Batista, *J. Chem. Theory Comput.* **13**, 4034 (2017).

[110] A. D. McLachlan, *Mol. Phys.* **8**, 39 (1964).

[111] J. C. Tully, R. K. Preston, *J. Chem. Phys.* **55**, 562 (1971).

[112] I. Horenko, C. Salzmann, B. Schmidt, C. Schutte, *J. Chem. Phys.* **117**, 11075 (2002).

[113] J. E. Subotnik, N. Shenvi, *J. Chem. Phys.* **134**, 024105 (2011).

[114] P. Shushkov, R. Li, J. C. Tully, *J. Chem. Phys.* **137**, 22A549 (2012).

[115] L. Wang, D. Trivedi, O. V. Prezhdo, *J. Chem. Theory Comput.* **10**, 3598 (2014).

[116] H. M. Jaeger, S. Fischer, O. V. Prezhdo, *J. Chem. Phys.* **137**, 22A545 (2012).

[117] L. Wang, O. V. Prezhdo, *J. Phys. Chem. Lett.* **5**, 713 (2014).

[118] W. Ouyang, W. Dou, J. E. Subotnik, *J. Chem. Phys.* **142**, 084109 (2015).

[119] M. J. Bedard-Hearn, R. E. Larsen, B. J. Schwartz, *J. Chem. Phys.* **123**, 234106 (2005).

[120] C. C. Martens, J.-Y. Fang, *J. Chem. Phys.* **106**, 4918 (1997).

[121] A. Donoso, C. C. Martens, *J. Chem. Phys. A* **102**, 4291 (1998).

[122] R. Kapral, G. Ciccotti, *J. Chem. Phys.* **110**, 8919 (1999).

[123] S. Nielsen, R. Kapral, G. Ciccotti, *J. Chem. Phys.* **112**, 6543 (2000).

[124] Q. Shi, E. Geva, *J. Chem. Phys.* **121**, 3393 (2004).

[125] D. MacKernan, R. Kapral, G. Ciccotti, *J. Phys: Cond. Matter* **14**, 9069 (2002).

[126] D. W. H. Swenson, T. Levy, G. Cohen, E. Rabani, W. H. Miller, *J. Chem. Phys.* **134**, 164103 (2011).

[127] H. Köppel, W. Domcke, L. S. Cederbaum, *Multimode Molecular Dynamics Beyond the Born-Oppenheimer Approximation* (John Wiley & Sons, Ltd, 2007), pp. 59–246.

[128] X. Sun, E. Geva, *J. Chem. Phys.* **145**, 064109 (2016).

[129] H. Köppel, J. Gronki, S. Mahapatra, *jcp* **115**, 2377 (2001).

[130] H. Köppel, B. Schubert, *Mol. Phys.* **104**, 1069 (2006).

[131] C. S. M. Allan, B. Lasorne, G. A. Worth, M. A. Robb, *jpca* **114**, 8713 (2010).

[132] G. A. Worth, M. H. Beck, A. Jäckle, O. Vendrell, H.-D. Meyer, The MCTDH Package, Version 8.2, (2000). H.-D. Meyer, Version 8.3 (2002), Version 8.4 (2007). O. Vendrell and H.-D. Meyer Version 8.5 (2013). Version 8.5 contains the ML-MCTDH algorithm. Current versions: 8.4.18 and 8.5.11 (2020). See http://mctdh.uni-hd.de/.

[133] G. D. Scholes, G. R. Fleming, A. Olaya-Castro, R. van Grondelle, *Nature Chemistry* **3**, 763 (2011).

[134] G. Panitchayangkoon, *et al.*, *Proc. Natl. Acad. Sci. USA* **107**, 12766 (2010).

[135] S. Irgen-Gioro, K. Gururangan, R. G. Saer, R. E. Blankenship, E. Harel, *Chem. Sci.* **10**, 10503 (2019).

[136] E. Thyrhaug, *et al.*, *Nature Chemistry* **10**, 780 (2018).

[137] G. S. Engel, *et al.*, *Nature* **446**, 782 (2007).

[138] R. E. Fenna, B. W. Matthews, *Nature* **258**, 573 (1975).

[139] A. Ishizaki, G. R. Fleming, *Proc. Natl. Acad. Sci. USA* **106**, 17255 (2009).

[140] J. Adolphs, T. Renger, *Biophys. J.* **91**, 2778 (2006).

[141] W. Pfalzgraff, A. Montoya-Castillo, A. Kelly, T. Markland, *J. Chem. Phys.* **150**, 244109 (2019).

[142] Z. Hu, R. Xia, S. Kais, *Sci. Rep.* **10**, 1 (2020).

[143] K. Head-Marsden, S. Krastanov, D. A. Mazziotti, P. Narang, *Phys. rev. res* **3**, 013182 (2021).

[144] Z. Hu, K. Head-Marsden, D. A. Mazziotti, P. Narang, S. Kais, *Quantum* **6**, 726 (2022).

[145] J. Cerrillo, J. Cao, *Phys. Rev. Lett.* **112**, 110401 (2014).

[146] Y. Wang, *et al.*, Simulation of open quantum system dynamics based on the generalized quantum master equation on quantum computing devices (2022).